TECHNISCHE
UNIVERSITÄT
DARMSTADT

Determination of Photofission Fragment Characteristics of ^{234,238}U and ^{232}Th in the Barrier Region

Vom Fachbereich Physik
der Technische Universität Darmstadt

zur Erlangung des Grades
eines Doktors der Naturwissenschaften (Dr. rer. nat.)

genehmigte Dissertation von
Alf Göök, M.Sc.
aus Hallsberg (Schweden)

Referent: Prof. Dr. J. Enders
Korreferent: Prof. Dr. A. Oberstedt

Tag der Einreichung: 12.10.2012
Tag der Prüfung: 05.11.2012

Darmstadt 2012
D 17

Abstract

The photofission of ^{232}Th, ^{234}U and ^{238}U at excitation energies in the barrier region has been studied. The goal has been to extract information on the mass, total kinetic energy (TKE) and angular distributions of the fission fragments.

The experiments were performed using bremsstrahlung, produced by an electron beam in a copper radiator at the injector of the Superconducting Darmstadt linear accelerator (S-DALINAC). Mass and TKE distributions were determined by means of the double kinetic energy technique using a twin Frisch grid ionization chamber. The angular distributions were derived simultaneously by measuring the drift time of ionization electrons. Results show that this drift-time method is comparable in accuracy to other more commonly used methods, but with a simplified procedure for setting up the experiment.

Mass, TKE and angular distributions have been obtained from bremsstrahlung-induced fission of ^{232}Th at average excitation energies $\langle E_x \rangle = 6.68$ MeV and 7.26 MeV, for ^{234}U at $\langle E_x \rangle = 5.80$ MeV, 6.49 MeV and 7.23 MeV, and for ^{238}U at $\langle E_x \rangle = 5.90$ MeV, 6.11 MeV and 6.93 MeV. Results on fission fragment characteristics from ^{238}U(γ, f) show good agreement with literature data, which verifies the experimental procedure. The correlated mass and TKE data have been analyzed in terms of fission modes within the multi-modal random-neck-rupture model. The result exhibits a dominant yield of the mass asymmetric standard-2 mode in all the investigated fissioning nuclei, with a relative yield of $\sim$77 % in ^{232}Th, $\sim$75 % in ^{234}U and $\sim$67 % in ^{238}U. No strong fluctuation of the mode yields were found as a function of the excitation energy.

Correlations between mass, TKE and angular distributions have been investigated in ^{232}Th and ^{234}U. The correlation takes the form of an increased anisotropy for far-asymmetric masses and low TKE. The dependence of the anisotropy on mass and TKE could simultaneously be described by assuming specific angular distributions for the two mass-asymmetric standard fission modes. This analysis results in a larger anisotropy for the standard-2 mode, which suggests a higher outer barrier for this fission mode.

Zusammenfassung

In dieser Arbeit wurde die photoneninduzierte Spaltung von ^{232}Th, ^{234}U und ^{238}U untersucht. Die hierbei verwendeten Anregungsenergien lagen nur knapp oberhalb der jeweiligen Spaltbarriere. Informationen über die Massen- und Winkelverteilung sowie die Verteilung der totalen kinetischen Energie (TKE) der Spaltfragmente standen als Ziel dieser Arbeit im Vordergrund.

Der Elektronenstrahl des Injektorbeschleunigers am supraleitende Darmstädter Elektronenbeschleuniger (S-DALINAC) wurde in einem Kupferradiator gestoppt. Die hierbei entstandene Bremsstrahlung wurde genutzt, um das jeweils verwendete Nuklid zur Spaltung anzuregen. Durch die Methode der doppelten kinetischen Energie wurden die Massen- und TKE-Verteilungen der Spaltfragmente unter Verwendung einer Zwillings-Frisch-Gitter-Ionisationskammer bestimmt. Die Winkelverteilung der Spaltfragmente wurde gleichzeitig durch die Messung der Driftzeit der Ionisations-Elektronen bestimmt. Hierbei zeigen die Ergebnisse, dass die in dieser Arbeit verwendete und untersuchte Methode in ihrer Genauigkeit vergleichbar ist mit der üblicherweise genutzten Variante. Darüber hinaus ermöglicht sie ein leichteres Vorgehen beim Aufbau und der Inbetriebnahme des Experiments.

In dieser Arbeit wurden die Massen-, TKE- und Winkelverteilungen für die photoneninduzierte Spaltung von ^{232}Th bei mittleren Anregungsenergien $\langle E_x \rangle$= 6.68 MeV und 7.26 MeV ermittelt. Ebenso wurde für ^{234}U bei $\langle E_x \rangle$= 5.80 MeV, 6.49 MeV und 7.23 MeV verfahren und für ^{238}U bei $\langle E_x \rangle$= 5.90 MeV, 6.11 MeV und 6.93 MeV. Die Ergebnisse der Massen- und TKE-Verteilung von ^{238}U(γ, f) zeigen eine gute Übereinstimmung mit den Literaturwerten, wodurch die experimentelle Vorgehensweise bestätigt wird. Die korrelierten Massen- und TKE-Daten wurden im Bezug auf verschiedene Spaltmoden nach dem Modell eines multimodalen random-neck-rupture untersucht. Die Ergebnisse zeigen hierbei einen dominanten Beitrag der massenasymmetrischen Standard-2-Mode in allen untersuchten Nukliden, mit einem relativen Beitrag von ∼77 % in ^{232}Th, ∼75 % in ^{234}U und ∼67 % in ^{238}U. Starke Fluktuationen der Modenbeiträge als Funktion der Anregungsenergie wurden nicht betrachtet.

Ebenso wurden die Korrelationen zwischen Massen-, TKE- und Winkelverteilung in ^{232}Th und ^{234}U untersucht. Die vorliegende Korrelation zwischen Massen- und TKE-Verteilung zeigt eine erhöhte Anisotropie für stark asymmetrische Massen und kleine TKE. Die gleichzeitige Abhängigkeit der Anisotropie von Masse und TKE konnte durch die Annahme spezifischer Winkelverteilungen für die zwei massenasymmetrischen Standard-Spaltmoden beschrieben werden. Die in dieser Arbeit verwendete Analyse der Massen-, TKE- und Winkelverteilung resultiert in einer stärker ausgeprägten Anisotropie für die Standard-2-Mode. Dieses Ergebnis lässt auf eine höhere äußere Barriere für diese Spaltmode schließen.

Contents

1 Introduction **1**

2 Theoretical Background **5**
2.1 Fission barriers 6
2.2 Theory of Fission Fragment Angular Distributions 9
2.3 Models of Fission-Fragment Mass Distributions 12
2.3.1 Scission-Point Model 13
2.3.2 Multi-Modal Random-Neck-Rupture Model 14
2.3.3 Mass Dependence of Angular Distributions 17

3 Experiments **19**
3.1 Bremsstrahlung Facility 21
3.2 Fission-Fragment Detector 21
3.2.1 Signal Generation: The Shockley-Ramo Theorem 23
3.2.2 Weighting Potential Distributions 23
3.2.3 Charge Signals 26
3.3 Data Acquisition 29

4 Data Analysis **31**
4.1 Calculation of Average Excitation Energies 31
4.2 Determination of Angular Distributions 34
4.2.1 Angular Resolution 35
4.3 Calculation of Mass and Total Kinetic Energy 36
4.3.1 Correction for Grid Inefficiency 38
4.3.2 Energy-Loss Correction 39
4.3.3 Pulse-Height Defect 41

5 Experimental Results **45**
5.1 Mass and TKE Distributions 45
5.2 Influence of Target Thickness 54

5.3 Angular Distributions 58
5.3.1 Mass Dependence of Angular Distributions 61

6 Discussion of the Experimental Results 65
6.1 Revisiting the Reaction $^{238}U(\gamma, f)$ 65
6.2 Fission-Mode Analysis 67
6.2.1 Interpretation of the Mass Dependence of Angular Distributions . . 83

7 Summary and Conclusions 91

8 Outlook 93
8.1 A Gaseous Uranium Hexaflouride Active Target 93
8.1.1 Setup for Investigation of UF_6 Counting-Gas Properties 94
8.1.2 Experimental Procedure and Preliminary Results 94
8.2 Investigations of Shape Isomers 98

A Transformation of Angular Distributions 101

Chapter 1

Introduction

Although it has been over 70 years since the nuclear reaction known as fission was discovered [1–3], an accurate quantitative description of the process is still lacking. Reliable predictions of fission fragment properties from a wide range of fissioning systems is needed for different applications, e. g. nuclear energy production and nuclear astrophysics. For future nuclear power plants, the description and modeling of the fission process becomes increasingly important for safe operation and evaluation of new innovative reactor designs [4]. In nuclear astrophysics, fission plays an important role in understanding the mechanism of nucleosynthesis by rapid neutron captures [5].

Detailed microscopic treatment of the fission process is generally too complicated, due to the many degrees of freedom. Instead, so-called deterministic models are commonly applied that treat the fissioning nucleus as a macroscopic object and include corrections for the microscopic effects. One such model that has been quite successful in describing fission fragment mass distributions is the so-called Multi-Modal Random Neck Rupture (MM-RNR) model. The concept of fission modes was first introduced in the 1950s by Turkevich and Niday [6]. To describe the dependence of mass-symmetric fission yields on incident neutron energy, it was suggested that fission proceeds via two modes, a symmetric and an asymmetric one. The theoretical foundation for this empirical approach was established by Brosa et al. [7], calculating potential energy landscapes of deforming nuclei and identifying fission modes as pathways through these landscapes. From the calculations further splitting into several symmetric and asymmetric modes was predicted. The number of modes that play a role for the actinide nuclei are in most cases three, one symmetric and two asymmetric ones. The two asymmetric modes are referred to as the standard modes, and are labeled S1 and S2 according to increasing asymmetry. The symmetric mode has a much longer scission configuration and is therefore labeled as the super-long (SL) mode. An open question in multi-modal fission is where, in the potential energy landscape, the

two standard modes split. According to the calculations by Brosa et al. [7] the bifurcation takes place after passing a common outer barrier. On the other hand, there are calculations of the potential energy landscape [8,9] and model calculations to experimental data [10–12] pointing to a bifurcation point in the shape-isomeric minimum, resulting in separate outer barriers for the two standard modes. In the latter case a correlation between the fission modes characteristic mass and total kinetic energy (TKE) with a change in the angular distribution is expected, since the angular distributions are settled at the saddle point. Consequently, failure to find such correlations would rule out the existence of separate outer barriers for the standard modes. The use of photons to investigate such correlation is advantageous due to a well defined J^π value of the compound nucleus and the involvement of only a few so-called transition states on top of the fission barrier that determine the angular distributions.

In this thesis the nuclear fission process is studied experimentally by means of low-energy bremsstrahlung induced fission. The experiments were performed at the superconducting injector linac of the Superconducting Darmstadt linear accelerator (S-DALINAC [13]). The primary fission fragment mass and TKE distributions from the three light actinide nuclei ^{238}U, ^{234}U and ^{232}Th, have been determined by means of the double kinetic energy technique using a twin Frisch grid ionization chamber. In the case of ^{234}U and ^{232}Th angular distributions and their correlations with the mass and TKE distribution have also been studied. Part of the results [14] as well as an analysis of the method for determining the fission-fragment emission angle [15] have already been published.

The photofission fragment mass and TKE distributions of ^{238}U were studied in order to establish an experimental procedure and analysis technique. Detailed data on this reaction is available in the literature [16, 17] and has served as a reference for the measurements performed within this thesis work. Since the main goal of the $^{238}\mathrm{U}(\gamma, f)$ experiment was the determination of the fission fragment mass and TKE distributions, and due to the fact that angular distributions in low energy photofission show a minimum at 0°, this measurement was performed with the chamber oriented at 45° relative to the photon beam in order to maximize the yield in the angular cone of accepted events. This has the disadvantage that the determination of the angular distribution is complicated by the loss of rotational symmetry around the beam axis.

Fission fragment mass and TKE distributions and their correlations with the angular distributions in the reaction $^{234}\mathrm{U}(\gamma, f)$ were studied for the first time in the energy range close to the fission barrier. The measurement was calibrated with results from the known photofission of $^{238}\mathrm{U}(\gamma, f)$ and performed together with a measurement on $^{232}\mathrm{Th}(\gamma, f)$, where the correlations of mass, TKE and angular distributions could also be studied.

Several innovative nuclear reactor design concepts are based on the thorium fuel cycle [18]. In which the energy producing reaction is $^{233}\mathrm{U}(n, f)$, which leads to the same compound state as in $^{234}\mathrm{U}(\gamma, f)$. The ^{233}U fuel is produced from the reaction $^{232}\mathrm{Th}(n, \gamma)$ and sub-

sequent β-decays. In both of these processes significant γ-ray fluences are present. An understanding of the ^{232}Th and ^{234}U photofission fragment properties are required for a thorough theoretical assessment of such concepts.

The dominant population of $J^\pi = 1^-$ states in photofission and their possible mixing with 1^+ states may give access to another interesting feature of fissioning nuclei, namely parity non-conservation (PNC). PNC effects have earlier been studied in fission induced by polarized thermal neutrons [19–23], as one example of symmetry breaking in compound nuclear reaction [24]. A slight preference of the light fission fragment to be emitted either parallel or anti-parallel to the neutron helicity is observed. The PNC effect measured in neutron-induced fission is several orders of magnitude stronger than what can be expected from the relative strengths of weak and strong interaction. Theory offers explanations for the enhancement of parity violation in compound-nucleus reactions in terms of a statistical model. In order to resolve open questions [25–27] in describing the enhancement factors, further experimental data taken with different probes is desirable. The new polarized injector SPIN [28] installed at the S-DALINAC [13], and realized in the framework of the collaborative research center SFB 634 of Deutsche Forschungsgemeinschaft, will deliver a high intensity beam of longitudinally polarized electrons. This may allow PNC to be investigated in photofission as bremsstrahlung photons near the endpoint energy are circularly polarized. Statistical enhancement of PNC effects upon averaging have been discussed by Flambaum and Gribakin [29]. Data from this experiment has been used to estimate the feasibility of a study of PNC effects in photofission. It could be estimated that such an experiment using the same experimental setup would require more than a year of beam time at optimum conditions. Hence, a significant increase in luminosity is mandatory for the experiment to be successful. An increase of the thickness of the standard solid targets is undesirable. As will be shown in this thesis, this would lead to a strong deterioration of the achievable mass resolution. Another approach to achieve the required luminosity without deteriorated mass resolution is the use of an active target. As a first step to such a device experimental investigations of the counting gas properties of UF_6 have been undertaken. Preliminary results of this investigation will be presented in the last chapter of this thesis.

Chapter 2

Theoretical Background

In 1939 Meitner, Hahn and Strassmann discovered that when bombarding uranium with neutrons, atoms chemically analog to barium are created [1]. It was proposed that the uranium nucleus, after capturing a neutron, was split into two new nuclei. The physical explanation for this phenomenon was given by Meitner and Frisch later the same year [2], using an essentially classic picture of the nucleus. On account of the close packing and strong energy exchange of the constituents of heavy nuclei, they can be expected to move in a collective way, which may be described, e. g. by the motion of a charged liquid-drop. If enough energy is added, the motion may be violent enough that the drop splits into two smaller ones. Due to the Coulomb repulsion, the fragments must be given a large kinetic energy as the liquid-drop splits. With the use of a uranium-lined ionization chamber irradiated by neutrons, Frisch was able to observe large pulses, corresponding to the predicted nearly 200 MeV of total kinetic energy [3]. Thus, providing the first direct experimental evidence for this new type of radioactive decay, which was given the name fission.

Shortly after the discovery of neutron-induced fission, search began for fission induced by γ-rays. First experimental evidence was provided by Haxby, Shoupp, Stevens and Wells [30] in 1941, who reported on fission of uranium and thorium induced by γ-rays from the $\mathrm{F}(p,\gamma)$ reaction. The use of photons to investigate the fission process offers some principle differences towards the neutron induced reaction. Due to hindrance of higher multipolarities, low energy photon absorption is mainly due to electric dipole (E1) and to a lesser extent due to magnetic dipole (M1) and/or electric quadrupole excitations (E2), see Refs. [31,32]. This leads to excited states with J^π values of 1^-, 1^+ and 2^+ for even-even nuclei, as opposed to hadronic excitation spectra, which are in general more complex. A further advantage is that there is no lower limit, due to the binding energy of the particle, on the excitation energy of the compound nucleus. Hence, the use of photons allows

investigating the fission process throughout the entire barrier region. In addition, nuclei that are difficult to investigate with neutrons, due to the instability of the target, may be accessible with photons.

2.1 Fission barriers

The reason why nuclei do fission can be understood by studying the binding energy per nucleon. From the large energy release in fission one would naively expect this decay branch to be important for all nuclei with mass numbers greater than about twice that of ^{58}Fe. However, spontaneous fission does not become an important competitor with alpha decay before reaching nuclei of mass A $\sim$ 250. The reason for the hindrance of the fission decay channel is the fission barrier.

The concept of the fission barrier can be understood using the liquid-drop model. Considering the nucleus as a charged liquid-drop, the energy can be described by Bethe-Weizsäcker's semi-empirical mass formula. The fission barrier is simply the energy as a function of deformation. Assuming incompressibility of nuclear matter, only the surface E_s and Coulomb E_c terms of the liquid-drop energy are relevant. The deformation energy can then be defined as

$$E_{def}(\epsilon) = E_s(\epsilon) + E_c(\epsilon) - E_s(0) - E_c(0), \tag{2.1}$$

where ϵ is a deformation parameter. It is given as a combination of the expansion coefficients α_n of the nuclear surface. For an originally spherical liquid-drop of radius R_0 the distance from the center to the deformed surface can be expressed using Legendre polynomials

$$r(\theta) = R_0 \left[1 + \sum_n \alpha_n P_n(\cos\theta) \right]. \tag{2.2}$$

In Fig. 2.1 the liquid-drop energy is plotted as function of quadrupole α_2 and hexadecupole α_4 deformation, the potential was calculated according to Bohr and Wheeler [33]. Following along the red dashed line the drop deforms into a dumb-bell shape. If enough energy is supplied, the barrier (cf. right hand side of Fig. 2.1) can be overcome and the drop will split in two smaller ones. Limiting the discussion to pure quadrupole distortion, the deformation energy can be written as

$$E_{def}(\epsilon) = \frac{1}{5}\alpha_2^2 \left(2E_s(0) - E_c(0)\right). \tag{2.3}$$

From this equation it is apparent that the nucleus is unstable against small deformations, if the so-called fissility parameter,

$$x = E_c(0)/2E_s(0) \tag{2.4}$$

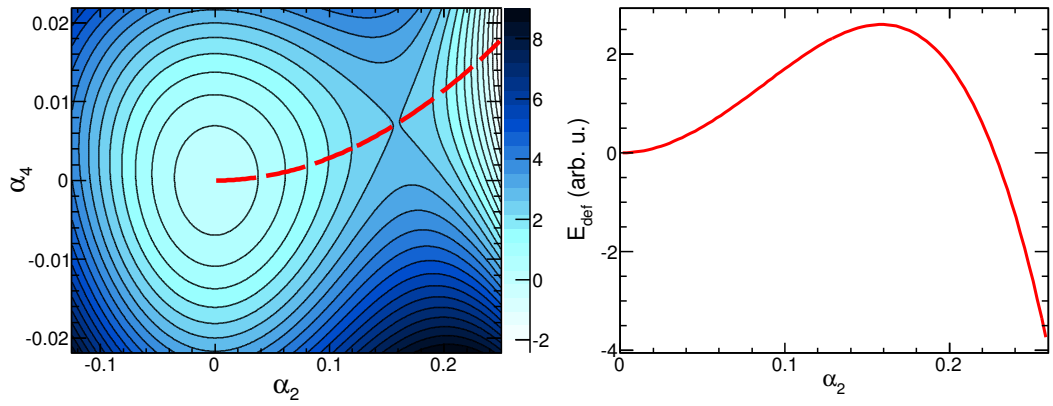

Fig. 2.1: *Potential energy contour plot (left) of a charged liquid-drop as function of quadrupole α_2 and hexadecupole α_4 deformation. The potential energy along the red dashed line, which represents the most favorable path to fission, is plotted to the right as a function of quadrupole deformation.*

is greater than one. The definitions of the surface and Coulomb terms from Bethe-Weizsäcker's mass formula lead to $x \propto Z^2/A$. Proportionality constants fitted to experimental mass data give the result that nuclei with $Z^2/A > 50$ are unstable against deformations of the simplest type [34], and will fission spontaneously. Even though the liquid-drop model can be used to explain the most fundamental question, i. e. why nuclei fission, it fails in predicting some basic properties of actinide nuclei. First of all, for all nuclei the liquid-drop energy has local mimima for zero deformation (cf. Eq. (2.2)), i. e. spherical ground states are predicted, in contrast to observation. Secondly, the liquid-drop is stable against asymmetric deformation for all $x > 0.39$ [34], and can therefore not explain the favoured asymmetric mass splits characteristic for fission of the actinides, which have $0.68 < x < 0.76$. The asymmetric mass distribution in the fission of actinides is the first clue that quantum mechanic shell effects play an important role in the fission process. Throughout the actinide region the heavy-mass peak stays quite constantly centered around masses corresponding to the closed spherical neutron shell at $N = 82$, while the light mass peak is moving linearly with the mass number of the fissioning nucleus. Pure microscopic treatments of the fission process are difficult, due to the large number of degrees of freedom. Therefore, a combination of the macroscopic liquid-drop model and a simplified microscopic treatment is commonly used. The so-called shell-correction method, or Strutinsky procedure (after its inventor [35]), uses a renormalization of single-particle energies in deformed potentials to the liquid-drop energy. The single particle energy levels are replaced by a smooth distribution of states that resembles the single particle-density of states, but with the actual shell structure washed out. A typical fission barrier for an ac-

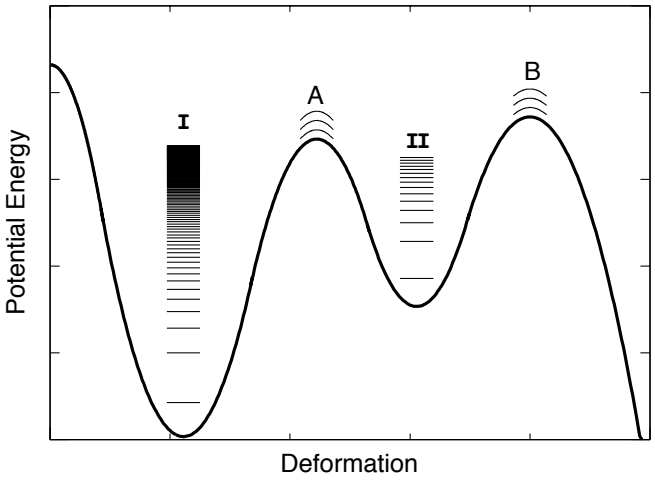

Fig. 2.2: *Schematic representation of a double-humped fission barrier. With states in the first (I) and second (II) wells as well as transition states above the inner (A) and outer (B) barriers.*

tinide nucleus, calculated according to the Strutinsky procedure, is illustrated schematically in Fig. 2.2. The most interesting feature, aside from the correctly reproduced deformed ground state, is the existence of a minimum at deformation corresponding to the liquid-drop saddle point. The double-humped structure of the fission barrier has led to a better understanding of many features of low-energy fission, most strikingly it gave a natural explanation for spontaneously fissioning isomers, discovered a few years before the theory had been developed. The first such isomer was discovered by Polikanov et al. [36], a state in ^{242}Am with a half life of 14 ms and with spontaneous fission as its principal mode of decay. The spontaneous fission half-life of this isomer was appropriate to a state with an excitation energy of several MeV, so its peculiar property was its stability agains gamma decay. The fission- or shape isomers could be explained within the concept of the double humped fission barrier as meta-stable states in the second minimum that decay through either fission, by tunneling the outer barrier, or gamma-decay back to the ground state, by tunneling the inner barrier. Another influence of the double humped barrier is on the resonance structure in the fission cross section. In nuclei that normally have very small fission cross sections for thermal neutron capture compared to radiative capture cross sections, narrow bands of resonances have been found that have fission cross sections comparable with radiative capture cross sections [37, 38]. These bands can be understood as due to states in the second well of the fission barrier. For a given energy, the density of states in the second well is much lower than that in the first well. States in the second well also

have a higher probability for fission and consequently larger widths. The coupling of the broader states in the second well with the narrow closely spaced states in the first well lead to the narrow bands of resonances with large cross sections for fission.

The inclusion of shell corrections to the liquid-drop model alone does not explain the asymmetric mass distribution observed in fission in the actinide region. However, it is found that the inclusion of reflection asymmetric P-odd deformations have a strong effect on the outer fission barrier and in this way offer a natural, qualitative explanation of observed mass distributions. In detailed calculations of the potential energy of deformed nuclei, well defined valleys have been found [7]. The valleys lead to separate scission configurations and give rise to different so-called fission modes that make up separate parts of the mass and total kinetic energy (TKE) distributions. The model based on these potential energy calculations is called the Multi-Modal-Random-Neck-Rupture (MM-RNR) model and will be discussed in further detail in Sect. 2.3.2.

2.2 Theory of Fission Fragment Angular Distributions

At excitation energies near the fission-barrier, fragment angular distributions can be explained using Bohr's fission-channel concept [39]. On the top of the barrier most of the excitation energy has been absorbed into deformation, therefore a discrete spectrum of low-lying collective excitations can be expected to exist there. Within Bohr's fission-channel concept, near-barrier fission proceeds through these so-called transition states. With the assumptions that fission proceeds along the symmetry axis of the deformed nucleus and that the projection K of the angular momentum J on this axis is conserved during the path from saddle point to scission, the angular distribution of fission fragments are determined by the quantum numbers J and K of the involved transition states. The differential cross section for fission through a particular transition state (J^π, K) is [34]

$$\left(\frac{d\sigma}{d\Omega}\right)_{J^\pi,K} = \sum_{M=-J}^{J} \phi_f(J^\pi, K, M; E) \cdot W^J_{M,K}(\theta), \tag{2.5}$$

where J^π is angular momentum and parity of the transition state, K the projection of J on the symmetry axis, M the projection of J on the quantization axis (which is parallel to the photon beam), E is the excitation energy and θ is the angle between the symmetry axis and the quantization axis, see Fig. 2.3. The angular distribution patterns are given by the function $W^J_{M,K}(\theta)$, which are related to the rotational wave functions $d^J_{M,K}(\theta)$ by

$$W^J_{M,K}(\theta) = \frac{2J+1}{2} \cdot |d^J_{M,K}(\theta)|^2,$$

and normalized according to $\int_0^\pi W^J_{M,K}(\theta) \sin\theta d\theta = 1$. The partial cross section of a transition state (J^π, K) with spin projection M is given by $\phi_f(J^\pi, K, M; E)$. In the case of an

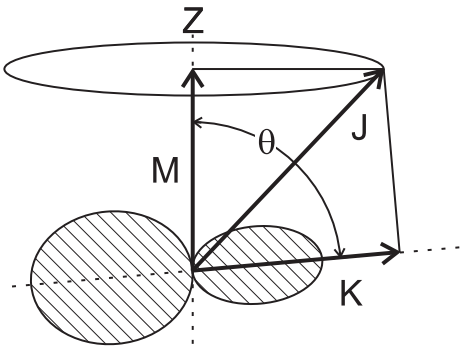

Fig. 2.3: *Geometrical representation of a moment in time of the fissioning nucleus. J, M and K are the total angular momentum, its projection on the quantization axis Z and its projection on the symmetry axis of the nucleus, respectively. The angle between the symmetry axis and the quantization axis is denoted θ.*

even-even target nucleus the J^π of the transition states are given by the multipole order of the excitation. Low-energy photon absorption is mainly due to electric dipole (E1) and to lesser extent electric quadrupole (E2) and magnetic dipole (M1) transitions leading to excited states with $J^\pi = 1^-, 2^+, 1^+$, respectively. For real photons only substates with $M = \pm 1$ are populated, and for unpolarized photons $\phi_{\gamma,f}(J^\pi, K, M; E) = \phi_{\gamma,f}(J^\pi, K, -M; E)$. The cross section for fission through a transition state (J^π, K), obtained from Eq. (2.5) by summing over the M substates and integrating over θ is then

$$\begin{aligned}\sigma_{\gamma,f}(J^\pi, K, E) &= \sum_{M=-J}^{J} \phi_{\gamma,f}(J^\pi, K, M, E) \\ &= 2 \cdot \phi_{\gamma,f}(J^\pi, K, \pm 1, E). \end{aligned} \tag{2.6}$$

Furthermore, the angular distribution pattern exhibits the symmetry relation $W^J_{M,K}(\theta) = W^J_{-M,K}(\theta)$ so that Eq. (2.5) for low-energy photofission becomes

$$\begin{aligned}\left(\frac{d\sigma_{\gamma,f}}{d\Omega}\right)_{J^\pi,K} &= 2 \cdot \phi_{\gamma,f}(J^\pi, K, \pm 1; E) \cdot W^J_{\pm 1,K}(\theta) \\ &= \sigma_{\gamma,f}(J^\pi, K, E) \cdot W^J_{\pm 1,K}(\theta). \end{aligned} \tag{2.7}$$

The angular distribution pattern are represented by a series of terms $\sin^2 n\theta$, restricting the possible multipolarities to $L \leq 2$,

$$W^J_{\pm 1,K}(\theta) = a + b \sin^2\theta + c \sin^2 2\theta. \tag{2.8}$$

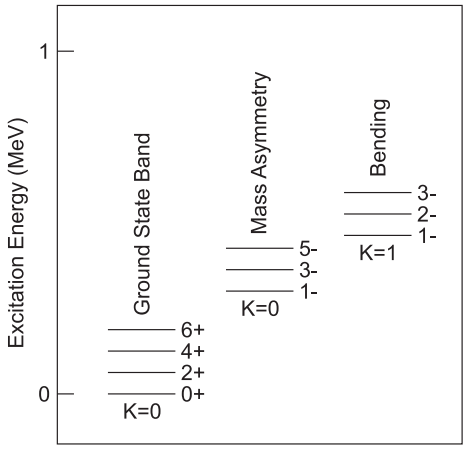

Fig. 2.4: *Expected spectrum of transition states above the barrier of an even-even nucleus accessible in photofission (schematically), according to Ref. [40].*

The experimentally observable differential cross section is a linear combination of $W^J_{\pm 1,K}(\theta)$ terms for the involved transition states

$$\frac{d\sigma_{\gamma,f}(E_\gamma,\theta)}{d\Omega} = A_\gamma + B_\gamma \sin^2\theta + C_\gamma \sin^2 2\theta. \tag{2.9}$$

Using Eq. (2.7) and calculated values for the expansion coefficients [34], taking the degeneracy of $K \neq 0$ into account, one obtains

$$\begin{aligned}
A_\gamma(E_\gamma) &= \frac{1}{4}\left[3\sigma_{\gamma,f}(1^-,1) + 3\sigma_{\gamma,f}(1^+,1) + 5\sigma_{\gamma,f}(2^+,1)\right] \\
B_\gamma(E_\gamma) &= \frac{1}{8}\left[6\sigma_{\gamma,f}(1^-,0) - 3\sigma_{\gamma,f}(1^-,1) - 3\sigma_{\gamma,f}(1^+,1) - 5\sigma_{\gamma,f}(2^+,1) + 5\sigma_{\gamma,f}(2^+,2)\right] \\
C_\gamma(E_\gamma) &= \frac{5}{8}\left[\frac{3}{2}\sigma_{\gamma,f}(2^+,0) - \sigma_{\gamma,f}(2^+,1) + \frac{1}{4}\sigma_{\gamma,f}(2^+,2)\right].
\end{aligned}$$

Obviously, the cross sections of all the transition states cannot be disentangled from the observed angular distributions. It is common practice to restrict the analysis of photofission fragment angular distributions to the theoretically predicted lowest-lying transition state bands; ground state, mass asymmetry and bending [40] as illustrated in Fig. 2.4, resulting in $(J^\pi, K) = (2^+,0), (1^-,0)$ and $(1^-,1)$, respectively.

Some useful relations following from the above discussion are worth mentioning here:

- The ratio B_γ/A_γ is connected to the anisotropy by

$$B_\gamma/A_\gamma = \frac{d\sigma_{\gamma,f}(90^\circ)}{d\Omega} \Big/ \frac{d\sigma_{\gamma,f}(0^\circ)}{d\Omega} - 1, \tag{2.10}$$

and in the case of pure dipole fission ($C = 0$), B_γ/A_γ also determines the ratio of the cross section for fission through the $K = 1$ and $K = 0$ transition states

$$B_\gamma/A_\gamma = \frac{\sigma_{\gamma,f}(1^-, 0)}{\sigma_{\gamma,f}(1^-, 1)} - \frac{1}{2} \qquad (C_\gamma = 0). \tag{2.11}$$

- With the analysis restricted to the lowest $K = 0$ fission-channels, the ratio C_γ/B_γ determines the relative quadrupole-to-dipole contribution

$$C_\gamma/B_\gamma = \frac{5\sigma_{\gamma,f}(2^+, 0)}{4\sigma_{\gamma,f}(1^-, 0)} \qquad (K = 0). \tag{2.12}$$

The concept of the double humped fission barrier is well established. At the inner barrier the deforming nucleus shows mirror-symmetric and axially asymmetric shapes, while at the outer barrier mirror asymmetric shapes with axial symmetry. Because of the mirror-symmetric shape at the inner barrier, the $(J^\pi, K) = (2^+, 0)$ channel in even-even actinide nuclei will be substantially lower (about 0.5 MeV) than the $(J^\pi, K) = (1^-, 0)$ channel. At the outer barrier there will be a degeneracy of the $(J^\pi, K) = (2^+, 0)$ and the $(J^\pi, K) = (1^-, 0)$ channels, due to the mirror-asymmetric shape of the nucleus. Because low-energy photon absorption is predominantly E1, there will be a fast decrease in the fission cross section at the higher of the two $(J^\pi, K) = (1^-, 0)$ barrier humps. In case of a higher inner barrier this will be accompanied with an increase in C/B ratio. For a lower inner barrier the increase in the C/B ratio is expected to start below the fast increase in the fission cross section. The ratio of quadrupole to dipole fission (measured by the C/B ratio) will thus be governed by the inner barrier, while the behaviour of the B/A ratio will be determined by the outer barrier [40, 41].

2.3 Models of Fission-Fragment Mass Distributions

Although many attempts have been made to model fission mass distributions qualitatively, a quantitative description of all fission characteristics is not available yet. In order to model fission fragment mass distributions, it is necessary to understand the motion of nucleons from the saddle point to scission. Models of fission fragment mass distributions can be classified as either microscopic, stochastic or deterministic [42]. The microscopic treatment is the most complete, since it would involve solving equations of motion for each individual nucleon in the fissioning nucleus. This is in general too complicated, and approximations must be applied. From microscopic treatments some conclusions about the scission process can be drawn, but due to the large computational difficulties little quantitative predictions can be made. In a stochastic treatment the number of variables is reduced by assuming the dynamics to be restricted to the time evolution of a set of collective variables. Due

to their complexity stochastic models exist only for a few limiting cases. Deterministic models are based on microscopic-macroscopic descriptions of the nucleus, usually using the Strutinsky shell-correction method. Deterministic models are still the ones that are most successful in describing both global aspects and details of mass distributions. Two of the most successful deterministic models are discussed in the following sections.

2.3.1 Scission-Point Model

In the scission-point model of Wilkins et al. [43] it is assumed that the fission-fragment distributions can be determined from the potential energies of the complementary fragment pairs at the scission point. This implies an equilibrium among the collective degrees of freedom, characterized by a collective temperature T_{coll}, and a separate equilibrium among the intrinsic degrees of freedom, characterized by an intrinsic temperature T_{int}. This assumption leads to an exponential relationship between the probability P of a fission event, characterized by the collective degrees of freedom, and the sum of the collective coordinates' potential and kinetic energies. The collective kinetic energies are calculated by assuming that, for a particular choice of the scission-point configuration, the kinetic energies are independent of the collective variables. The scission-point configuration consists of two coaxial spheroids, whose tips are separated by a distance d. Because of this assumption it is possible to calculate the probability for a fission event from the individual potential energies of the fragments at the scission point as

$$\begin{aligned} P = \int_{\beta_L=0}^{\beta_{max}} \int_{\beta_H=0}^{\beta_{max}} \exp\big\{ - \big[& V_{C,N}(N_L, Z_L, \beta_L, N_H, Z_H, \beta_H, d) \\ & + V_L(N_L, Z_L, \beta_L, T_{int}) \\ & + V_H(N_L, Z_L, \beta_L, T_{int})\big]/T_{coll}\big\} d\beta_L d\beta_H \quad , \end{aligned} \tag{2.13}$$

where $N_{L,H}$ and $Z_{L,H}$ are neutron and charge numbers of the light and heavy fragments, respectively, and $\beta_{L,H}$ are the corresponding deformation parameters. The potential $V_{C,N}$ is the fragments mutual Coulomb and nuclear interaction and the potentials $V_{L,H}$ are the individual potential energies of the fragments, each consisting of a liquid-drop part with shell and pairing corrections. In the absence of shell effects, the potential energies $V_{L,H}$ show broad minima as functions of deformation at about $\beta_{L,H} \approx 0.6$. Shell corrections in the vicinity of this minimum will therefore play a major role. Furthermore, a spherical configuration of one of the fragments can only be achieved at a considerable cost in the liquid-drop energy, and only be partially compensated by deformation of the second fragment. The major contributions from the shell and pairing corrections comes from two neutron shells; a spherical one at $N = 82$ and a deformed ($\beta \approx 0.65$) one at $N \approx 88$. The interplay of these neutron shells and the favoured symmetric mass split from the liquid-drop part of Eq. (2.13) allows a qualitative explanation for many features of mass and

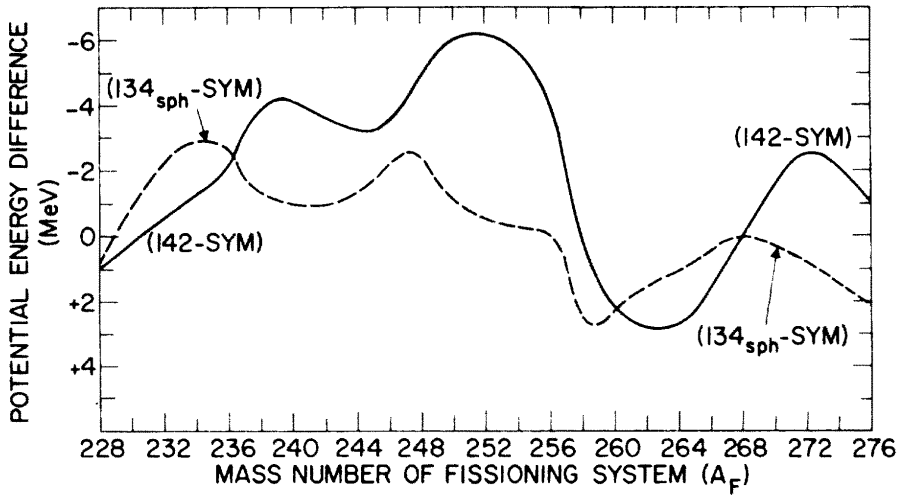

Fig. 2.5: *Difference in the minimum potential energy of asymmetric mass splits (solid line: $A_H = 142$, dashed line $A_H = 134$) to that of symmetric mass splits according to the scission-point model, plotted as a function of the compound-nucleus mass. Figure reprinted from Ref. [43], with permission. Copyright (1976) by the American Physical Society.*

kinetic energy distributions. In Fig. 2.5 the difference in potential energy of asymmetric and symmetric mass splits is shown as a function of the mass number of the fissioning nucleus. Although the scission-point model can explain many qualitative features of fission, it is hardly useful for quantitative predictions [42]. Generally, the calculated mass yield curves come out too narrow and slightly displaced. Furthermore, theoretical arguments against the purely static version of the scission-point model have been raised [44].

2.3.2 Multi-Modal Random-Neck-Rupture Model

The Multi-Modal Random-Neck-Rupture (MM-RNR) model [7] is the first theoretical model that has been able to deliver quantitative predictions of fission fragment mass distributions in agreement with experimental observation. It has been successful in describing mass and energy distributions of fission fragments from a wide range of nuclei from ^{213}At to ^{258}Fm, see Ref. [7] and references therein. The model has been used to interpret the experimental results and will be described in some detail in this section.

The theory of multi-modal fission is based on potential energy calculations of the deforming nucleus. Using a Strutinsky-type procedure, the potential energy of the nucleus is

$$E_{pot} = E_{LQD} + E_{micro}, \tag{2.14}$$

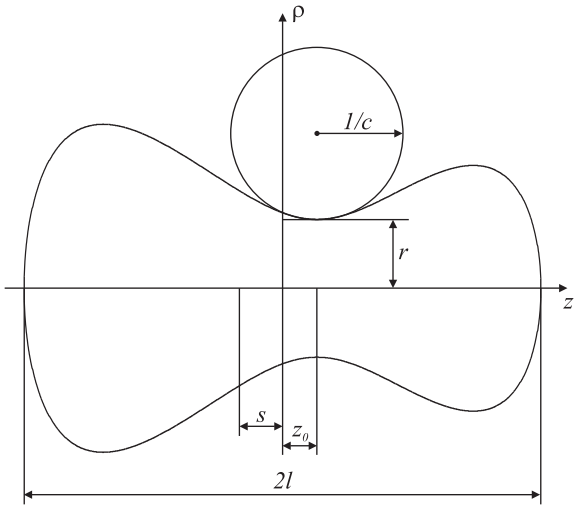

Fig. 2.6: *Parameterization of the nuclear shape according to Eq. (2.15).*

where E_{LQD} is a liquid-drop term that accounts for more than 99% of the potential energy, while E_{micro} is a relatively small correction term that takes shell and pairing effects into account. The shell corrections are calculated using a Woods-Saxon single-particle potential. The shape of the nucleus is parameterized using axially symmetric Lawrence shapes, in cylindrical coordinates

$$\rho^2(z) = (l^2 - z^2) \sum_{n=0}^{N} a_n (z - z_0)^n. \tag{2.15}$$

The coefficients a_n are replaced by geometric parameters (l, r, z_0, c, s):

- The semi-length l measures the elongation of the nucleus,
- the radius of the neck is r,
- the position of the neck is z_0,
- the curvature of the neck is c, and
- the position of the center of mass is s,

as illustrated in Fig 2.6. The relation between the coefficients a_n and the geometric parameters are fixed by analytical expressions. From the calculations, pathways in the potential energy landscapes are found that determine the motion of the nucleus. Each pathway corresponds to a fission mode. The different modes show different shapes of the nucleus at the scission point, and therefore each mode has a characteristic mass and total kinetic energy (TKE). The model up to this point does not explain the widths of mass and TKE distributions. To explain such features a scission mechanism is needed; in the MM-RNR model this

mechanism is random neck rupture. Experiments with macroscopic liquid-drops show that, as the drop is deformed, a long flat neck is formed that ruptures at random positions [45] because of surface vibrations along the neck. The drop becomes unstable when the total length of the drop $2l$ becomes larger than 11 times the neck radius r, which is known as the Rayleigh condition. The probability that the neck ruptures at a position z_r instead of at position z_0, where the neck is thinnest, is governed by the potential-energy difference $E(z_0) - E(z_r)$. The model uses a Boltzmann distribution for the rupture probability

$$P(A) \propto \exp\left[-2\pi\gamma_0(\rho^2(z_r) - \rho^2(z_0))/T\right], \tag{2.16}$$

where γ_0 is the liquid-drop surface-tension coefficient and T is the nuclear temperature of the pre-scission shape. Although the probability distribution for a certain mass split in the MM-RNR model is similar in form to that of the scission-point model, the random neck rupture is able to reproduce experimentally observed widths of the mass distributions. The difference is that in the MM-RNR model the deciding factor is not the potential energy of the forming fragments, as in the scission-point model, but rather the energy of surface oscillations that vary slowly enough to allow mass splits further from the most probable mass split.

The results of calculations within the MM-RNR model are the involved fission modes and their characteristic mass and TKE distributions. For the light actinide nuclei the number of modes are in most cases three; a mass symmetric so-called super-long (SL) mode and two mass asymmetric so-called standard modes (S1, S2). The S1 and S2 modes' mass distributions are centered around heavy fragment masses 135 and 141 and may be associated with the neutron shell closures at $N = 82$ and $N \approx 88$ of the scission-point model, respectively. The model does, however, not predict the probability with which the different modes appear, other than through rough estimates based on the different barrier heights. Comparison of experimental data with calculation is done using a fit function for each predicted mode. This procedure was used to interpret the data in this thesis and is described in Sect. 6.2.

In order to predict fission-fragment mass distributions, a combination of the MM-RNR model and cross-section calculations using a statistical model and a static fission barrier has been suggested by Ref. [11, 46]. While the original calculations by Brosa et al. [7] predicts a bifurcation point of the standard modes beyond the saddle point, more recent calculations of the nuclear potential landscape [8, 9] has suggested that the two standard modes bifurcate in the second minimum of the fission barrier. The inclusion of mode specific outer barriers in calculations of the transmission through a double humped barrier could therefore be used to predict mass distributions. To this end barrier heights and curvatures are found by fitting experimental mode-weighted cross section data, which are then used to predict mode weight dependence as a function of excitation energy. The predictive power of the model has been demonstrated in Ref. [12]. However, conclusive evidence for separate outer barriers of the two standard modes are still missing.

2.3.3 Mass Dependence of Angular Distributions

In the discussion of the theory of fission-fragment angular distributions (Sect. 2.2) no dependence on the fission fragment mass of the angular distributions is taken into account. However, mass dependence of the angular distributions has been observed experimentally [47, 48]. An intuitive explanation for this phenomenon is offered within the concept of multi-modal fission. Since this model describes the fission fragment mass and TKE distributions as the result of fission through different paths along the multi-dimensional landscape of the fission barrier, depending on where on the path to fission the modes bifurcate a distinct barrier can be associated with each mode. Since the position of the transition states depends strongly on the shape and height of the fission barrier, a distinct angular distribution can be expected for each fission mode. Because each mode also has a distinct mass and TKE distribution, a dependence of the angular distribution according to

$$W(A, \mathrm{TKE}, \theta) = \sum_m W_m(\theta) \cdot Y_m(A, \mathrm{TKE}), \tag{2.17}$$

can be expected [49]. The angular distribution of each mode $W_m(\theta)$ is given by Eq. (2.9) and the yield of each mode $Y_m(A, \mathrm{TKE})$ can be determined from a fit to experimental $Y(A, \mathrm{TKE})$ data.

Chapter 3

Experiments

The fission fragment mass, TKE and angular distributions in the bremsstrahlung-induced fission of ^{232}Th, ^{234}U and ^{238}U have been studied by means of the double-kinetic-energy ($2E$) technique. The fission fragment detector was a twin Frisch-grid ionization chamber (FGIC), its working principles are discussed in detail in Sect. 3.2. The fission targets were placed in a hole in the central cathode of the FGIC. The targets themselves consist of UF_4 or ThF_4 that have been vacuum-evaporated onto thin polyimide foils, the target spot is circular with a diameter of 30 mm. Thin gold layers (50 μg/cm^2) evaporated onto the opposite sides of the polymide foils serve to electrically separate the two chamber sides. The experiments were divided in two measurement series. In the first one, experiments on ^{234}U and ^{238}U were performed. The ionization chamber was placed at 45° angle relative to the beam axis, in order to maximize the fission yield in the angular cone of events accepted in the analysis (cf. Sect. 4.3.2). The determination of the angular distribution in this setting was therefore limited (cf. Appendix A). In addition one measurement without a target was performed in order to investigate possible background-induced false events: During an 11-hour run at a bremsstrahlung energy of 6.8 MeV and a beam current of about 40 μA, no events were detected. The investigation of the photofission of ^{234}U was continued in the second measurement series, which also included the investigation of the photofission of ^{232}Th. In this measurement series the ionization chamber was placed so that the target normal coincided with the beam axis. A summary of the experimental parameters is given in Tab. 3.1. The table includes the targets measured, the orientation of the FGIC with respect to the beam axis, measurement times and average electron beam currents as well as the total number of fission events accepted in the analysis.

Tab. 3.1: *Summary of the performed experiments. The first column gives the target nucleus, the second and third columns the thickness of target layer and polymide backing, respectively. The fourth column gives the orientation of the fission fragment detector relative to the beam axis. The electron beam energy E_0, the average current $\langle I \rangle$, the beam time T for each measurement and the number of events NEV accepted in the analysis for the fission fragment mass and* TKE *distributions are given in the following columns.*

Target Nucleus	Target Thickness (μg/cm^2)	Polyimide (μg/cm^2)	Detector Orientation	E_0 (MeV)	$\langle I \rangle$ (μA)	T (h)	NEV
^{238}U	130.3±6.5	35.0±3.0	45°	8.5	19	17	42288
				7.0	43	20	17594
				6.5	48	82	25403
^{234}U	190.0±0.9	32.0±1.0	45°	9.0	23	43	682765
				7.5	5	99	6659
				6.8	11	93	3916
^{238}U	82.9±4.2	35.0±3.0	0°	8.5	18	22	46715
^{232}Th	87.0±5.0	35.2±0.7	0°	9.5	15	22	47957
				8.0	20	29	15434
^{234}U	46.6±0.3	32.0±1.5	0°	9.0	23	21	28185
				7.5	12	96	16411
				6.4	29	81	3541

3.1 Bremsstrahlung Facility

As mentioned before, the experiments were performed at the Darmstadt High-Intensity Photon Setup (DHIPS [50, 51]), located at the end of the superconducting injector linac of the S-DALINAC (Superconducting Darmstadt linear accelerator [13]). The electrons for acceleration are drawn from a high-voltage terminal at 250 kV. A chopper-prebuncher section produces the time structure required for acceleration in the injector linac, from the electro-statically pre-accelerated beam. In the injector linac the electron beam is then accelerated up to 10 MeV in superconducting niobium cavities, operated in liquid helium at 2 K. The beam leaving the injector can then either be bent by 180° for injection into the main linac for further acceleration up to 130 MeV, or as in these experiments be used at the end of the injector. In the latter case the electrons exit the accelerator vacuum through a thin (0.13 mm) aluminum window and hit a radiator that produces the bremsstrahlung photons for the experiments. The radiator consists of four copper sheets. By measuring the absorbed current in each sheet it is possible to monitor both the electron current and energy online [52]. Before reaching the fission target, placed inside the fission fragment detector ca. 1.5 m behind the radiator, the bremsstrahlung from the radiator is collimated in a 955 mm long copper collimator. The photon beam-spot at the target position is 30 mm in diameter, as determined via a picture on radiographic film [51].

3.2 Fission-Fragment Detector

In order to detect the fission fragments, a twin Frisch-grid ionization chamber (FGIC) was employed. This detector consists of two ionization chambers with Frisch grids placed back to back on a common cathode. A schematic illustration of the detector geometry is given in Fig. 3.1. The cathode and grid are separated by a distance of 3 cm, while the anode-grid distance is 0.5 cm. The volume between the electrodes is filled with P-10 gas (90 % Ar + 10 % CH_4) at a pressure of 1.05 bar, continuously flowing through the chambers at a flow rate of about 60 ml/min. The cathode has a circular hole in the center where a transparent fission target is placed. With exception of the target itself (which has a sample and a backing side), the detector is mirror symmetric with respect to the cathode. In the following discussion of the chamber's working principles, only one side is therefore considered.

As a fission fragment is stopped in the gas-filled volume between the ionization chamber's electrodes, it leaves a number of electrons and positive ions in its path. To the first approximation the number of electron-ion pairs is proportional to the energy deposited in the gas. To separate the electrons from the ions, a negative electric potential (-1.6 kV) is applied to the cathode, while the grid is kept at ground potential. The negatively charged electrons then proceed to drift in the opposite direction of the electric field towards the

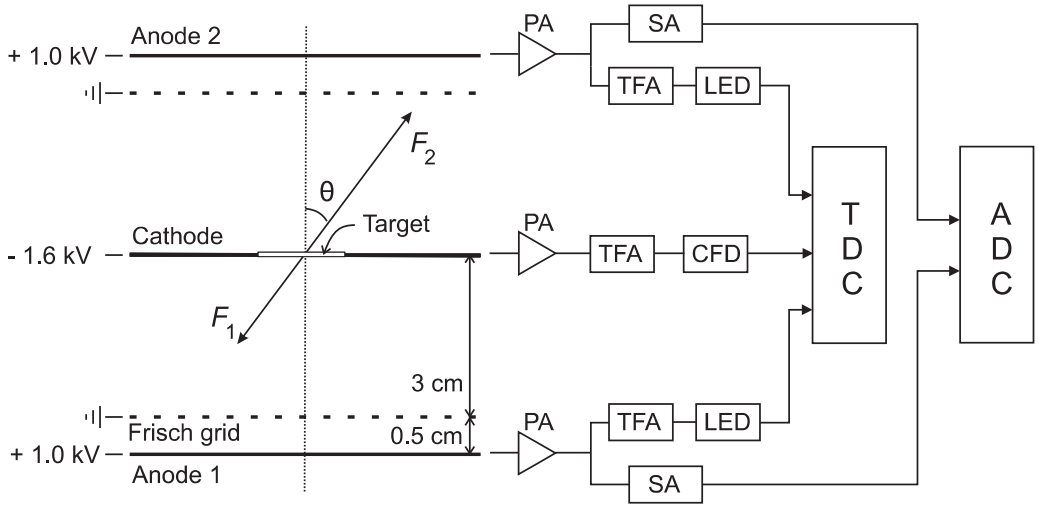

Fig. 3.1: *Schematic illustration of the detector and associated electronics. The abbreviations denote: PA – charge-sensitive preamplifier, SA – spectroscopy amplifier, TFA – timing-filter amplifier, LED – leading-edge discriminator, CFD – constant-fraction discriminator, TDC – time-to-digital converter, ADC – analog-to-digital converter.*

anode, which is held at a positive electric potential (+1.0 kV). Due to lower mobility of the comparatively massive positive ions, they can be considered as stationary during the time it takes to collect the electrons from an event [53]. Hence, when all electrons from the event are collected on the anode, a track of positive ions is left in the chamber volume. If the Frisch grid was not present, a charge, of opposite sign to the collected electron charge, would be influenced on the anode. This would render the ionization chamber useless for spectroscopic purposes. The grid serves the purpose of dividing the chamber into two (ideally) separate parts; the interaction region between cathode and grid where the fission fragments deposit their energy, and the collection region between anode and grid where no ionization should take place. The grid cannot, however, shield the collection region perfectly from charge induction by charge carriers in the interaction region. This causes a slight position dependence of the anode signal, which is generally referred to as grid inefficiency (GI). The problem of the position dependence in terms of positive ions influencing a charge on the anode was solved by Bunemann et al. [54], which offered a useful correction method for analog signals. In the last decades, however, it has become increasingly common to use pulse-shape digitizers to store the entire anode signal for offline-analysis. For this purpose it is vital to understand how the grid inefficiency affects the pulse shape. In Ref. [55] an attempt was presented to determine the GI experimentally from the shape of the anode signal. The shape of the signal was traced back to drifting electrons inducing charge on the anode. An expression for the final pulse height of the anode was given that differs from the one presented in Ref. [54]. Furthermore, it was shown how the

experimentally measured values of the GI differed from values calculated according to the recipe of Bunemann et al. [54], and the desire for a more detailed method of calculation was expressed. However, the description of the influence of the GI on the shape of the anode signal used in Ref. [55] is incorrect, since it leads to an anode charge signal, which is larger than the collected charge. Their results may therefore be questioned. In the following subsections the pulse-shapes from—and the effect of the grid inefficiency on—the different electrodes of the FGIC will be derived based on the Shockley-Ramo theorem [56,57].

3.2.1 Signal Generation: The Shockley-Ramo Theorem

As the electrons drift in the electric field towards the anode, they induce current on the three electrodes of the chamber. According to the Shockley-Ramo theorem [56, 57], the current induced on a conductor k due to an electron moving with velocity $\vec{v}$ is given by

$$i_k = -e\,\vec{v}\cdot\vec{E}_k, \tag{3.1}$$

where $-e$ is the electron charge, and $\vec{E}_k$ is the electric field that would exist at the position of the electron under the following circumstances: all charge carriers are removed, the conductor k is held at unit potential, and all other conductors are grounded. The field $\vec{E}_k$ is referred to as the weighting field, and should not be confused with the actual electric field that exists due to the applied potentials and the distribution of charges inside the chamber. The current i_k will cause a current to flow in the opposite direction through the electronic circuit connected to the electrode. The integration of this current on a charge sensitive preamplifier produces an output signal proportional to

$$\Delta Q_k = -\int i_k dt = -e[\varphi_k(\vec{r}) - \varphi_k(\vec{r}_0)], \tag{3.2}$$

where φ_k is the potential existing between the conductors under the same conditions as for the weighting field, $\vec{r}$ is the electron's current position and $\vec{r}_0$ its origin. With this definition of the charge signal only moving charge carriers contribute, therefore the positive ions does not need to be taken into account. The potential φ_k is called a weighting potential and can be calculated by solving the Laplace equation

$$\nabla^2\varphi_k = 0 \tag{3.3}$$

under the boundary conditions $\varphi_k = 1$ on conductor k and $\varphi_k = 0$ on any other conductor.

3.2.2 Weighting Potential Distributions

For the simple case of an idealized parallel wire grid chamber, as illustrated in Fig. 3.2, approximate analytic solutions to Eq. (3.3) can be found using the method of images [58].

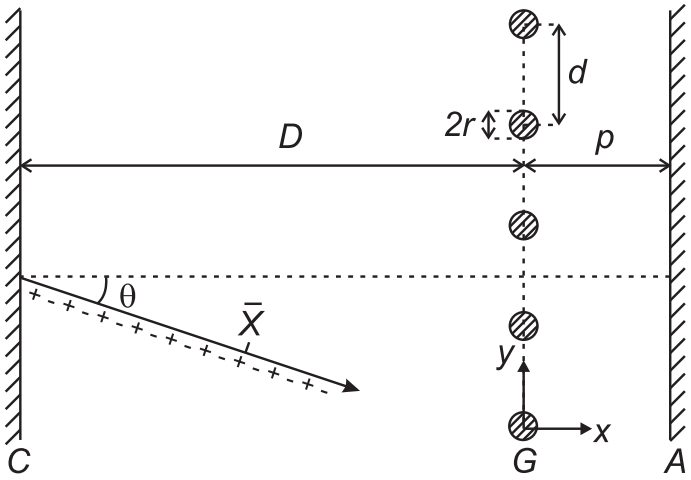

Fig. 3.2: *Schematic illustration of the three-electrode geometry of the Frisch-grid ionization chamber, consisting of a cathode C, a grid G and an anode A. An ionizing particle is emitted from the cathode at an angle θ relative to the chamber normal, creating a track of electrons and positive ions. The center of gravity of the electron distribution along this track is denoted by $\bar{X}$.*

To find the weighting potential, one first considers the case of a periodic distribution of line charges placed along the y-axis at $x = 0$ and a grounded conducting plate at $x = p$, causing a mirror image of the line charge distribution at $x = 2p$. The potential due to this configuration is given by

$$\varphi_0'(x,y) = -\alpha \ln \left[\frac{\sin^2(\pi \frac{y}{d}) + \sinh^2(\pi \frac{2p-x}{d})}{\sin^2(\pi \frac{y}{d}) + \sinh^2(-\pi \frac{x}{d})} \right]. \tag{3.4}$$

Circular equipotentials of radius r are found around each line charge, assuming $r \ll d \ll p$. By adjusting the line charge density α, the distribution of line charges can therefore simulate a grid with wire radius r at unit potential. The potential due to a grounded grid and a conducting plate at unit potential is then given by

$$\varphi_0(x,y) = 1 - \frac{1}{2\ln(\frac{d}{2\pi r}) + 4\pi \frac{p}{d}} \ln \left[\frac{\sin^2(\pi \frac{y}{d}) + \sinh^2(\pi \frac{2p-x}{d})}{\sin^2(\pi \frac{y}{d}) + \sinh^2(\pi \frac{x}{d})} \right]. \tag{3.5}$$

Far from the grid the potential reaches an asymptotic value

$$V_0 := \lim_{x \to -\infty} \varphi_0(x,y) = \frac{2\ln(\frac{d}{2\pi r})}{2\ln(\frac{d}{2\pi r}) + \frac{4\pi p}{d}}. \tag{3.6}$$

Combining this with a linear function to satisfy boundary conditions at both anode ($\varphi_A = 1$) and cathode ($\varphi_A = 0$) the final anode weighting potential due to the system of electrodes

of the FGIC may be approximated as

$$\varphi_A(x) = \begin{cases} \sigma\left(1 + \dfrac{x}{D}\right) , & \text{if} \quad -D < x < 0 \\ \sigma + (1-\sigma)\dfrac{x}{p} , & \text{if} \quad 0 < x < p \end{cases} , \qquad \text{with } \sigma = \frac{V_0}{1 + V_0 \frac{p}{D}}. \tag{3.7}$$

The weighting potential of the cathode can be found in the same manner, but due to the large cathode-grid distance, the asymptotic potential (Eq. (3.6)) for the cathode at unit potential is small and may, hence, be neglected. The cathode weighting potential is then

$$\varphi_C(x) = \begin{cases} -\dfrac{x}{D} , & \text{if} \quad -D < x < 0 \\ 0 , & \text{if} \quad 0 < x < p \end{cases} . \tag{3.8}$$

The grid weighting potential φ_G follows by noting that $\varphi_C + \varphi_G + \varphi_A = 1$ for all (x, y) as

$$\varphi_G(x) = \begin{cases} (1-\sigma)\left(1 + \dfrac{x}{D}\right) , & \text{if} \quad -D < x < 0 \\ (1-\sigma)\left(1 - \dfrac{x}{p}\right) , & \text{if} \quad 0 < x < p \end{cases} . \tag{3.9}$$

As evident by the above discussion, analytical calculation of the weighting potentials need numerous approximations. For more accurate results one may therefore use numerical methods to solve the Laplace equation. One numerical method that offers the advantage of simplicity and availability of computer software for defining geometries and other parameters is the finite element method (FEM). In this work the computer software package Elmer [59] was used to calculate weighting potentials for two different types of grids at several anode distances. The calculations of the weighting potentials for the parallel wire grids were performed over one grid period $y \in [0, d]$ for the geometry given in Fig. 3.2, for a number of elements in the xy-plane. At $y = 0$ and $y = d$ periodic boundary conditions were imposed and, as required by Eq. (3.3), the boundary conditions were unity at $x = p$ and zero at $x = -D$ as well as at $x^2 + y^2 = r^2$ and $x^2 + (y - d)^2 = r^2$. The size of the elements was successively decreased until the change in the results became considerably smaller than the uncertainties of the corresponding experimental values. Eventually, the size of the elements in the vicinity of the grid wires was a fourth of the cross-section area of the wires. The result of such a calculation projected onto the x-axis is shown in Fig. 3.3. Evidently, the form of the numerical solution is well represented by Eq. (3.7), with the parameter σ taken as the linear extrapolation of the weighting potential from $x \ll 0$ to $x = 0$.

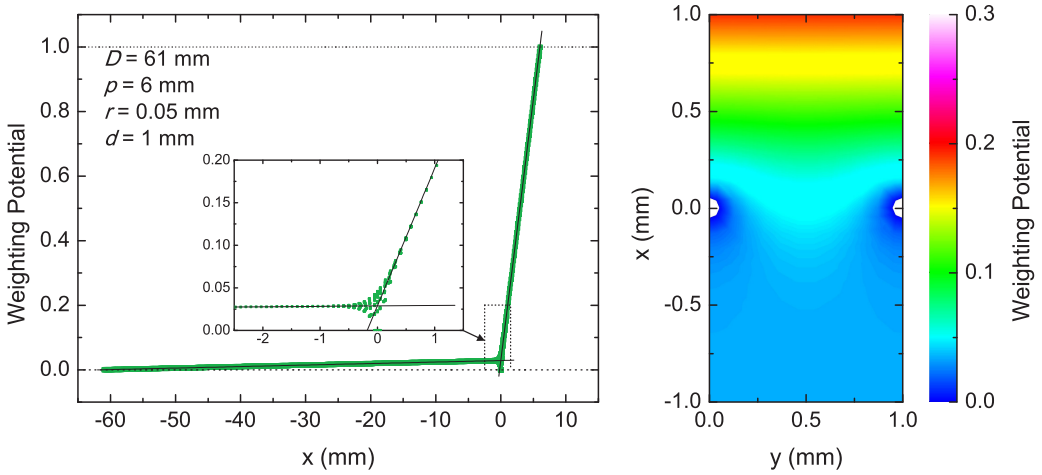

Fig. 3.3: *Left: Calculated weighting potential projected onto the x-coordinate as indicated in Fig. 3.2. The two solid lines represent linear fits to the regions $|x| > 2d$, where d is the distance between the grid wires. Also indicated are values of the geometry parameters as defined in Fig. 3.2. The inset zooms into the region $|x| \approx 0$ and shows a slight y-dependence of the weighting potential there. Right: The weighting potential as a function of the x- and y-coordinates around the grid wires.*

3.2.3 Charge Signals

The charge-signal amplitude is obtained by integrating Eq. (3.2) over the entire electron distribution. The distance along the ionized track from the entry point of the ionizing particle at the cathode is $X = (x + D)/\cos\theta$, where θ is the angle between the track and the chamber normal (see Fig. 3.2). When all electrons have reached the anode, $\varphi_A(\mathbf{r}) = 1$ and $\varphi_A(\mathbf{r_0})$ is given by Eq. (3.7). This leads to the following expression for the anode charge-signal amplitude

$$Q_A = -e \int \rho_0(X)[1 - \sigma \frac{X}{D} \cos\theta] dX = -n_0 e \left(1 - \sigma \frac{\bar{X}}{D} \cos\theta\right), \tag{3.10}$$

where it was used that the total number of electrons in the track is given by $n_0 = \int \rho_0(X) dX$, and that

$$\bar{X} = \frac{1}{n_0} \int X \rho_0(X) dX \tag{3.11}$$

is the center of gravity of the electron distribution along the particle's track. The result above for the anode charge-signal amplitude is the same as obtained considering the influence of the image charge induced on the anode by the positive ions residing in the

interaction region [54, 60]. The cathode and grid charge-signal amplitudes follow in the same way from Eqs. (3.8) and (3.9), respectively,

$$Q_C = n_0 e \left(1 - \frac{\bar{X}}{D}\cos\theta\right), \tag{3.12}$$

$$Q_G = n_0 e \left(1 - \sigma\right) \frac{\bar{X}}{D}\cos\theta. \tag{3.13}$$

The time development of charge signals from electrode k is found by integrating Eq. (3.2) over the moving electron distribution $\rho(x,t)$ created at $t = 0$,

$$Q_k(t) = -e\left[\int \rho(x,t)\varphi_k(x)dx - \int \rho(x,0)\varphi_k(x)dx\right]. \tag{3.14}$$

Combining this with the weighting potentials given in Eqs. (3.7 and 3.8) and assuming that no charge distribution is created in the collection region, the anode charge signal may be written as

$$Q_A(t) = -\sigma Q_C(t) - e(1-\sigma)\int_0^p \rho(x,t)\frac{x}{p}dx. \tag{3.15}$$

Hence, the anode pulse can be decomposed into two parts, the first one caused by electrons drifting in the interaction region and the second one by electrons drifting in the collection region. The time evolution of the anode pulse according to Eq. (3.15) for the electron distribution created by a typical fission fragment in P-10 gas and for three different emission angles is depicted in Fig. 3.4. Each electron makes a contribution to the anode charge signal proportional to its contribution to the cathode charge signal, when moving through the interaction region. When drifting through the collection region, each electron contributes with $-e(1-\sigma)$ to the anode charge signal. Hence, the ideal anode signal $Q_A^*(t)$, which is independent of the electron drift in the ionization region, can be reconstructed from the anode and cathode signals by

$$Q_A^*(t) := \frac{Q_A(t) + \sigma Q_C(t)}{1-\sigma}. \tag{3.16}$$

The factor $(1-\sigma)$ in the denominator makes sure that the final signal amplitude is equal to the collected charge $-n_0 e$. Equation (3.15) shows that before any electrons have passed the grid $Q_A(t) = \sigma Q_C(t)$ holds. This relation was used in Refs. [61, 62] to find the parameter σ experimentally. To validate the numerical calculation of the weighting potentials calculations were performed for the chamber geometry in Refs. [61, 62]. In addition to the two-dimensional parallel wire grid, calculations were also performed in three dimensions for a grid that uses crossed wires. In Fig. 3.5 experimental values of the parameter σ are compared with values calculated in this work using FEM.

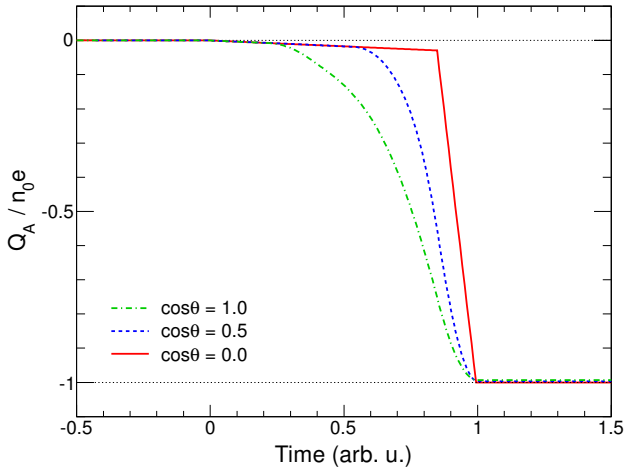

Fig. 3.4: *Calculated time evolution of anode charge signals for three different values of* $\cos\theta$*, according to Eq. (3.15). The calculation is based on the ionization track left in P-10 gas by a* ^{135}I *- ion with a kinetic energy of 73 MeV, as calculated with SRIM [63].*

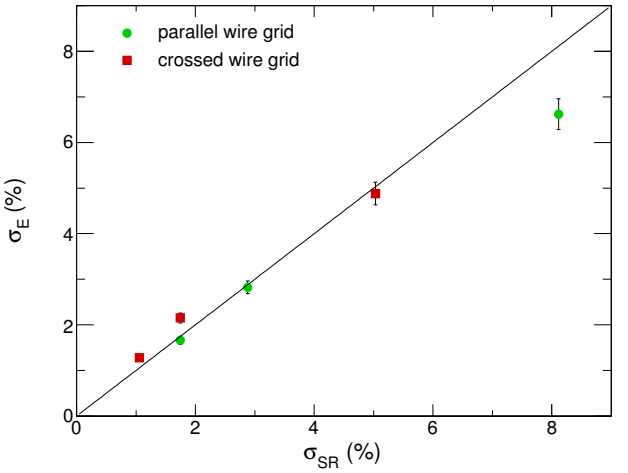

Fig. 3.5: *Plot of experimental* σ_E *[61, 62] versus calculated* σ_{SR} *values of the grid inefficiency parameter for different grid types and anode-grid distances. The green symbols represent a parallel wire grid while the red symbols represent a crossed wire grid. The error bars are experimental, mainly stemming from uncertainties in the relative calibration of the two amplification chains.*

3.3 Data Acquisition

Figure 3.1 displays a schematic view of the electronic setup. The pulse-height data from the two anodes was converted to channel numbers using a CAEN V785 analog-to-digital converter and stored digitally. Stability of the amplification chain was monitored by feeding pulses from a precision pulse generator to the input of the charge sensitive preamplifiers at a rate of 2.5 Hz. Corrections for drifts in the amplification chain were done offline by multiplying the recorded ADC channel number with the ratio of a pre-defined reference value to the pulse height from the pulse generator, averaged over the last 500 registered pulses. For the purpose of determining the emission angle θ (cf. Sect. 4.2), the time difference between anode and cathode signals was also measured. All timing information was digitized using a CAEN V775 time-to-digital converter. The time difference between the cathode and anode timing signals registered by the TDC is ideally equal to the drift time of ionization electrons created furthest away from the cathode. However, due to non-perfect triggering, the time difference may differ slightly from the drift time. In order to avoid distortion of the angular distributions, particular attention was paid to the choice of discriminator for the two signals. The initial part of the cathode signal rises linearly, but has a final pulse-height dependence on the emission angle, therefore the discriminator of choice is of constant-fraction type. The anode-signal pulse-height, on the other hand, has no angular dependence (apart from the small charge induced due to grid inefficiency), but it has a rise times and shapes which strongly depend on the emission angle. To avoid shape-dependent walk, a leading-edge discriminator with a threshold set just above the noise level was chosen. This choice of discriminator does introduce a pulse-height dependent walk, but since the pulse height is registered along with the drift time, this can be corrected for offline.

The data acquisition is based on the MBS (multi-branch system) computer code, developed at the GSI [64]. The data was written event-by-event to disk in a so-called list-mode file for offline analysis. The experiments were monitored and controlled online using an interface between the MBS based data acquisition and the computer program Go4 (GSI Object Oriented On-line Off-line system [65]).

Chapter 4

Data Analysis

4.1 Calculation of Average Excitation Energies

The energy spectrum of bremsstrahlung photons created from the electron beam is continuous. This leads to a continuous distribution of excitation energies of the fissioning nucleus for each energy of the electron beam E_0. The excitation energy spectra can be calculated, if the photon spectra $N_\gamma(E, E_0)$ and the photofission cross section $\sigma_{\gamma,f}(E)$ are known. The average excitation energy of the fissioning nucleus is then given by

$$\langle E_x(E_0)\rangle = \frac{\int_0^{E_0} N_\gamma(E, E_0)\sigma_{\gamma,f}(E)EdE}{\int_0^{E_0} N_\gamma(E, E_0)\sigma_{\gamma,f}(E)dE}. \tag{4.1}$$

To determine the photon spectra Monte-Carlo simulations using the software package Geant4 [66] were carried out. The simulated photon fluxes were fitted with polynomials of the form

$$p(E) = \sum_{i=0}^{4} a_i \cdot E^{(i-1)}, \tag{4.2}$$

which were used to represent $N_\gamma(E, E_0)$ in order to reduce statistical fluctuations, when calculating the excitation energy spectra. Figure 4.1 displays photofission cross sections for ^{238}U, ^{234}U and ^{232}Th from the evaluated nuclear data library ENDF [67] and experimental photofission cross section for ^{234}U from Ref. [68]. In the calculation of the excitation energy spectra for ^{238}U and ^{232}Th, the photofission cross sections from the ENDF library were used. For ^{238}U and ^{232}Th the availability of experimental data on the low-energy photofission cross section is good, for ^{234}U on the other hand the situation is different. For ^{238}U

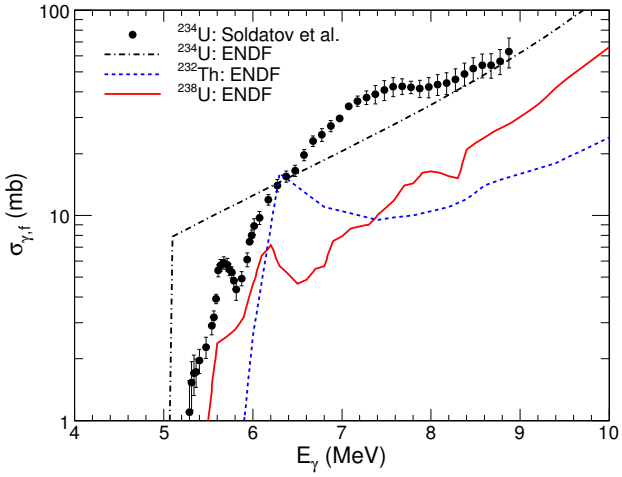

Fig. 4.1: *Evaluated photofission cross sections for ^{238}U (solid red line), ^{234}U (dotted–dashed black line) and ^{232}Th (dashed blue line) from Ref [67] and experimental photofission cross section for ^{234}U (full circles) from Ref. [68].*

and ^{232}Th the evaluated data reproduce structures corroborated by experimental data. For ^{234}U the evaluated data in the energy region below 10 MeV consists of an exponential tail fitted to the giant dipole resonance with a fission threshold at 5.06 MeV. The experimental data that do exist reveal more structures, hence, for a better representation experimental cross section data from Ref. [68] was used in the calculation of the excitation spectra for this nucleus. On the left hand side of Fig. 4.2 the simulated spectra are displayed along with the fitted polynomials. The calculated excitation spectra are displayed on the right hand side of Fig. 4.2.

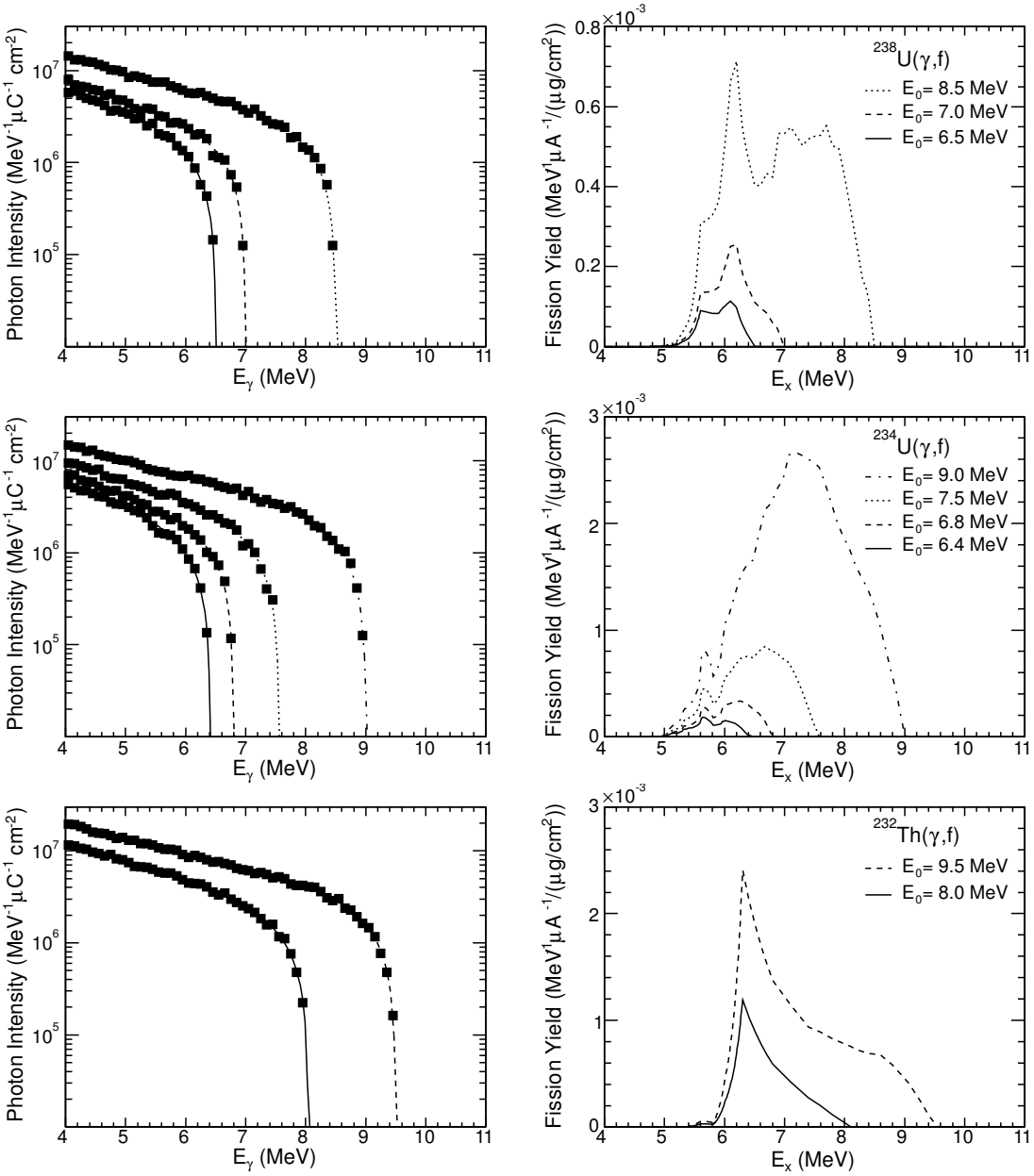

Fig. 4.2: *Bremsstrahlung spectra with endpoint energies of 8.5, 7.0, 6.5 MeV (top left) and 9.0, 7.5, 6.8, 6.4 MeV (middle left) and 9.5, 8.0 MeV (bottom left). The solid, dashed, dotted and dotted–dashed lines represent fits of Eq. (4.2) to the simulated data, represented by the black squares. Also shown are corresponding calculated fission yields per μA electron beam current incident on the radiator and per μg/cm^2 fission target mass thickness for $^{238}U(\gamma, f)$ (top right), $^{234}U(\gamma, f)$ (middle right) and $^{232}Th(\gamma, f)$ (bottom right).*

4.2 Determination of Angular Distributions

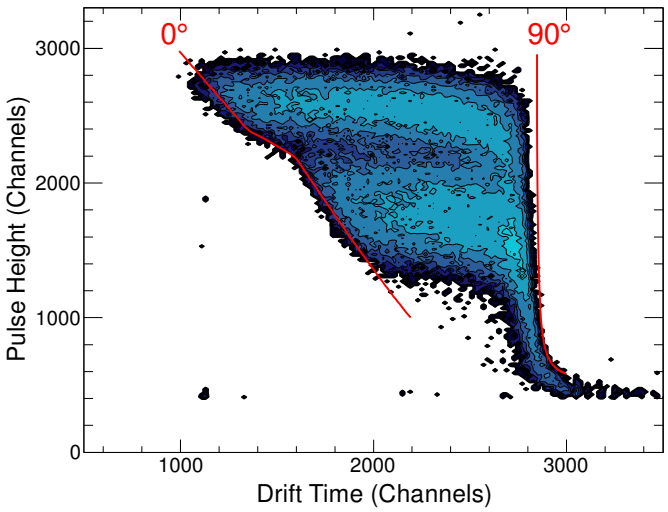

Fig. 4.3: *Registered time difference between anode and cathode timing signals versus the anode pulse height. The solid lines marked* $0°$ *and* $90°$ *indicates the limits of the distribution used to determine the emission angle.*

The emission angle θ of a fission fragment relative to the target normal is extracted from the drift time of ionization electrons, created along the fragment's stopping track. The time it takes for electrons created furthest away from the cathode to reach the grid electrode is given by

$$T^* = \frac{D - R\cos\theta}{v}, \tag{4.3}$$

where R is the range of the fragment in the counting gas and v is the electron drift velocity. The cathode-grid distance is denoted by D, according to Fig. 3.2. Figure 4.3 shows a contour plot with the registered time difference between anode and cathode signals on the abscissa and the anode pulse height on the ordinate. Events at low pulse height around TDC channel number 2800 result from fragments that have suffered extensive energy loss in the target material. This occurs when fragments are emitted almost parallel to the target plane. As may be observed, this energy-loss tail varies with the inverse of the pulse height. This is due to the pulse-height dependent walk in the leading edge triggering of the anode signal. A function $f(P_A) \propto 1/P_A$ fitted to the energy loss tail represents the drift time for events with $\cos\theta = 0$, and allows the definition

$$\Delta T = f(P_A) - T = \frac{R}{v}\cos\theta. \tag{4.4}$$

Once the anode pulse height is corrected for the grid inefficiency (Sect. 4.3.1), the range of the fission fragments is determined as a function of the anode pulse height. The solid red lines labeled 0° and 90° in Fig. 4.3 represent the determined fission-fragment range and the function $f(P_A)$, respectively.

The $\cos\theta$-values are determined from each chamber side individually. Due to conservation of linear momentum the two fragments from each event are collinear. Hence, to reduce the uncertainty in the orientation of the fission axis, an average value of the determined $\cos\theta$-values from the two chamber sides is used.

4.2.1 Angular Resolution

The fact that the $\cos\theta$-values from the two fission fragments are supposed to be equal can be utilized to determine the resolution of the emission angle. The left hand side of Fig. 4.4 shows the distribution of the difference in the $\cos\theta$-values determined from the two chamber sides obtained in the measurement of $^{238}\mathrm{U}(\gamma, f)$. The width of this distribution is related to the angular resolution. Assuming that the uncertainties in the $\cos\theta$-values from the two chamber sides are equal, the resolution in the average value is given by half of the FWHM of the depicted distribution. The right-hand side of Fig. 4.4 shows a comparison of the angular resolutions obtained in this work with resolution values obtained in Refs. [69–71]; the latter ones all employ a different technique for extracting $\cos\theta$. That technique is based on the angular dependence of the induced charge on the grid electrode [60], see Eq. (3.13). The grid signal is, however, bipolar and therefore not suited for shaping and amplification in a spectroscopic amplifier. Therefore, the grid and the anode signals are added up using splitters and fast filter amplifiers to create a unipolar signal whose height is proportional to $\cos\theta$. When comparing the obtained angular resolutions the thickness of the target needs to be taken into account, since angular straggling and decreased energy resolution will affect the angular resolution. A lower limit of the angular resolution that can be obtained with the drift-time method is set by the angular straggling of the fragments in the counting gas, from an SRIM [63] simulation this limit was found to be around 6–7 % for typical fission fragments in P-10 gas. The expected trend of increased resolution with decreasing target thickness is confirmed by the data in Fig. 4.4. Moreover, it may be observed that the angular resolutions obtained using either of both methods are evidently in good agreement with each other. Therefore, it is concluded that the drift-time method presented here is comparable in accuracy with the method of Ref. [60], but with a much simplified procedure for setting up the experiment. Further details have been published in Ref. [15].

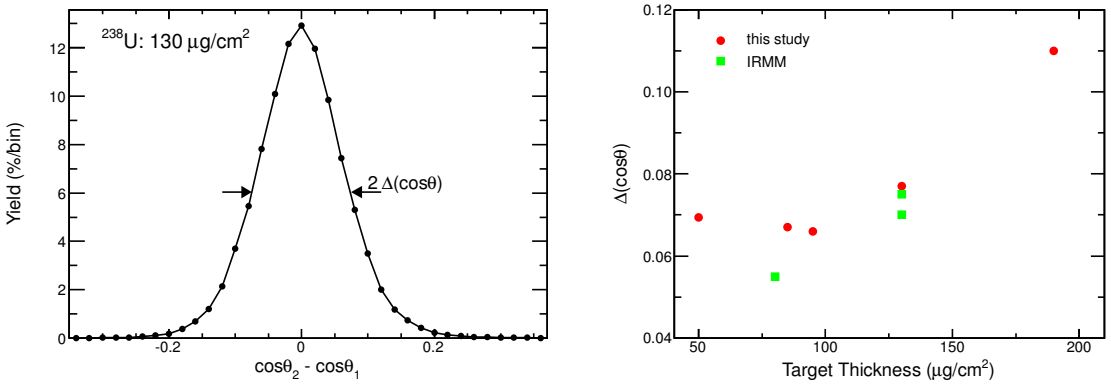

Fig. 4.4: *Left: Distribution of the difference in* $\cos\theta$*-values determined from the two chamber sides for a* ^{238}U *target with a thickness of 130* $\mu g/cm^2$*. Right: Angular resolution as a function of target thickness obtained with the drift time method for the various targets used in this work (red circles) and those from Refs. [69–71] (green circles) using the summing method for determining the emission angle.*

4.3 Calculation of Mass and Total Kinetic Energy

Conservation of linear momentum, with the approximation that the sum of the fission fragments' masses is equal to the mass of the fissioning nucleus, leads to the following relations

$$A_1 = A_f \frac{E_2}{\mathrm{TKE}}, \qquad A_2 = A_f \frac{E_1}{\mathrm{TKE}}, \tag{4.5}$$

for the fission fragments entering chamber side (1) and (2), respectively. The masses have been replaced by their respective mass numbers $A_{1,2}$, the fragments' kinetic energies gained from the fission process are denoted $E_{1,2}$, and $\mathrm{TKE} = E_1 + E_2$ is the total kinetic energy. The mass number of the fissioning nucleus is denoted by A_f. Highly excited fission fragments evaporate neutrons as part of their de-excitation processes. Hence, as a consequence of the recoil from neutron emission, the kinetic energies of the fragments, as they enter the counting gas differ from the kinetic energies they gained in the fission process. Since the kinetic energies that enter into Eq. (4.5) are the initial energies, a correction for the neutron evaporation must be applied to the registered energies. The initial energies and masses of the fission fragments are referred to as pre-neutron quantities, in contrast to the post-neutron quantities of the fragments as they enter the counting gas. The kinematics for the emission of a single neutron from a fragment is illustrated in Fig. 4.5. The conservation of momentum can be written as

$$\vec{p}_f{}^{\,2} = \vec{p}_i{}^{\,2} - 2|\vec{p}_i||\vec{p}_n|\cos\theta_n + \vec{p}_f{}^{\,2},$$

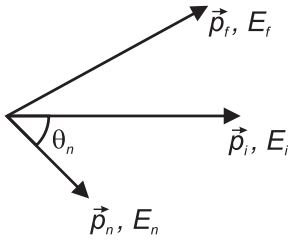

Fig. 4.5: *Illustration of the kinematics involved in the emission of a single neutron with momentum $\vec{p}_n$ and energy E_n from a fission fragment with initial momentum $\vec{p}_i$ and energy E_i and final momentum $\vec{p}_f$ and energy E_f.*

where the quantities are defined in Fig. 4.5. The relation can be rewritten for the respective energies

$$E_f = E_i \frac{m_i}{m_f} - \frac{|\vec{p}_i||\vec{p}_n|}{m_f} \cos\theta_n + E_n \frac{m_n}{m_f}.$$

To obtain the relation for the emission of a number of ν neutrons, it is assumed that the emission is isotropic. This leads to $\cos\theta_n = 0$ on average, eliminating the second term. The third term may be neglected considering that the energy of emitted neutrons is about 1 MeV and that the ratio m_n/m_f is of the order of 10^{-2}, to be compared with 50 – 100 MeV for the fragment energies. Again, replacing the masses with the mass numbers and using conservation of mass leads to

$$E_{post} = \frac{A}{A-\nu} E_{pre}, \tag{4.6}$$

where the indices f, i for final and initial have been replaced by $post, pre$ for post- and pre-neutron emission, respectively. Obviously, this relation can only be used to correct the energies, if both the initial mass number A and the number of emitted neutrons ν are known. The number of neutrons can be found using literature data on the average number of neutrons emitted as a function of the fragment mass number $\bar{\nu}(A)$ together with the relation [72]

$$\nu(A, \mathrm{TKE}) = \bar{\nu}(A) + \frac{\bar{\nu}(A)}{\bar{\nu}(A) + \bar{\nu}(A_f - A)} \cdot \frac{\langle \mathrm{TKE}(A) \rangle - \mathrm{TKE}}{8.6\ \mathrm{MeV}}, \tag{4.7}$$

where 8.6 MeV is the average neutron separation energy of the fission fragments [73]. The data for $\bar{\nu}(A)$ were taken from Refs. [16,74,75]. The mass number A is found iteratively from Eqs. (4.5) – (4.7). The first approximation of the mass numbers is known as the provisional masses $\mu_{1,2}$; they are found from Eq. (4.5) using the measured post-neutron energies. The provisional masses are then used in Eqs. (4.6) and (4.7) to find a first approximation of the pre-neutron energies, which are then used in Eq. (4.5) to find a second order approximation of the mass numbers. The iterative procedure is stopped, when the difference in the mass

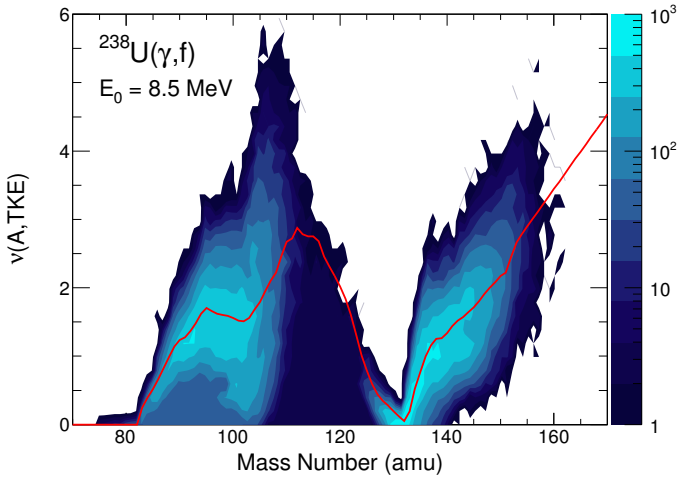

Fig. 4.6: *The number of emitted neutrons $\nu(A, \mathrm{TKE})$ calculated according to Eq. (4.7) as a function of the pre-neutron fission-fragment mass number, for the reaction $^{238}U(\gamma, f)$ at $E_0 = 8.5$ MeV. The solid red line represent the average number of neutrons $\bar{\nu}(A)$ from Ref. [16]. A logarithmic color-scale indicates the number of counts per bin.*

number from one iterative step to the next is smaller than 1/8 atomic mass units (amu). The second term of Eq. (4.7), which approximates the dependence of the number of emitted neutrons on fragment excitation-energy, requires that the average TKE as a function of the mass number $\langle \mathrm{TKE}(A) \rangle$ is known. This distribution was determined by neglecting the second term of Eq. (4.7) in the iterative calculation in a first approximation of the mass and TKE distribution. An example of the number of emitted neutrons calculated from Eq. (4.7) in this way is given in Fig. 4.6 as a function of the pre-neutron mass number for the reaction $^{238}\mathrm{U}(\gamma, f)$ at $E_0 = 8.5$ MeV. The $\bar{\nu}(A)$ curve is scaled to reproduce the average total number of neutrons $\bar{\nu}_T$ obtained in Refs. [16, 74, 75], by assuming a linear relation between $\bar{\nu}_T$ and the average excitation energy

$$\bar{\nu}_T = a + b \cdot \langle E_x \rangle. \tag{4.8}$$

Before the iterative process to calculate the masses from the registered pulse heights can be started a number of corrections need to be applied. The different corrections are described separately below.

4.3.1 Correction for Grid Inefficiency

The grid inefficiency has already been extensively discussed in Sect. 3.2.1. Using the drift time method for determining the emission angle no information on the center of gravity of

the charge distribution $\bar{X}$ is not directly available. From a SRIM [63] simulation the ratio $\bar{X}/R$, where R is the range of the fission fragments in the counting gas, was found to be constant at 0.34 with a standard deviation of 0.02. The registered anode pulse heights are corrected for the angular dependence in Eq. (3.10) using

$$P_A^* = P_A(1 + \sigma\frac{\bar{X}}{R}\frac{v}{D}\Delta T). \tag{4.9}$$

The electron drift velocity v was taken from Ref. [61].

4.3.2 Energy-Loss Correction

As the fragments pass through the target and backing material, they lose kinetic energy that stays undetected. Assuming that the energy loss is given by the path length that the fragment travels in the target, independent of its charge, mass and velocity, the energy loss can be found from the experimental data. By plotting the average anode pulse height against $1/\cos\theta$, which is proportional to the path length, the average energy loss is found. The procedure is illustrated in Fig. 4.7. Two sets of data are shown: one for the fragments that only have to pass the target material (sample side) and another for fragments that in addition have to pass the backing material (backing side). This data was obtained with a ^{238}U sample at $E_0 = 8.5$ MeV. The solid lines show linear fits to the region marked with full symbols. Extrapolation to $1/\cos\theta = 0$ gives the average anode pulse height for zero path length. The fit is first performed for the backing side, the intercept at $1/\cos\theta = 0$ is then kept fixed when performing the fit to the sample side. The slope k of the fitted function is then used to correct the pulse height data according to

$$P_A^{**} = P_A^* + \frac{k}{\cos\theta}. \tag{4.10}$$

Due to multiple scattering in the target material at large emission angles and the fact that the fission does not, as assumed, take place in the center of the target, the energy loss correction fails for large emission angles. Therefore a cut-off angle is introduced in the analysis. The angle, where the energy-loss correction fails, depends on the thickness of the target. The cut-off angle was therefore chosen for each target individually, based on the assumption that the energy distribution should be the same for any angle θ. In Fig. 4.8 the energy-loss corrected pulse-height distribution as a function $\cos\theta$ is plotted for the case of ^{238}U at $E_0 = 8.5$ MeV. The cut-off angle is illustrated by a red dashed line. Clearly, the pulse-height distributions become increasingly distorted for emission angles larger than the cut-off angle.

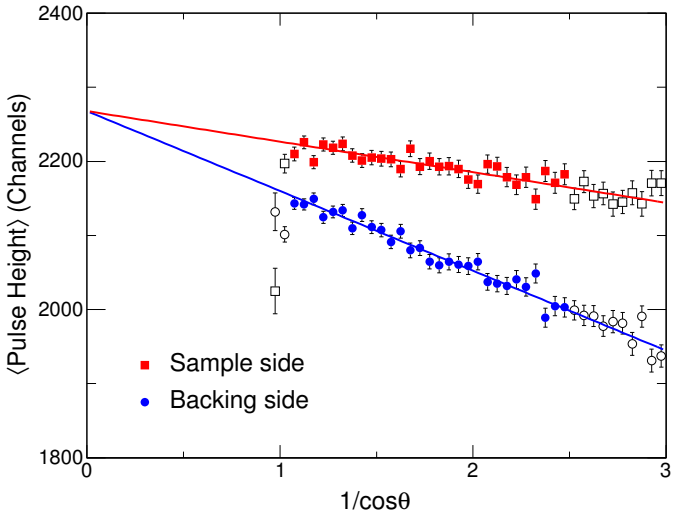

Fig. 4.7: *Average anode pulse height as a function of* $1/\cos\theta$ *for fragments that pass only the target material (red) and for fragments that in addition have to pass the backing material (blue). The solid lines are linear fits to the region of events used in the analysis to calculate the mass distributions, indicated by full colored symbols.*

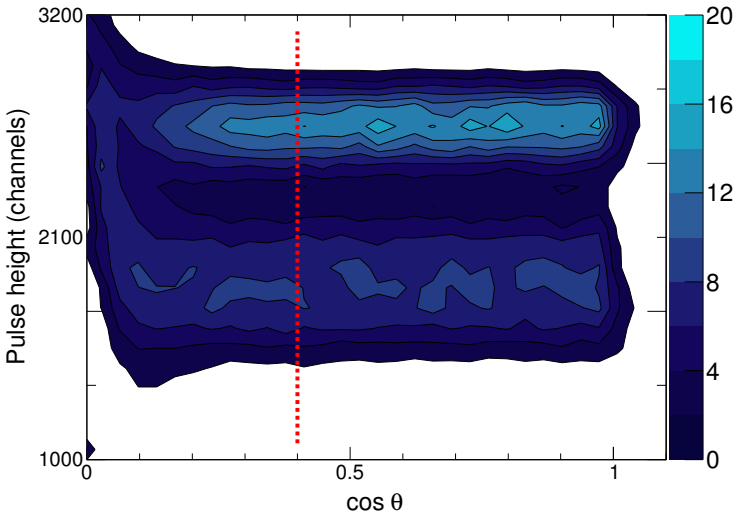

Fig. 4.8: *Anode pulse height corrected for the energy loss in the target material as a function of* $\cos\theta$ *for* ^{238}U *at* $E_0 = 8.5$ *MeV. The pulse-height distribution is normalized to 100 % for each bin in* $\cos\theta$*. The red dotted line indicates the cut-off angle introduced in the analysis.*

4.3.3 Pulse-Height Defect

Multiple ionization [76] and non-ionizing collisions [77] show a dependence on the fragment type. This causes a deviation from the proportionality between the energy of — and the number of electron-ion pairs created by — the fragment, depending on the type of fragment. The deviation from proportionality is usually summarized in a quantity known as the pulse-height defect (PHD). The energy of a fission fragment can be written

$$E_{post} = E_{app} + PHD(A, Z, E), \tag{4.11}$$

where E_{app} is the apparent energy in terms of an energy calibration from alpha-particles. The PHD is a function of mass, charge and energy of the fragment, but can be described as a function of a single variable when expressed in dimensionless LSS (Lindhard-Scharff-Schiott) units [78, 79]. An energy is converted to LSS units according to

$$\epsilon[\text{LSS}] = \frac{0.8553 a_0}{e^2} \frac{(Z_1^{2/3} + Z_2^{2/3})^{-1/2}}{Z_1 Z_2} \frac{A_2}{A_1 + A_2} \cdot E[\text{MeV}], \tag{4.12}$$

where the indices 1, 2 refer to projectile and target, respectively, and a_0 is the Bohr radius. For a gas mixture, such as P-10, empirical rules [60] are used to find A_2 and Z_2

$$A_2 = 0.9 \cdot A_{Ar} + 0.1 \cdot \frac{A_C + A_H}{5} = 36.4,$$
$$Z_2 = 0.9 \cdot Z_{Ar} + 0.1 \cdot \frac{Z_C + Z_H}{5} = 16.4.$$

The PHD in P-10 gas has been determined for a number of different ions at the tandem accelerator of the Physics Institute at the University of Aarhus [60]. The result is reproduced in Fig. 4.9. The PHD found for P-10 gas is much smaller than that found for Semiconductor detectors, but not negligible. A correction for the PHD is included in the iterative procedure for calculating the masses. The apparent energy is first converted to LSS units using Eq. (4.12), A_1 is taken as the current value of the post-neutron mass in the iteration, and Z_1 is taken as the most probable charge according to the conservation of charge-to-mass ratio of the fissioning nucleus. A polynomial fit, shown by the solid red line in Fig. 4.9, is then used to find the corresponding PHD and derive a post-neutron energy, according to Eq. (4.11), which is then used in Eq. (4.6) in the next step of the iteration to find E_{pre}.

A common practice in fission-fragment energy measurements using Frisch grid ionization chambers is to calibrate the pulse-height-to-energy conversion to a known system [80], in order to avoid systematic uncertainties due to extrapolation of alpha-particle energies and uncertainties in the PHD. In this work this procedure was adopted by calibrating the apparent energy, after applying the PHD correction, in a way that the post-neutron TKE

obtained in Ref. [17] was reproduced for ^{238}U at $E_0 = 8.5$ MeV. Hence, all measurements are energy calibrated relative to ^{238}U at $E_0 = 8.5$ MeV. As can be seen in Fig. 4.10 the pre-neutron TKE resulting for the other fissioning systems agree well with systematics derived by Unik et al. [81] and Viola et al. [82].

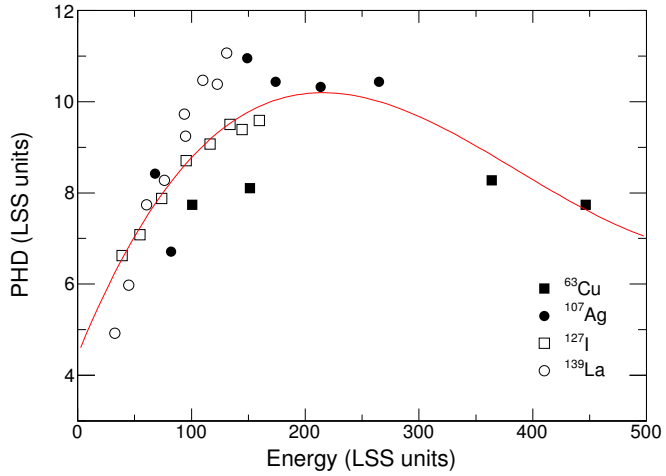

Fig. 4.9: *Experimental PHD for different ions in P-10 gas from Ref. [60]. The solid red line shows a polynomial fit to the experimental data, which is used to represent the PHD in the data analysis.*

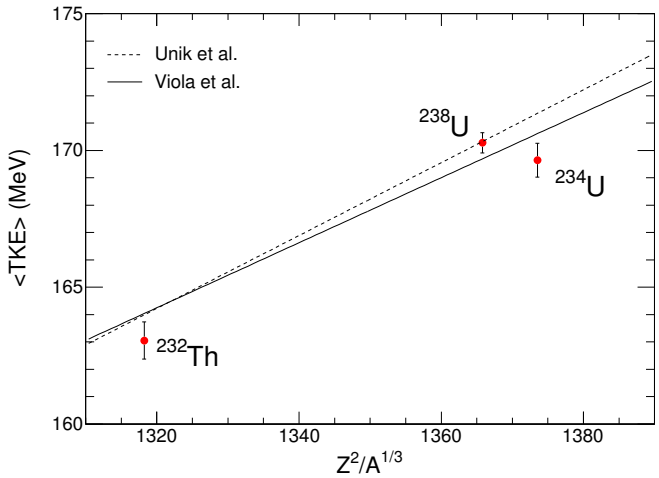

Fig. 4.10: *Mean pre-neutron* TKE *for* ^{238}U, ^{234}U *and* ^{232}Th *as a function of* $Z^2/A^{1/3}$. *The entries have been averaged over the* TKE *determined for the different incident photon spectra and the error bars indicate the spread in these values. The dashed and full lines are prediction of Unik et al [81] and Viola et al [82], respectively.*

Chapter 5

Experimental Results

In this chapter the experimental results are presented. Unless stated otherwise uncertainties are statistical only. In Ref. [83], which used the same calibration procedure as in this work, systematic uncertainties in mean energies and masses were determined to be 0.1 MeV and 0.1 amu, respectively. The results obtained for ^{234}U(γ, f) with the two different targets show quite strong deviations from one another. The results obtained with the two different targets are therefore presented separately here. An explanation for the discrepancies will be discussed in Sect. 5.2. In the case of the measurements on ^{238}U(γ, f) with the 130.3 μg/cm^2 and the 82.9 μg/cm^2 targets at $E_0 = 8.5$ MeV the data showed deviation only within the experimental uncertainties.

5.1 Mass and TKE Distributions

Pre-neutron fission fragment mass distributions for ^{238}U, ^{234}U and ^{232}Th are displayed in Figs. 5.1 - 5.4. The mass yield is normalized to 200 %. The distributions have been labeled with the calculated average excitation energies and consecutively displaced by 2 %. Obviously, the distributions are perfectly symmetric around mass number $A = A_f/2$, this is inherent to the method used to determine the distribution. The preference for asymmetric mass split, characteristic for low-energy fission of actinide nuclei, are easily recognized in all the mass distributions. In Tabs. 5.1 - 5.4 characteristic parameters of the mass distributions are given. In the photofission of ^{238}U a trend of the mean heavy-fragment mass to move towards symmetry, when lowering the excitation energy is apparent. This can be explained by a decrease in the heavy-fragment mass yield in the region above heavy-fragment mass $A_H \sim 140$, with a simultaneous increase for lighter masses at lower excitation energy. For ^{234}U the mass yield in the region above $A_H \sim 140$ increases going from $\langle E_x \rangle = 7.23$ MeV to $\langle E_x \rangle = 6.49$ MeV, while the mean heavy-fragment mass stays

Tab. 5.1: *Characteristic parameters of the measured total kinetic energy and mass distributions from photofission of ^{238}U obtained with a 130.3 $\mu g/cm^2$ target. The calculated average excitation energy of the fissioning nucleus is denoted by $\langle E_x \rangle$ and σ_{E_x} stands for the standard deviation of the excitation energy. The mean heavy-fragment mass and the standard deviation of the mass peak are denoted by $\langle A_H \rangle$ and σ_A, respectively. Results from Ref. [17] are included for comparison.*

E_0 (MeV)	$\langle E_x \rangle$ (MeV)	σ_{E_x} (MeV)	$\langle$TKE$\rangle$ (MeV)	σ_{TKE} (MeV)	$\langle A_H \rangle$ (amu)	σ_A (amu)	Ref.
8.5	6.91	0.60	170.50 ± 0.06	10.73 ± 0.04	139.76 ± 0.03	6.00 ± 0.02	this work
8.35	6.68		170.41 ± 0.30	11.02 ± 0.10	139.49 ± 0.05	6.09 ± 0.05	[17]
7.33	6.23		170.12 ± 0.30	11.13 ± 0.10	139.37 ± 0.05	5.99 ± 0.05	[17]
7.0	6.11	0.14	170.20 ± 0.09	11.02 ± 0.06	139.51 ± 0.05	6.16 ± 0.04	this work
6.5	5.90	0.08	170.13 ± 0.07	11.04 ± 0.05	139.31 ± 0.04	6.09 ± 0.03	this work
6.44	5.84		170.05 ± 0.50	11.04 ± 0.10	139.28 ± 0.05	6.06 ± 0.05	[17]

constant within the statistical uncertainty. Further lowering of the excitation energy causes a decrease in mass yield above $A_H \sim 140$, which causes a slight decrease in the mean heavy-fragment mass. For ^{232}Th an increase in the mass region above $A_H \sim 140$ is observed, going from $\langle E_x \rangle = 7.26$ MeV to $\langle E_x \rangle = 6.68$ MeV. The average TKE and width of the TKE distribution as a function of heavy-fragment mass number is displayed in Figs. 5.5 - 5.8. For comparison, the results obtained for the highest bremsstrahlung endpoint energy for each fissioning nucleus is drawn as a dotted line in the figures representing the results at lower endpoint energies. The average TKE distributions show some common features for all fissioning nuclei, namely a characteristic dip around the symmetric mass split and a well pronounced maximum around mass number $A_H \approx 130$. These features are common to low-energy fission of all light actinides. In the case of ^{238}U no strong changes in the average TKE distributions are observed with changing excitation energy. However, an increase in the width of the TKE distribution is seen over the entire mass range at an average excitation energy of 6.11 MeV. In the case of ^{234}U a rather strong increase in the TKE is seen in the mass region $A_H \sim 120 - 128$, going from an average excitation energy of 7.26 MeV to 6.68 MeV, in Fig. 5.7. This coincides with a relative decrease in yield for symmetric mass splits.

Comparing the results obtained with the two different targets used for the measurements on $^{234}\mathrm{U}(\gamma, f)$, some discrepancies may be observed. The widths of mass and TKE distributions are consistently larger for the thicker of the two targets. Furthermore a less pronounced minimum of $\langle$TKE$\rangle$ for symmetric mass splits and a decrease in the slope of $\langle$TKE$\rangle$ as function of fragment mass for asymmetric mass splits are observed. These observations may be explained by mass and energy resolution broadening due to the energy loss in the target layer.

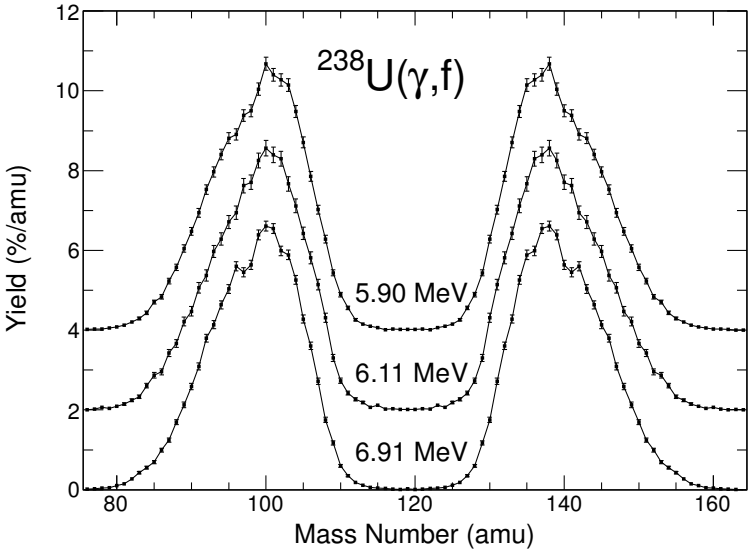

Fig. 5.1: *Yield as a function of fission-fragment mass number from the reaction $^{238}U(\gamma, f)$ obtained with a 130.3 $\mu g/cm^2$ target. The curves are consecutively displaced by 2% and labeled with the average excitation energy.*

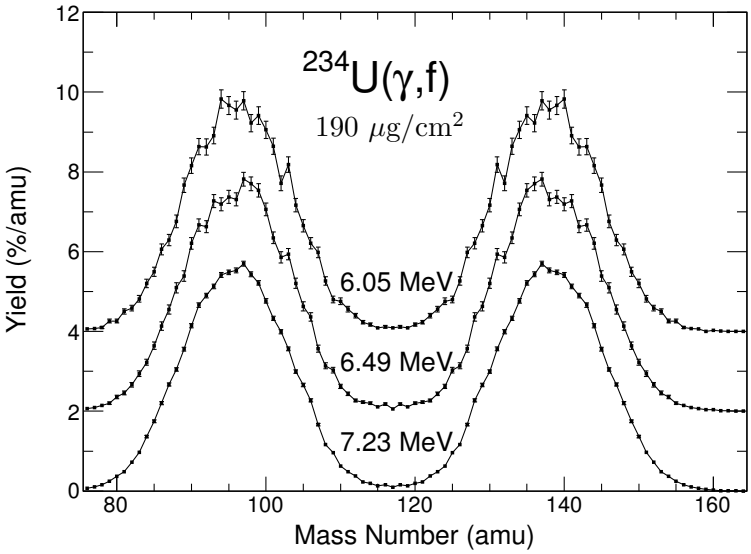

Fig. 5.2: *Yield as a function of fission-fragment mass number from $^{234}U(\gamma, f)$ obtained with a 190.0 $\mu g/cm^2$ target. The curves are consecutively displaced by 2% and labeled with the average excitation energy.*

Tab. 5.2: *Characteristic parameters of the measured total kinetic energy and mass distributions from photofission of ^{234}U obtained with the 190.0 $\mu g/cm^2$ target. The calculated average excitation energy of the fissioning nucleus is denoted by $\langle E_x \rangle$, and σ_{E_x} stands for the standard deviation of the excitation energy. The mean heavy-fragment mass and the standard deviation of the mass peak are denoted by $\langle A_H \rangle$ and σ_A, respectively.*

E_0 (MeV)	$\langle E_x \rangle$ (MeV)	σ_{E_x} (MeV)	$\langle \mathrm{TKE} \rangle$ (MeV)	σ_{TKE} (MeV)	$\langle A_H \rangle$ (amu)	σ_A (amu)
6.8	6.05	0.15	170.9 ± 0.20	12.1 ± 0.10	137.73 ± 0.10	6.27 ± 0.07
7.5	6.49	0.29	171.5 ± 0.10	11.5 ± 0.10	138.06 ± 0.08	6.33 ± 0.05
9.0	7.23	0.66	170.8 ± 0.04	11.68 ± 0.03	137.96 ± 0.02	6.50 ± 0.02

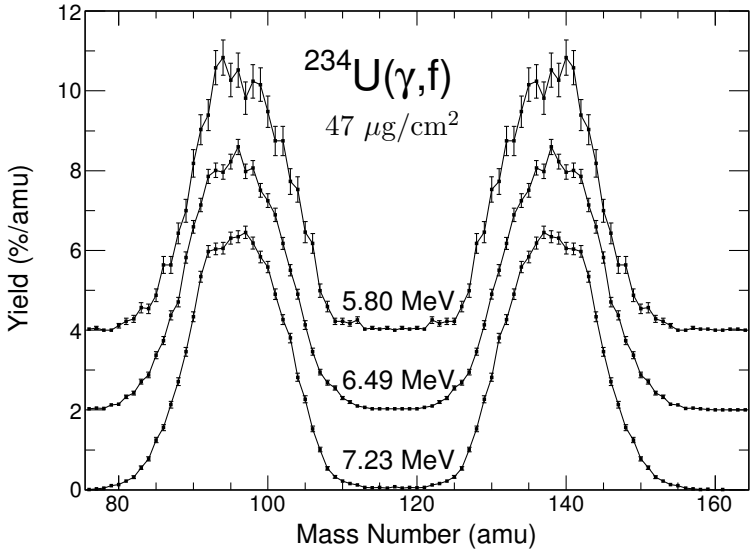

Fig. 5.3: *Yield as a function of fission-fragment mass number from the reaction $^{234}U(\gamma, f)$ obtained with a 46.6 $\mu g/cm^2$ target. The curves are consecutively displaced by 2% and labeled with the average excitation energy.*

Tab. 5.3: *Characteristic parameters of the measured total kinetic energy and mass distributions from photofission of ^{234}U obtained with the 46.6 $\mu g/cm^2$ target. The calculated average excitation energy of the fissioning nucleus is denoted by $\langle E_x \rangle$ and σ_{E_x} stands for the standard deviation of the excitation energy. The mean heavy-fragment mass and the standard deviation of the mass peak are denoted by $\langle A_H \rangle$ and σ_A, respectively.*

E_0 (MeV)	$\langle E_x \rangle$ (MeV)	σ_{E_x} (MeV)	$\langle \mathrm{TKE} \rangle$ (MeV)	σ_{TKE} (MeV)	$\langle A_H \rangle$ (amu)	σ_A (amu)
6.4	5.80	0.09	169.88±0.12	10.44±0.09	137.77±0.05	5.77±0.04
7.5	6.49	0.29	170.00±0.08	10.59±0.06	138.29±0.05	5.92±0.03
9.0	7.23	0.66	169.79±0.05	10.11±0.03	138.10±0.04	5.79±0.03

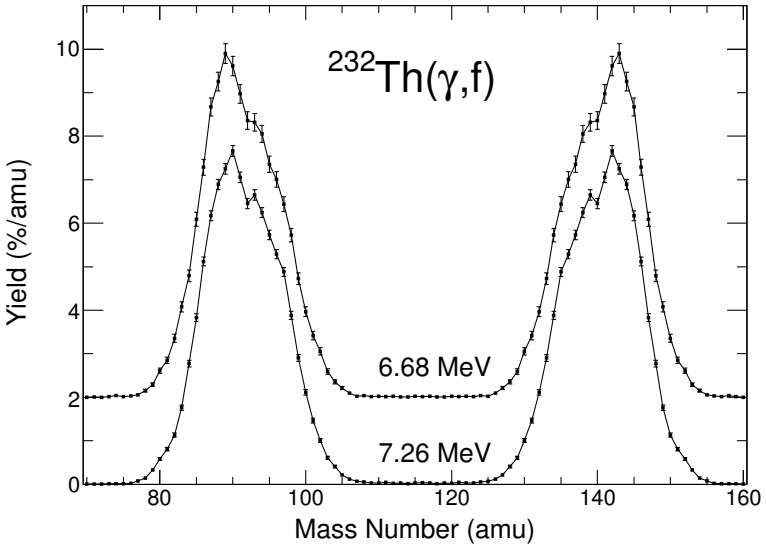

Fig. 5.4: *Yield as a function of fission-fragment mass number from the reaction $^{232}Th(\gamma, f)$ obtained with a 87.0 $\mu g/cm^2$ target. The curves are consecutively displaced by 2% and labeled with the average excitation energy.*

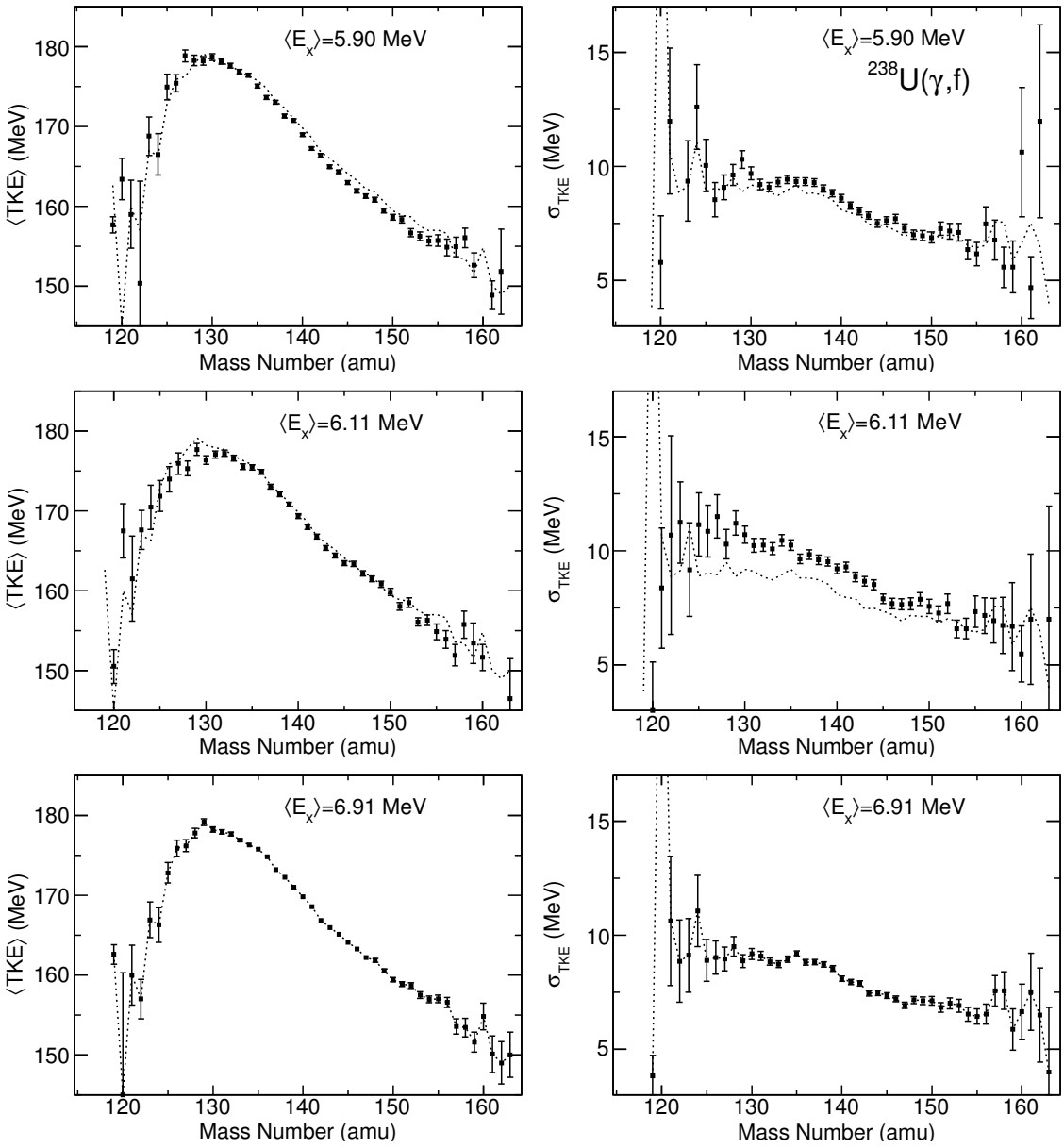

Fig. 5.5: *Average fragment* TKE *(left) and width (right) as a function of the fragment mass number for photofission of* ^{238}U *with 6.5, 7.0, and 8.5 MeV bremsstrahlung from top to bottom, obtained with a 130.3* $\mu g/cm^2$ *target. The dotted line repeats the result obtained at 8.5 MeV bremsstrahlung. The error bars refer to statistical uncertainties only.*

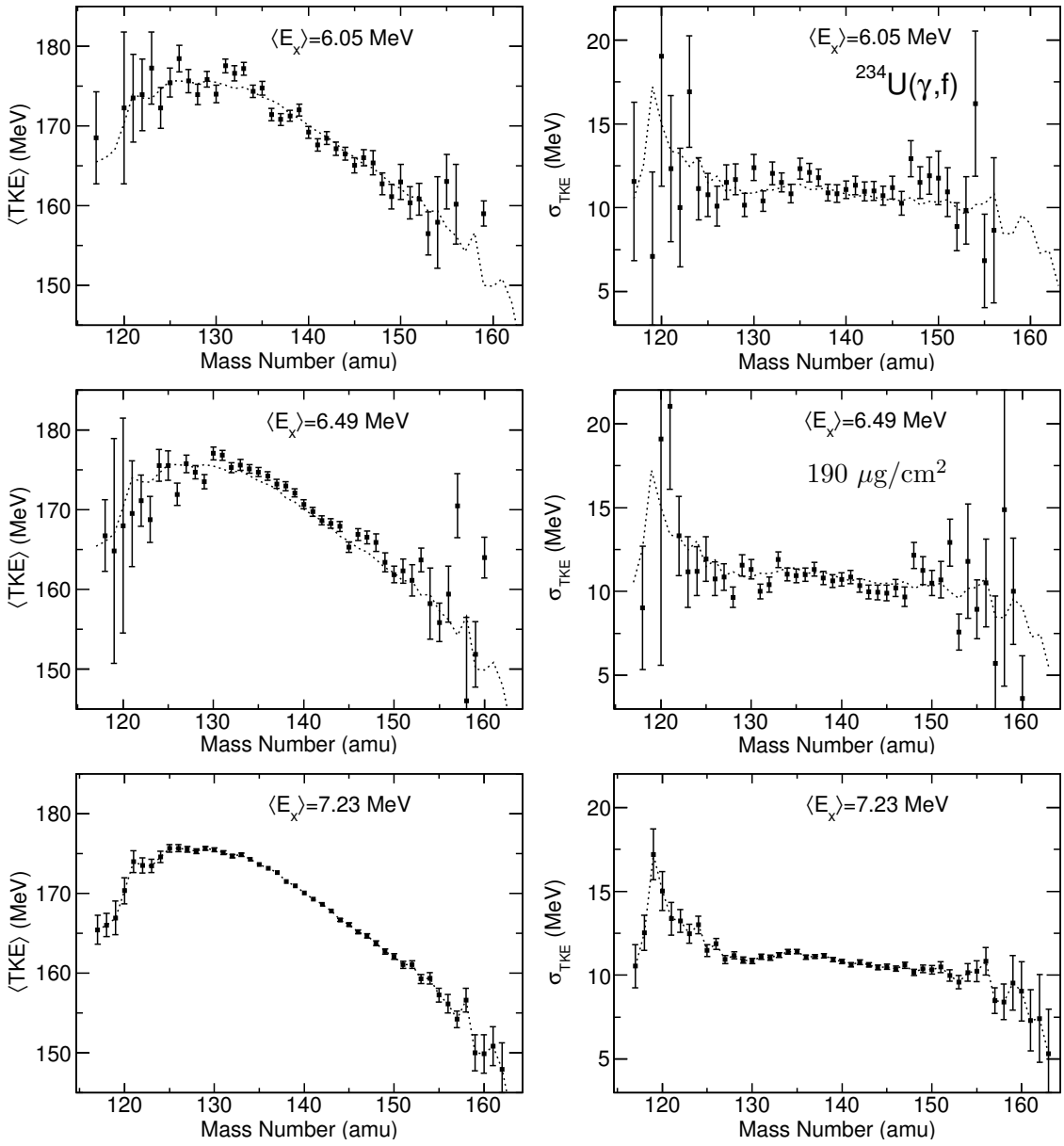

Fig. 5.6: *Average fragment* TKE *(left) and width (right) as a function of the fragment mass number for photofission of* ^{234}U *with 6.8, 7.5, and 9.0 MeV bremsstrahlung from top to bottom, obtained with a 190.0* $\mu g/cm^2$ *target. The dotted line repeats the result obtained at 9.0 MeV bremsstrahlung. The error bars refer to statistical uncertainties only.*

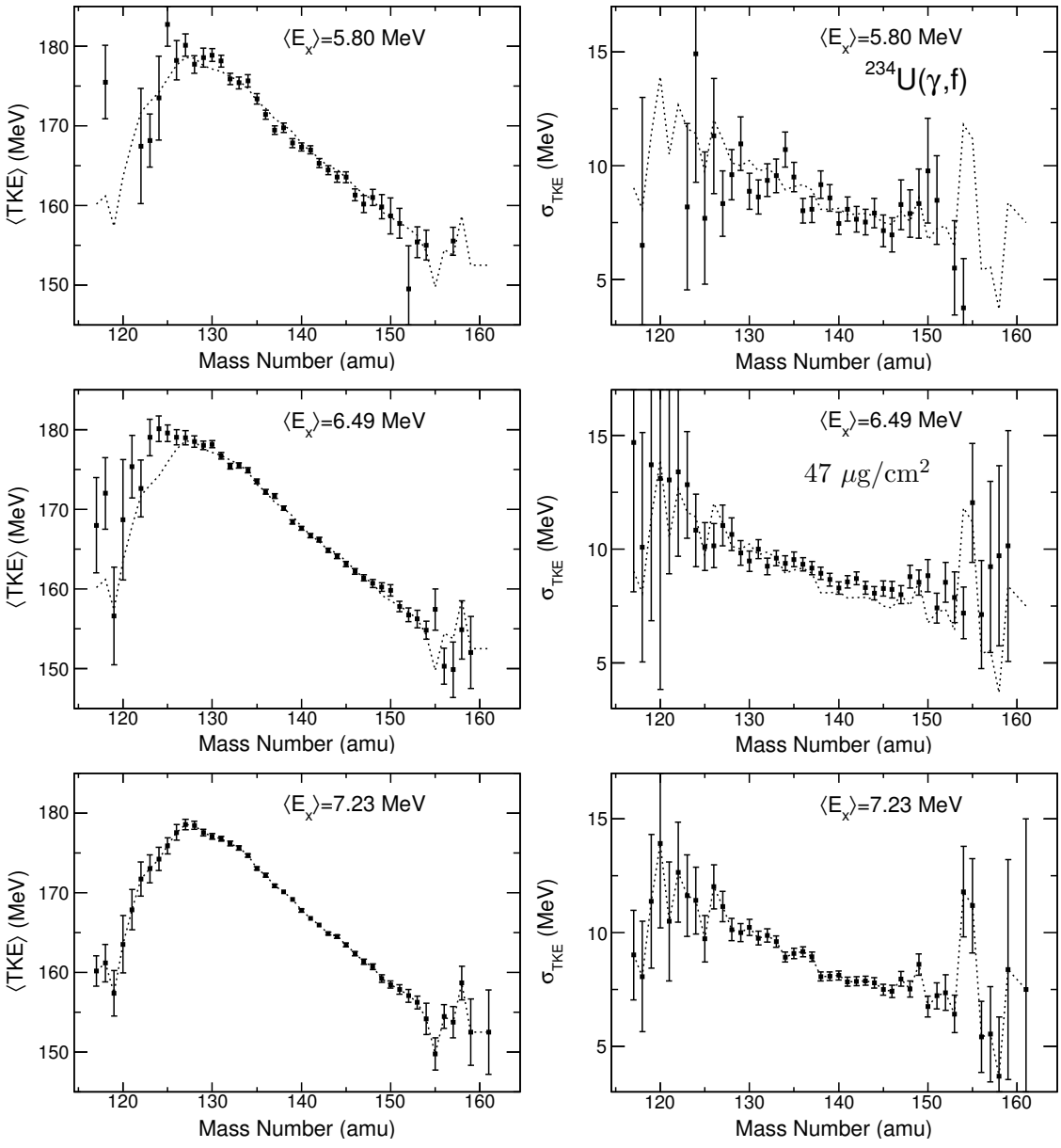

Fig. 5.7: *Average fragment* TKE *(left) and width (right) as a function of the fragment mass number for photofission of* ^{234}U *with 6.4, 7.5, and 9.0 MeV bremsstrahlung from top to bottom, obtained with a 46.6* $\mu g/cm^2$ *target. The dotted line repeats the result obtained at 9.0 MeV bremsstrahlung. The error bars refer to statistical uncertainties only.*

Tab. 5.4: *Characteristic parameters of the measured total kinetic energy and mass distributions from photofission of ^{232}Th. The calculated average excitation energy of the fissioning nucleus is denoted by $\langle E_x \rangle$ and σ_{E_x} stands for the standard deviation of the excitation energy. The mean heavy-fragment mass and the standard deviation of the mass peak are denoted by $\langle A_H \rangle$ and σ_A, respectively.*

E_0 (MeV)	$\langle E_x \rangle$ (MeV)	σ_{E_x} (MeV)	$\langle$TKE$\rangle$ (MeV)	σ_{TKE} (MeV)	$\langle A_H \rangle$ (amu)	σ_A (amu)
8.0	6.68	0.22	162.71±0.05	8.84±0.04	140.74±0.04	5.19±0.03
9.5	7.26	0.80	163.39±0.03	8.95±0.02	140.46±0.03	5.23±0.02

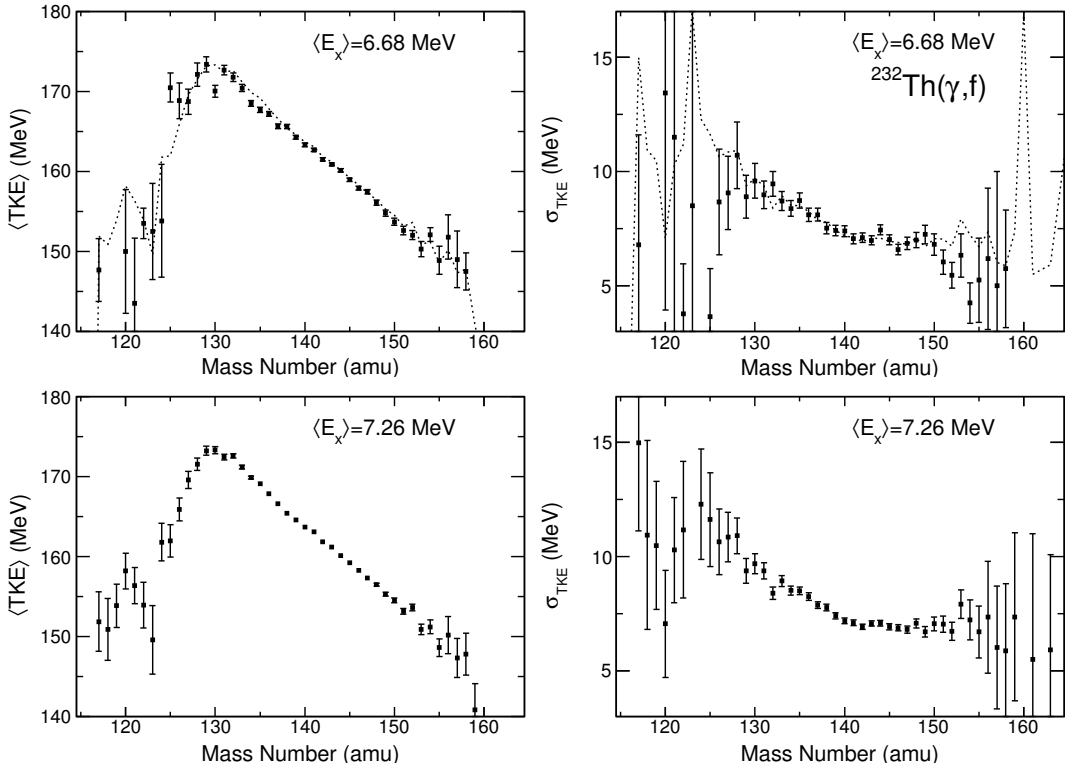

Fig. 5.8: *Average fragment TKE (left) and width (right) as a function of the fragment mass number for photofission of ^{232}Th with 8.0 and 9.5 MeV bremsstrahlung from top to bottom, obtained with a 87.0 $\mu g/cm^2$ target. The dotted line repeats the result obtained at 9.5 MeV bremsstrahlung. The error bars refer to statistical uncertainties only.*

5.2 Influence of Target Thickness

When correcting for energy loss in the target and backing materials, a constant specific energy loss must be assumed for all fragments. Furthermore, only the average energy loss as a function of emission angle can be determined and corrected for, corresponding to fission events taking place in the center of the target material. These shortcomings give rise to energy and mass resolution broadening, which due to the specific energy loss of fragments depend on the fragment mass, charge and energy. To quantify the conjecture that the discrepancies between results obtained with the different targets are due to this effect, a Monte-Carlo procedure was developed to fold the data obtained with the thinner target with the resolution of the thicker target.

Adding a UF_4 layer of thickness T will introduce an uncertainty in the depth, where the fission takes place inside the target. The energy loss of complementary fragments in the added layer can be approximated as

$$\begin{aligned}\Delta E_1 &= \left(\frac{1}{\rho}\frac{dE}{dx}\right)_U \cdot \frac{d}{\cos\theta} + 4\,\frac{m_F}{m_U} \cdot \left(\frac{1}{\rho}\frac{dE}{dx}\right)_F \cdot \frac{d}{\cos\theta} \quad \text{and} \\ \Delta E_2 &= \left(\frac{1}{\rho}\frac{dE}{dx}\right)_U \cdot \frac{T-d}{\cos\theta} + 4\,\frac{m_F}{m_U} \cdot \left(\frac{1}{\rho}\frac{dE}{dx}\right)_F \cdot \frac{T-d}{\cos\theta},\end{aligned} \tag{5.1}$$

where d is a depth parameter, see illustration in Fig. 5.9. To describe the specific energy loss, the Bethe-Bloch formula was used

$$\left(\frac{1}{\rho}\frac{dE}{dx}\right)_X = \kappa_X \frac{Z_X Z_{eff}^2}{\beta^2}\left[\ln\left(\frac{2m_e c^2}{\langle I\rangle_X}\cdot\frac{\beta^2}{1-\beta^2}\right) - \beta^2 - \left(\frac{C}{Z}\right)_X\right], \tag{5.2}$$

where

$$\kappa_X = \frac{3.071\cdot 10^{-7}}{A_X}\ \text{MeV}/(\mu\text{g/cm}^2),$$

and Z_X and A_X are proton and mass numbers of the target atom X, respectively, and β is the fragment's relativistic velocity. The mean excitation and ionization potentials $\langle I\rangle_X$ and the shell correction terms $\left(\frac{C}{Z}\right)_X$ were taken from Ref. [63]. The effective charge was estimated using an empirical expression for fission fragments [84],

$$\frac{Z_{eff}}{Z} = 1 - \left(1.034 - 0.177\cdot e^{-0.08114\cdot Z}\right) e^{-a}, \tag{5.3}$$

where

$$\begin{aligned}a &= b + 0.0378\cdot\sin\left(\frac{\pi}{2}b\right) \\ b &= 0.866\cdot\sqrt{\frac{E/\text{keV}}{25\cdot A}}\cdot Z^{-2/3},\end{aligned}$$

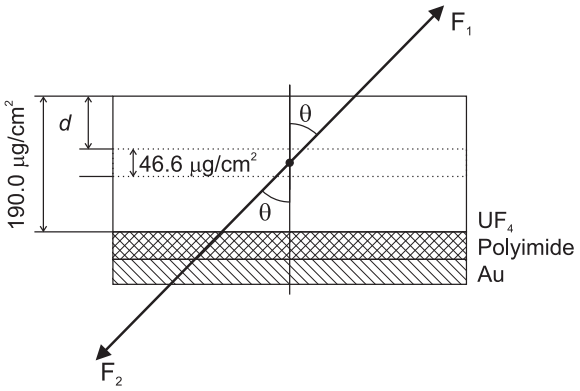

Fig. 5.9: *Illustration of the target composition and the angular dependent energy loss.*

and Z and A are the fragment's proton and mass numbers, respectively, and E its kinetic energy. The Monte-Carlo procedure uses the data of the experiment performed on ^{234}U at $E_0 = 9.0$ MeV with the 46.6 μg/cm^2 thick target. By randomizing $d \in [0, 143.4]$ μg/cm^2 for each event and using Eq. (5.1) a new data set is generated that corresponds to the experiment performed with the 190.0 μg/cm^2 target. This data set was then reanalyzed according to the procedure described in Sect. 4.3. The result of this analysis on the mass distribution and $\langle$TKE$\rangle$ as a function of fragment mass is presented in Fig. 5.10, solid red lines represent the result of the Monte-Carlo procedure, while full squares and open circles represent the experiments with the 46.6 μg/cm^2 and the 190.0 μg/cm^2 targets, respectively. The simulation reproduces the result obtained with the thicker target well. It can be concluded that the discrepancies observed for the two different targets used for the measurements of ^{234}U(γ, f) are indeed explained by an effect of a deteriorated resolution due to increased energy loss. Furthermore, it can be concluded that when performing 2E-experiments special attention should be paid to the quality of the target that is used, to avoid faulty conclusions.

The mass-resolution broadening in a 2E-experiment can be divided into two categories, the inherent and the instrumental contributions. The inherent contribution is due to the prompt neutron evaporation and is on average about 4 amu [85], while the instrumental contribution is mainly due to the uncertainty in the energy-loss correction, as discussed above. In order to avoid distortion of the mass distributions the target should be chosen so that the instrumental broadening does not exceed the inherent broadening. The instrumental mass-resolution broadening can be calculated using Eqs. (5.1)–(5.3). In Fig. 5.11 the results of such a calculation is presented for four different targets. The abscissa gives the input mass number and the ordinate gives the difference between the provisional masses for fissions taking place directly at the target surface ($d = 0$) and at the polyimide backing ($d = T$). As input to the calculation the experimentally obtained average post neutron

energies as a function of the provisional mass is used. The resolution broadening varies slightly with the mass number and shows a maximum for the symmetric mass splits. The fact that no strong deviations were observed in the case of ^{238}U(γ, f) at $E_0 = 8.5$ MeV between the data set obtained with the 130.3 μg/cm^2 and the 82.9 μg/cm^2 targets, indicates that the instrumental broadening is below the limit set by the prompt neutron evaporation in both cases.

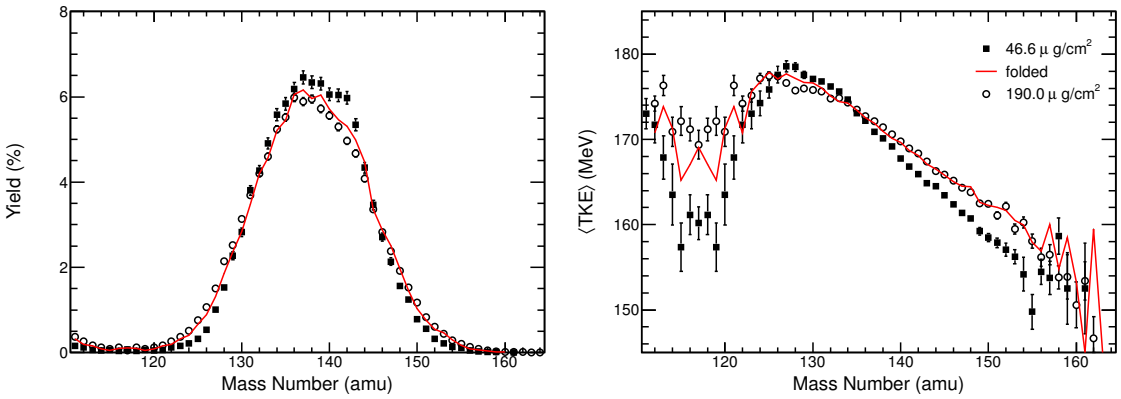

Fig. 5.10: *Fragment yield (left) and average* TKE *(right) as a function of the fragment mass number for* $^{234}U(\gamma, f)$ *at* $E_0 = 9.0$ *MeV. The open circles represent results obtained with the 190.0* $\mu g/cm^2$ *target, full squares represent results obtained with the 46.6* $\mu g/cm^2$ *target. The red line represent the simulated effect of the energy loss in the 190.0* $\mu g/cm^2$ *target on the data obtained with the 46.6* $\mu g/cm^2$ *target.*

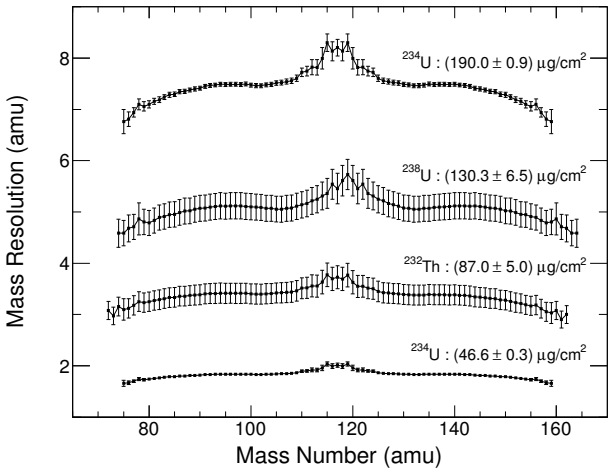

Fig. 5.11: *Mass resolution broadeing (FWHM) due to the uncertainty in the energy loss correction in a 2E-experiment as a function of the mass number for four different targets. The errorbars take the statistical uncertainty of the input data and the uncertainty of the target thickness into account.*

5.3 Angular Distributions

The fission-fragment angular distributions are parameterized by the theoretically expected angular distribution, given by the expression

$$W(\theta) = A + B\sin^2\theta + C\sin^2 2\theta, \tag{5.4}$$

which is normalized according to $\int_0^\pi W(\theta)\sin\theta d\theta = 1$. Before the parameterization, each obtained angular distribution is divided by an angular distribution determined for the alpha particle activity of the sample, in order to reduce experimental errors due to the response function of drift-time-to-cos θ conversion. Angles close to 90° are excluded from the fit, since this data is influenced by absorption and scattering in the target. Angles close to 0° are excluded as well, due to the uncertainty introduced by the limited angular resolution.

In Fig. 5.12 the angular distribution determined for ^{232}Th(γ, f) at bremsstrahlung endpoint energy $E_0 = 8.0$ MeV is shown as an example. The experimental data is obviously well described by the fit to Eq. (5.4), represented by the solid red line. As expected for the photofission of ^{232}Th, the angular distribution shows a distinct dipole pattern, peaked at $\theta = 90°$.

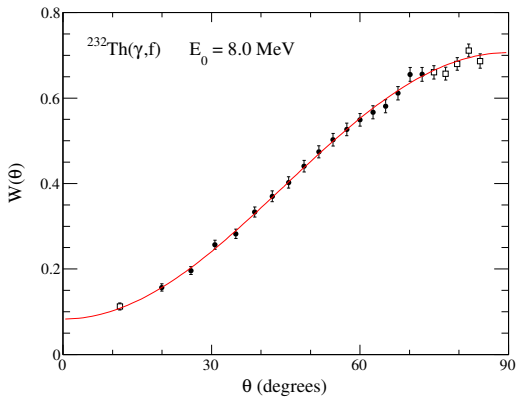

Fig. 5.12: *Fission-fragment angular distribution from ^{232}Th(γ, f) at bremsstrahlung endpoint energy $E_0 = 8.0$ MeV. The red line shows the fit of Eq. (5.4) to the region indicated by the full black circles.*

The dependence of the angular distribution parameters on the bremsstrahlung endpoint energy for ^{232}Th is shown in Fig. 5.13, previously taken data from Refs. [48, 86] is included for comparison. Evidently, the results are in good agreement with the existing literature data. The uncertainties from Ref. [48] are surprisingly small even-though the statistical

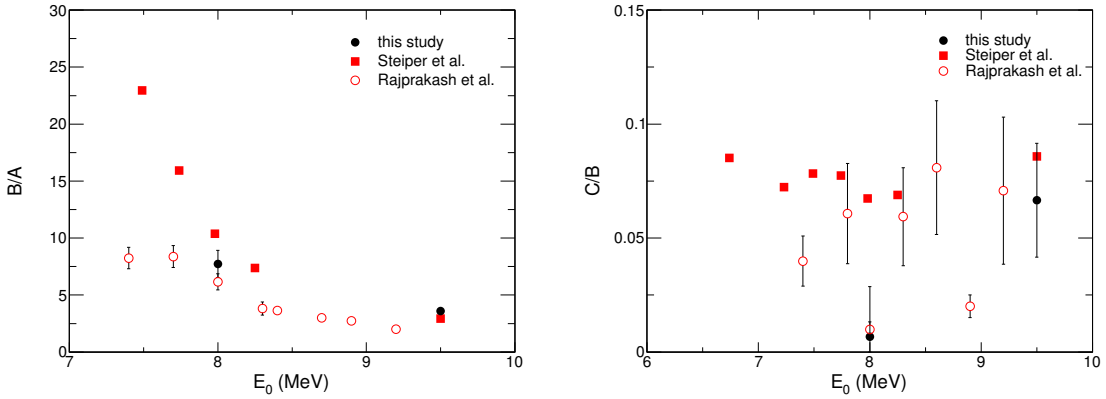

Fig. 5.13: $^{232}Th(\gamma, f)$ *angular distribution parameters in comparison with literature data [48, 86].*

accuracy are about the same as in this work. An increasing anisotropy, measured by the ratio B/A, is observed when lowering the bremsstrahlung endpoint energy. This behaviour is expected within the transition state concept for all even-even actinide nuclei due to a more predominant fission through the lower energy $(J^\pi, K) = (1^-, 0)$ channel [34]. The relative quadrupole contribution, measured by the ratio C/B, is expected to be very small and not to depend on the endpoint energy in the case of ^{232}Th, according to the systematics of the double humped fission barrier [87]. A sizable quadrupole contribution is only expected if the outer barrier is lower than the inner one. At the inner barrier the $(2^+, 0)$ transition state of the ground-state band lies lower in energy than the lowest lying dipole $(1^-, 0)$ transition state belonging to the mass-asymmetry band. At the outer barrier the dipole $(1^-, 0)$ and quadrupole $(2^+, 0)$ transition states are nearly degenerate, due to the preferred reflection asymmetric shape of the nucleus at large deformations. The relative quadrupole contribution is therefore controlled by the quadrupole-to-dipole photon absorption ratio, at the outer barrier. For light actinides the outer of the two barriers is expected to be the higher one of the two barrier humps. As observed in the right hand side of Fig. 5.13, the experimental data confirms this expectation.

The dependence of the angular distribution parameters on the bremsstrahlung endpoint energy for ^{234}U is shown in Fig. 5.14. The results are similar to those for ^{232}Th.

The measurements on ^{238}U was performed with the chamber tilted at a 45° relative to the beam axis. This complicates the angular distribution due to the loss of rotational symmetry around the beam axis. The angular distributions relative to the beam axis could, however, be extracted from data measured relative to the chamber axis, cf. Appendix A. The strong correlation of the angular distribution parameters extracted from this data reduces the accuracy of the result. In Fig. 5.15 the result for the ratios A/B and C/B

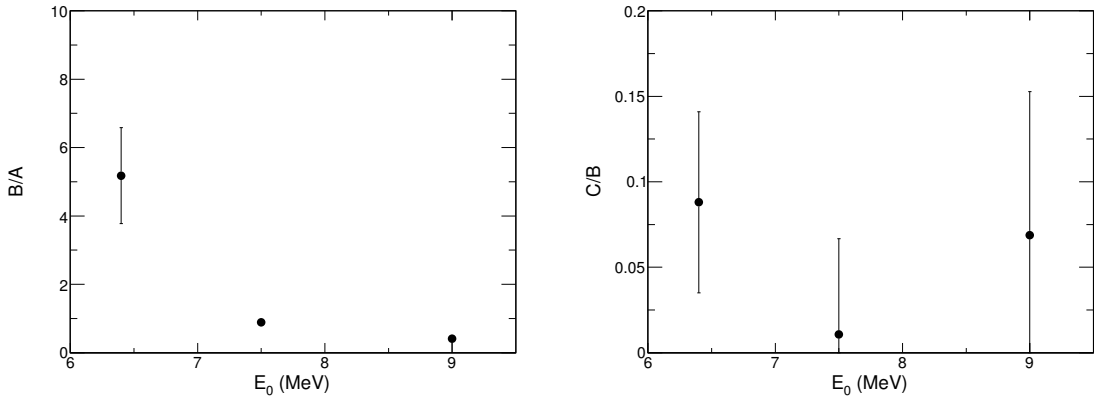

Fig. 5.14: $^{234}U(\gamma, f)$ *angular distribution parameters as a function of the bremsstrahlung endpoint energy from data obtained with a 46.6* $\mu g/cm^2$ *target.*

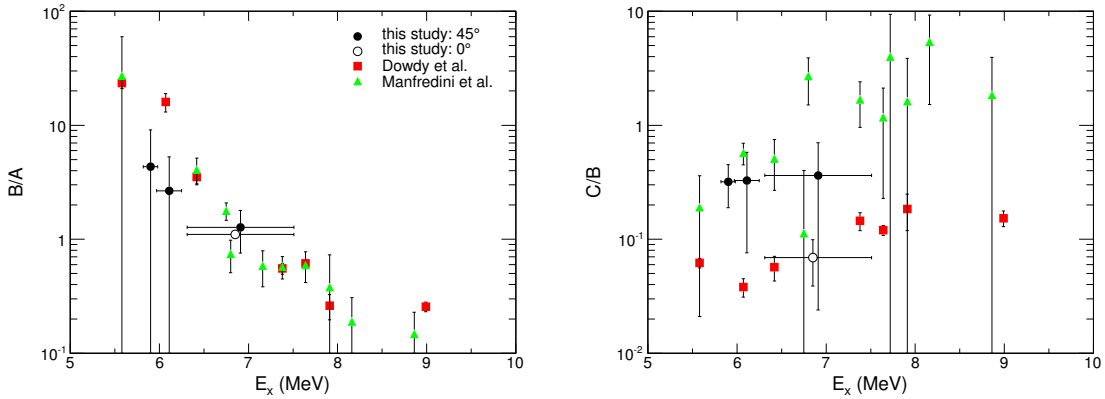

Fig. 5.15: $^{238}U(\gamma, f)$ *angular distribution parameters in comparison with data from Refs. [88, 89] for mono-energetic gamma rays as a function of the excitation energy. Data obtained with the ionization chamber in the 45° orientation is represented by full black circles, while data obtained with the ionization chamber in the 0° orientation by open black circles, for better visibility these data points has been shifted by 0.06 MeV to the left. The horizontal error bars indicate the standard deviation of the calculated excitation energy spectra.*

Tab. 5.5: *Angular distribution parameters from fit to Eq. (5.4). The last column gives the orientation of the detector relative to the beam axis, see text for details.*

	E_0 (MeV)	A	B	C	Detector Orientation
^{232}Th	9.5	0.16±0.01	0.48±0.01	0.03±0.02	0°
	8.0	0.08±0.01	0.63±0.01	0.004±0.014	0°
^{234}U	9.0	0.39±0.02	0.16±0.02	0.01±0.02	0°
	7.5	0.31±0.02	0.28±0.02	0.003±0.016	0°
	6.4	0.11±0.03	0.55±0.03	0.05±0.03	0°
^{238}U	8.5	0.282±0.009	0.310±0.008	0.021±0.009	0°
	8.5	0.24±0.06	0.30±0.28	0.11±0.03	45°
	7.0	0.15±0.11	0.41±0.30	0.13±0.04	45°
	6.5	0.15±0.16	0.64±0.25	0.21±0.03	45°

are plotted as a function of the average excitation energy. The horizontal error bars indicate the standard deviation of the excitation energy spectrum. The ratio B/A obtained in this study underestimates the ratio B/A from Refs. [88, 89] obtained with mono-energetic gamma rays. This can be understood as an effect of the use of bremsstrahlung. The slope of the decreasing B/A ratio in the region between 6 and 7 MeV will be flattened due to the extended excitation energy spectrum. For the purpose of calibration in the second measurement series, the measurement of ^{238}U(γ, f) was repeated at $E_0 = 8.5$ MeV, corresponding to $\langle E_x \rangle = 6.91$ MeV, then with the chamber axis oriented along the beam axis. As may be observed from Fig. 5.15 the angular distribution obtained in this measurement agrees well with the earlier data, but with much improved accuracy. The data obtained with the chamber in the 45° orientation overestimates the C/B ratio, as compared to the data point obtained with the chamber in the 0° orientation, but is compatible within the uncertainty.

Results for the angular distributions in the photofission of ^{232}Th, ^{234}U and ^{238}U are summarized in Tab. 5.5.

5.3.1 Mass Dependence of Angular Distributions

The first hint for a correlation between the fission-fragment masses and their angular distribution is shown in Fig. 5.16, where the left hand side shows the angular distribution from ^{234}U at $E_0 = 7.5$ MeV for a quasi-symmetric (S) and a far asymmetric (A) mass cut as defined on the right hand side. As may be observed, the fission fragments in these two regions show angular distribution patterns that are distinctively different from one another. Similar results for the angular distributions of symmetric and far asymmetric

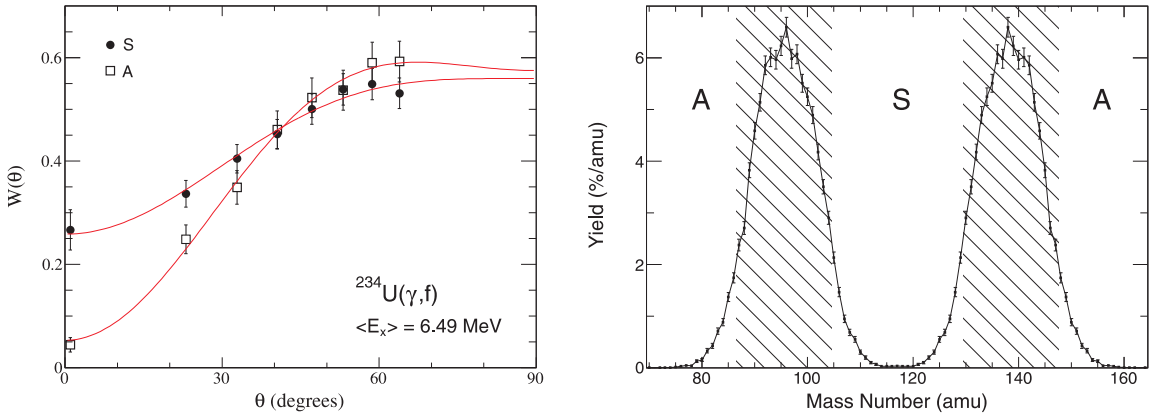

Fig. 5.16: *Angular distribution of fission fragments from* $^{234}U(\gamma, f)$ *at* $E_0 = 7.5$ *MeV in a symmetric (S) and an asymmetric (A) mass region, as indicated on the right hand side. Only events with* $\cos\theta \geq 0.4$ *are shown, since the mass cuts are not defined for lower values of* $\cos\theta$.

mass regions have earlier been found in the photofission of ^{236}U [47, 48]. The mass cuts introduced in Fig. 5.16 are rather arbitrarily chosen, and a more quantitative procedure is desirable. This is achieved by the introduction of a parameter M^*, according to

$$W(\theta, M^*) = \int_{A=M^*}^{\infty} W(\theta, A) dA, \tag{5.5}$$

where A is the heavy-fragment mass number. Similarly, for the TKE dependence a parameter TKE* is introduced, according to

$$W(\theta, \mathrm{TKE}^*) = \int_{\mathrm{TKE}=\mathrm{TKE}^*}^{\infty} W(\theta, \mathrm{TKE}) d(\mathrm{TKE}). \tag{5.6}$$

For each value of the parameters M^* and TKE* the expression in Eq. (5.4) is fitted to the resulting angular distribution. The result of applying this procedure on the ^{232}Th(γ, f) data at $E_0 = 9.5$ MeV is shown in Fig. 5.17, and for the ^{234}U(γ, f) data at $E_0 = 9.0$ MeV in Fig. 5.18. In the upper panels an increase in the anisotropy B/A correlated with an increase in M^* is seen for both ^{232}Th and ^{234}U, similarly an increase in the parameter TKE* is correlated with a decrease in the anisotropy B/A. This forms a consistent picture when keeping the $\langle \mathrm{TKE} \rangle(A)$ dependence in mind. For the asymmetric mass peak, the further away from symmetric mass splits, the lower is the TKE, neglecting the low yield symmetric component. The C/B ratios show more complex behaviors as functions of M^* and TKE*. The yield of the angular distribution component proportional to $\sin^2 2\theta$ is however small for all the experimental data and even takes on negative values for some values of M^* and TKE*. It is concluded that the angular distribution does indeed show

a dependence on both the mass and the TKE of the fission fragments. This result will be further discussed in Sect. 6.2.

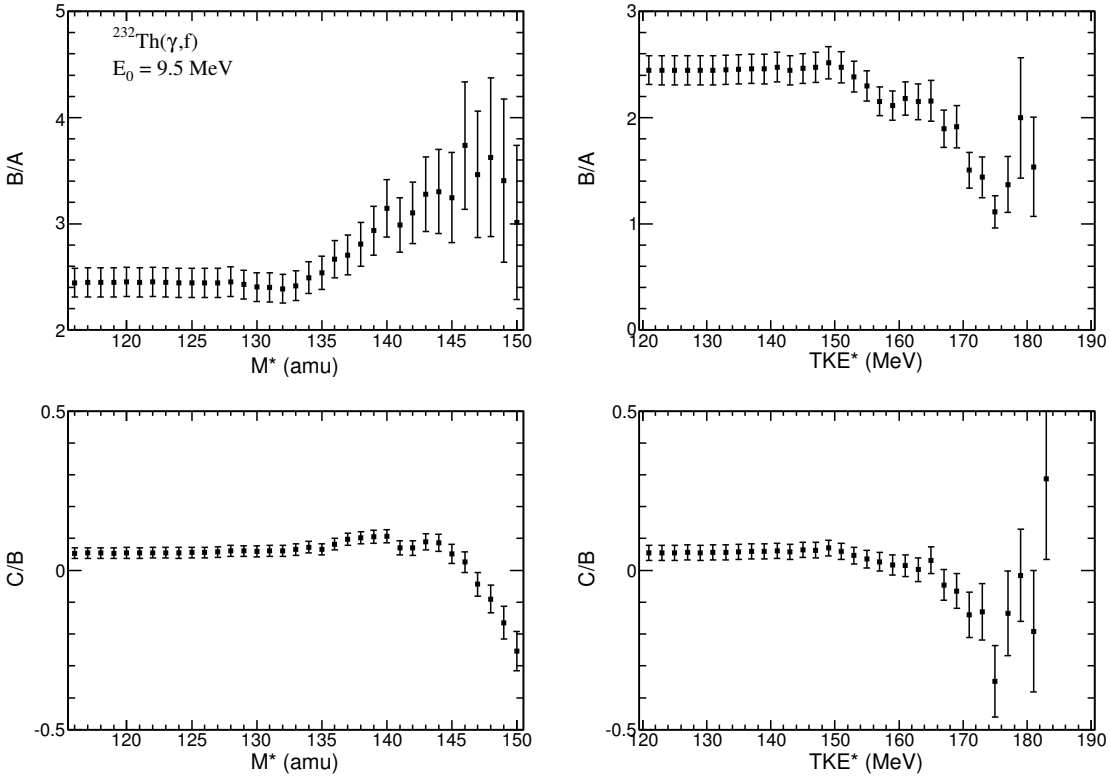

Fig. 5.17: *Dependence of fission-fragment angular distributions in* $^{232}Th(\gamma, f)$ *at* $E_0 = 9.5$ *MeV on the parameters* M^* *and* TKE^**, which are described in the text in more detail.*

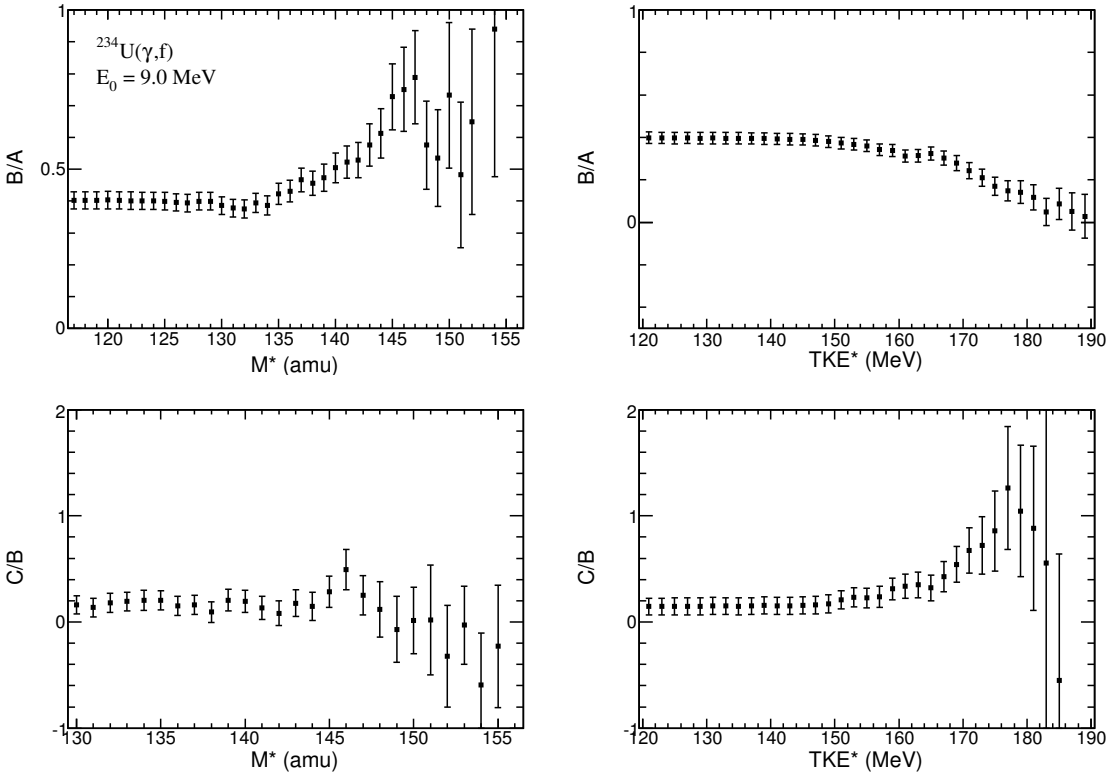

Fig. 5.18: *Dependence of fission-fragment angular distributions in* $^{234}U(\gamma, f)$ *at* $E_0 = 9.0$ *MeV on the parameters* M^* *and* TKE^* *(see text for details).*

Chapter 6

Discussion of the Experimental Results

6.1 Revisiting the Reaction $^{238}\mathrm{U}(\gamma, f)$

The motivation for the measurement of mass and TKE distributions from the reaction $^{238}\mathrm{U}(\gamma, f)$ was to validate the functionality of experimental setup and analysis procedure established in this work for photofission experiments of this type at the S-DALINAC. Since the measurement is also calibrated using the $^{238}\mathrm{U}$ data at $E_0 = 8.5$ MeV, comparison of the absolute values for characteristic mass and TKE serves little purpose. However, the PHD correction and the energy loss corrections based on the emission-angle information derived from the electron drift times, can be validated by comparing of the shape of the mass distribution, since errors in these corrections would also influence the shape of the mass distribution. In Fig. 6.1 the heavy-fragment pre-neutron mass distribution obtained at an average excitation energy $\langle E_x \rangle = 6.91$ MeV is compared to results from Ref. [17]. Clearly, the two distributions agree very well. Mean heavy-fragment pre-neutron mass and standard deviation of the mass peak obtained in this work, given in Tab. 5.1, are compared to values obtained in Ref. [17] as a function of the mean excitation energy in Fig. 6.2. The trend of increasing mean heavy-fragment mass with increasing excitation energy from Ref. [17] is also well reproduced in this work. As already mentioned, this trend can be attributed to a decrease in yield at masses above $A_H \sim 140$.

Fits performed within the constraints of the MM-RNR model, as described in Sect. 6.2, can be used to make a quantitative comparison of the experimental yield as a function of mass and TKE, if the fitted modes represent the data well. In Tab. 6.1 characteristics of the mass asymmetric standard fission modes obtained in this work are compared to results obtained in Ref. [17]. It is noted that mean heavy-fragment mass and mean TKE are in fair

agreement for both of the standard modes, although the mean heavy-fragment masses are consistently higher in the present study. The weight parameter w_{S1} is consistently larger in this study, as compared to Ref. [17], which coincides with a larger width σ_{S1} for the S1 mode.

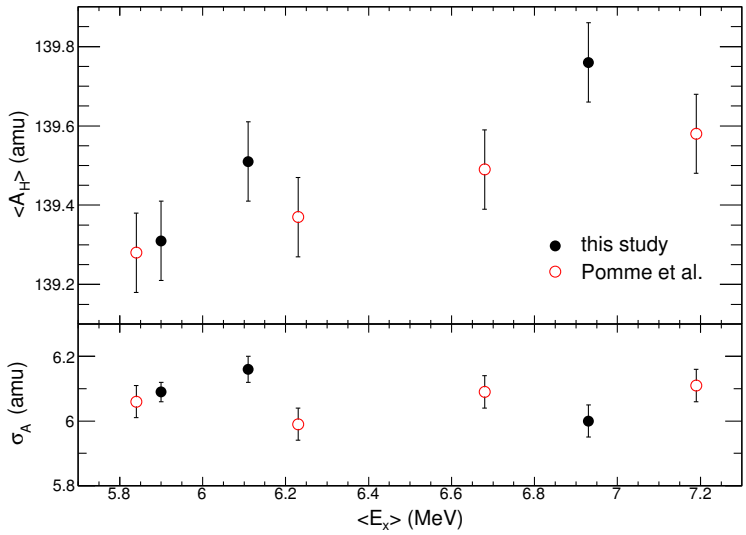

Fig. 6.1: *Mean heavy-fragment pre-neutron mass number and standard deviation of the mass peak from this work (closed black circles) as function of the average compound nucleus excitation energy is compared to the results of Ref. [17] (open red circles). The mean heavy fragment mass is drawn with systematic uncertainties of 0.1 amu.*

Tab. 6.1: *Comparison of characteristics of the fission modes obtained in this work to results reported in Ref. [17].*

E_0 (MeV)	w_{S1} (%)	$\langle A_H \rangle_{S1}$ (amu)	$\sigma_{A,S1}$ (amu)	$\langle TKE \rangle_{S1}$ (MeV)	w_{S2} (%)	$\langle A_H \rangle_{S2}$ (amu)	$\sigma_{A,S2}$ (amu)	$\langle TKE \rangle_{S2}$ (MeV)	Ref.
8.5	37.4	135.2	3.55	179.8	62.4	141.8	5.7	165.9	
8.35	29.2	134.8	3.15	181.9	70.4	141.2	5.8	166.6	[17]
7.33	33.3	135.1	3.32	182.3	66.5	140.8	5.7	165.9	[17]
7.0	35.1	135.3	3.57	180.7	64.6	141.3	6.1	165.5	
6.5	36.9	135.1	3.55	180.8	62.9	141.3	5.9	165.1	
6.44	29.2	134.7	3.11	180.3	70.4	141.2	5.7	165.9	[17]

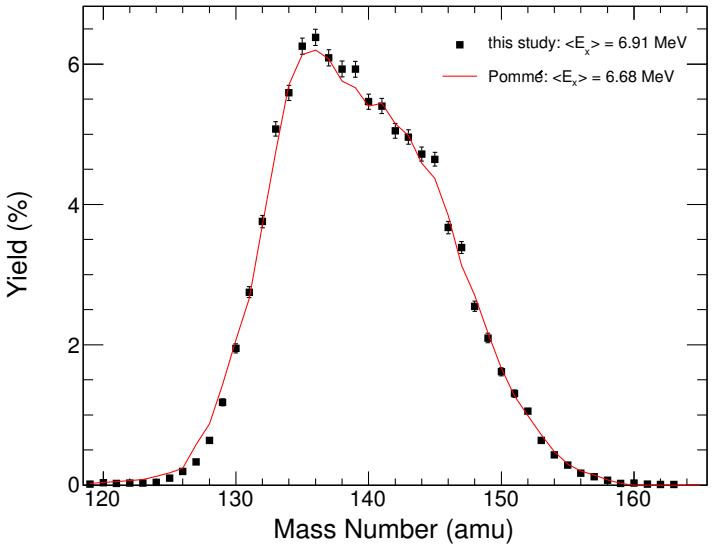

Fig. 6.2: *Heavy-fragment pre-neutron mass distribution at* $\langle E_x \rangle = 6.91$ *MeV compared to the mass distribution at* $\langle E_x \rangle = 6.68$ *MeV obtained in Ref. [17].*

6.2 Fission-Mode Analysis

Further investigation of the data was made within the framework of the MM-RNR model (see Sect. 2.3.2). As mentioned earlier, the yield predicted in this model is a superposition of the yields from individual fission modes. To extract information on the characteristics of the involved modes and their relative importance, a fit to the experimentally obtained yield as a function of fragment mass and TKE is made of the expression

$$\begin{aligned} Y(A,\mathrm{TKE}) =& \sum_m w_m Y_m(A,\mathrm{TKE}), \\ Y_m(A,\mathrm{TKE}) =& \frac{1}{4\pi\sigma_{A,m}} \left[\exp\left(-\frac{(A-\langle A\rangle_m)^2}{2\sigma_{A,m}^2} \right) + \exp\left(-\frac{(A-A_f+\langle A\rangle_m)^2}{2\sigma_{A,m}^2} \right) \right] \\ & \times \left(\frac{200}{\mathrm{TKE}} \right)^2 \exp\left(\frac{-(L-l_{max,m})^2}{(L-l_{min,m})l_{dec,m}} \right), \end{aligned} \tag{6.1}$$

where the index m denotes a fission mode. The distance between the fragments' charge centers at scission is denoted by L. Considering only Coulomb interaction this quantity may be approximated by

$$L = \frac{Z_L Z_H e^2}{\mathrm{TKE}} = 1.44 \text{ MeV·fm} \left(\frac{Z_f}{A_f} \right)^2 \frac{(A_f - A)A}{\mathrm{TKE}}.$$

The part describing the mass distribution is a simple superposition of two Gaussians, one for the heavy fragment and one for the light fragment. For symmetry reasons both use the same set of parameters for each mode: the mean heavy-fragment mass number $\langle A \rangle_m$ and the width σ_A, m of the mass yield. The part describing the TKE uses three parameters for the distance between the fragments' charge centers at scission, with the following intuitive meanings:

- The most probable distance is denoted l_{max},
- the smallest allowed distance, due to Q-value limitation, by l_{min}.
- The exponential decrease in yield with simultaneous increase in L is described by l_{dec}.

In the fission of light actinides three modes are predicted to play a role (see Sect. 2.3.2 for details), the super-long (SL) mode, which is symmetric in mass with low TKE, and the two mass-asymmetric so-called standard modes (S1, S2) centered around the masses 135 and 141, respectively. In total the fit-function then has 18 parameters. The fits were performed using the method of maximum log-likelihood and the Minuit computer code [90, 91]. In Figs. 6.3 and 6.4 fission-fragment yields as a function of mass and TKE are displayed. The red ellipses labeled SL, S1 and S2 are contours at 67% of the maximum yield of the corresponding fission mode, resulting from the fit.

Results of the fits of Eq. (6.1) to the experimental data are summarized in Tabs. 6.2 - 6.4. The mode-weights w_m in Eq. (6.1) are not strictly proportional to the relative yields Y_m of the fission modes. Both w_m and Y_m are referred to as the mode weight in the literature. For clarity both quantities are therefore given in the tables. In Figs. 6.6 - 6.13 the results of the fits are shown for the individual data sets. As evident in these figures and by the reduced χ^2 values, the individual fits describe the respective experimental data well. Included in Tabs. 6.2 - 6.4 are predicted values of the fission mode characteristic mass and TKE distributions [7]. The predicted $\langle A_H \rangle$ are fixed by the asymmetry of the prescission shape, calculated from the potential energy landscape, while σ_A is connected to the elongation of the neck by the random neck rupture mechanism. A compact scission configuration is, because of the Coulomb repulsion, characterized by a high TKE and will, due to the random-neck-rupture mechanism, lead to a narrow mass distribution. A more elongated neck will lead to a lower TKE and a wider mass distribution. Examining Tabs. 6.2 - 6.4, this systematic is clearly observed in the experimental data. Uncertainties in the predictions of the mass distributions are in the order of 3 amu for the average heavy-fragment masses and 25% for the mass widths. The predicted mass distributions do indeed agree fairly well with the experimentally obtained ones. However, the predicted $\langle$TKE$\rangle$ overestimate the experimentally obtained ones, by $\sim$5 MeV for the S1 mode in all the nuclei and by $\sim$7 MeV for the S2 mode in the uranium nuclei and by $\sim$10 MeV in ^{232}Th, this is a substantial deviation even when taking the uncertainty of $\sim$5 MeV in the

predicted ⟨TKE⟩ into account. Similarly, the predicted widths of the TKE distributions are also overestimated.

In Fig. 6.5 the relative yield of the S1 mode is shown as a function of the average compound nucleus excitation energy. Evidently, no strong variation of the mode weights as a function of excitation energy is found. This observation is in agreement with the potential energy calculations by Brosa et al. [7], where the two standard modes bifurcate after passing a common outer barrier. With a common outer barrier only secondary effects play a role in modulating the relative importance of the two standard modes, and no order-of-magnitude changes in the mode weights are expected. When drawing conclusions about the excitation-energy dependence, the width of the excitation-energy spectra must be kept in mind.

The S1 and S2 modes can be associated with the spherical $N = 82$ and the deformed $N \approx 88$ neutron shells of the scission point model (cf. Sect 2.3.1), respectively. A systematic behavior of the relative importance of the two standard modes with the neutron number of the fissioning system may therefore be expected. On the right-hand side of Fig. 6.5 the relative yields of the S1 mode, averaged over the excitation energies is plotted as a function of the neutron numbers of the fissioning nuclei; data from Refs. [83, 92, 93] is also included. A systematic behavior is indeed recognized. The behavior can be qualitatively explained by the interplay of the two neutron shells with the spherical proton shell $Z = 50$, cf. Ref. [93]. The increasing yield of the S1 mode with increasing neutron number may be connected with the fact that the larger the neutron number of the fissioning nucleus is, the closer the Z/A ratio comes to that of a doubly magic heavy-fragment with $Z = 50$ and $N = 82$.

Referring to the results on the influence of the target thickness presented in Sect. 5.2, it is interesting to investigate the effect of the target thickness on the results of the fission mode fits. In Tab. 6.5 the results of the fit to the data obtained with the 46.6 μg/cm^2 target is compared to the fit to the data obtained with the 190.0 μg/cm^2 target, with bremsstrahlung of endpoint energy of 9.0 MeV. The fit to the data obtained with the thicker target did not converge when all three fission modes were included, therefore the low yield SL mode had to be excluded from the fit. A smaller weight for the S1 mode is observed for the thicker of the two targets. Also included in Tab. 6.5 are results of a fit to the data obtained from the Monte-Carlo procedure described in Sect. 5.2. The result of the fit to the folded data agrees well with the fit to the data obtained with the thicker target, which corroborates the conclusions drawn in Sect. 5.2.

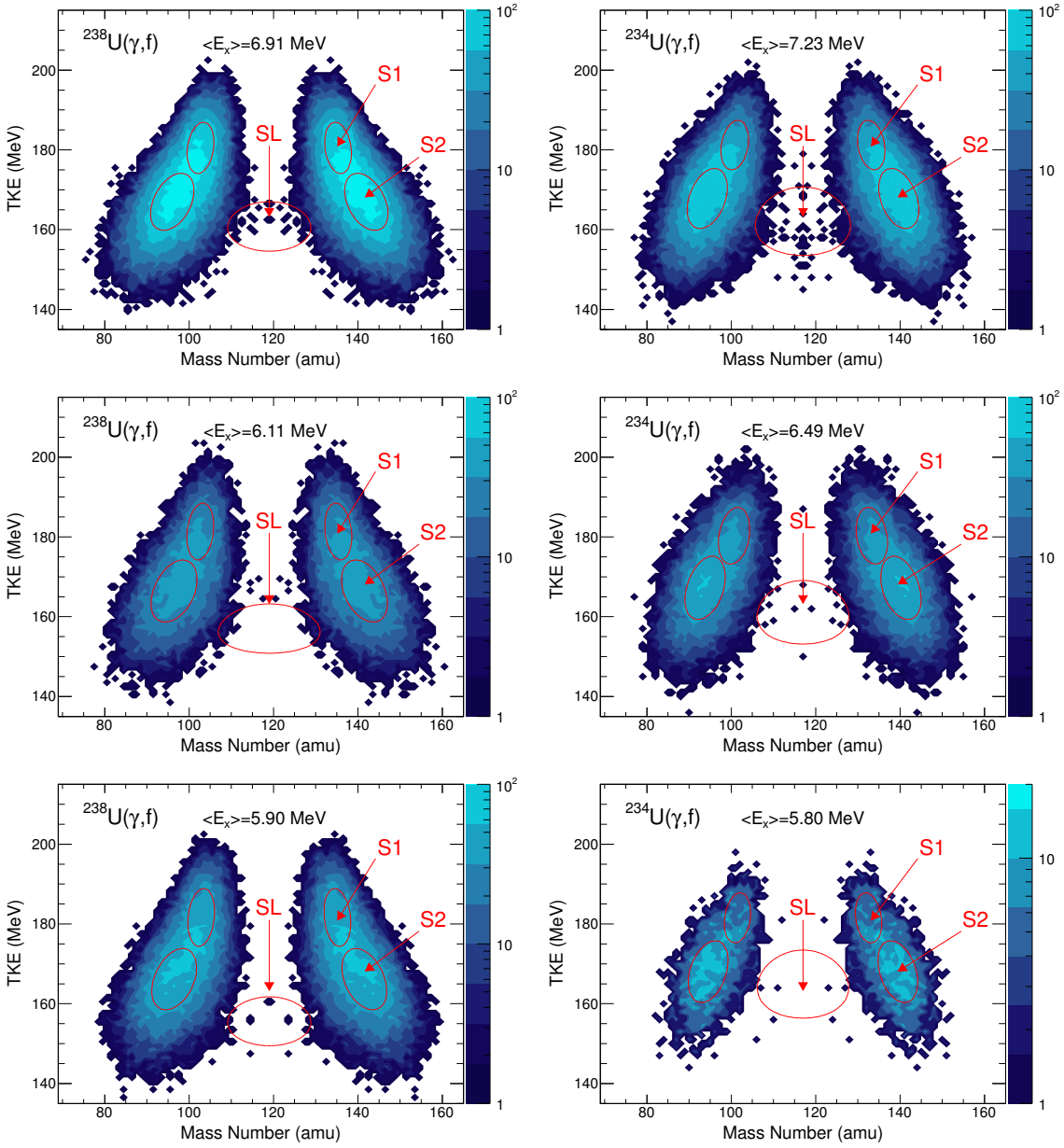

Fig. 6.3: *Logarithmic contour plots of fission-fragment yield as a function of pre-neutron fragment-mass number and TKE. Left: For the reaction* $^{238}U(\gamma,f)$ *at* $\langle E_x \rangle = 6.91$, *6.11 and 5.90 MeV. Right: For the reaction* $^{234}U(\gamma,f)$ *at* $\langle E_x \rangle = 7.23$, *6.49 and 5.80 MeV. The color scales indicated the number of counts per amu and MeV. The ellipses labeled S1, S2 and SL are contours at 67% of the maximum yield of the corresponding fission modes.*

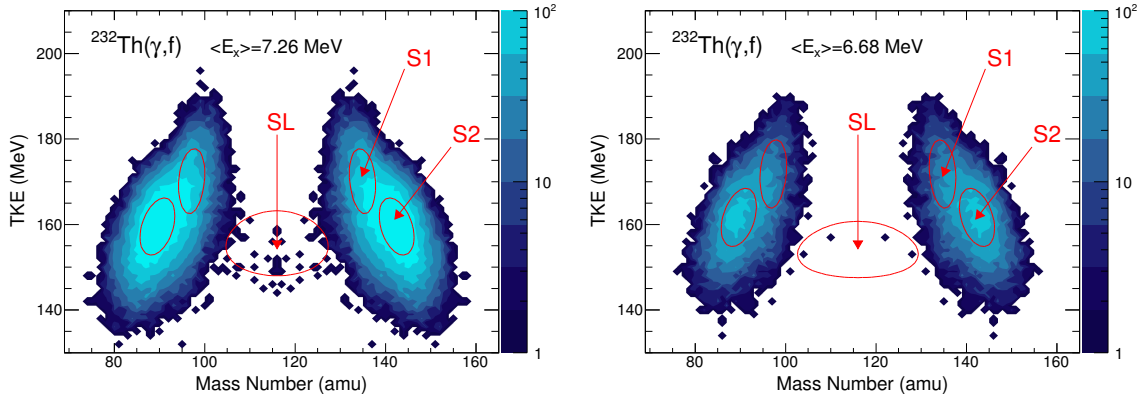

Fig. 6.4: *Logarithmic contour plots of fission-fragment yield as a function of pre-neutron fragment-mass number and TKE for the reaction $^{232}Th(\gamma,f)$ at $\langle E_x \rangle = 7.26$ and 6.68 MeV. The color scales indicated the number of counts per amu and MeV. The ellipses labeled S1, S2 and SL are contours at 67% of the maximum yield of the corresponding fission modes.*

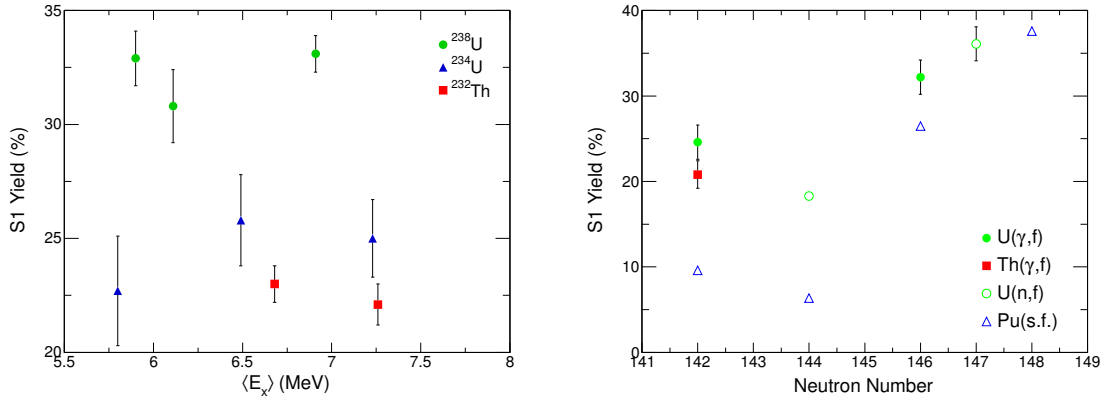

Fig. 6.5: *Left: Relative yield of the S1 mode as a function of the average excitation energy of the compound nucleus for the photofission of ^{238}U (green circles), ^{234}U (blue triangles) and ^{232}Th (red squares) determined in this work. Right: The relative yield of the S1 mode averaged over the excitation energies as a function of the neutron number of the compound nucleus, literature data on neutron induced fission of ^{235}U [92] and ^{238}U [83] as well as spontaneous fission of four different Pu-isotopes [93] is included for comparison.*

Tab. 6.2: *Characeristics of the fission modes from fitting the ^{238}U data obtained with the 130.3 $\mu g/cm^2$ target to Eq. (6.1). Given are the average excitation energies of the compound nucleus $\langle E_x \rangle$, the reduced chi squared $\tilde{\chi}^2$ of the fit, the relative yield Y and weight w, as well as average heavy-fragment mass number $\langle A_H \rangle$, mass width σ_A, average total kinetic energy $\langle \mathrm{TKE} \rangle$ and total kinetic energy width σ_{TKE}, of the fitted fission modes. Values marked (*) were kept fixed during the fitting. Also included are theoretical predictions [7] of the characteristics.*

$\langle E_x \rangle$ (MeV)	$\tilde{\chi}^2$		Y (%)	w (%)	$\langle A_H \rangle$ (amu)	σ_A (amu)	$\langle \mathrm{TKE} \rangle$ (MeV)	σ_{TKE} (MeV)
6.91	1.2	S1	33.1 ± 0.8	37.4 ± 0.6	135.2 ± 0.1	3.55 ± 0.03	179.8 ± 0.2	7.2 ± 0.1
		S2	66.6 ± 0.8	62.4 ± 0.8	141.8 ± 0.1	5.72 ± 0.03	165.9 ± 0.1	8.0 ± 0.1
		SL	0.2 ± 0.1	0.2 ± 0.1	119.0 *	10.9 ± 1.0	157.4 ± 1.3	7.6 ± 0.7
6.11	1.1	S1	30.8 ± 1.6	35.1 ± 1.0	135.3 ± 0.1	3.57 ± 0.06	180.7 ± 0.3	8.0 ± 0.1
		S2	68.9 ± 1.7	64.6 ± 1.7	141.3 ± 0.1	6.07 ± 0.06	165.5 ± 0.2	8.7 ± 0.1
		SL	0.3 ± 0.1	0.3 ± 0.1	119.0 *	13.1 ± 3.0	153.2 ± 2.4	7.7 ± 1.8
5.90	1.0	S1	32.9 ± 1.2	36.9 ± 0.8	135.1 ± 0.1	3.55 ± 0.05	180.8 ± 0.2	8.1 ± 0.1
		S2	66.9 ± 1.3	62.9 ± 1.3	141.3 ± 0.1	5.92 ± 0.05	165.1 ± 0.1	8.6 ± 0.1
		SL	0.3 ± 0.1	0.2 ± 0.1	119.0 *	10.9 ± 0.3	152.4 ± 1.9	7.4 ± 0.2
theory		S1			134.0	3.4	186	9.0
		S2			141.0	5.9	176	9.5
		SL			117.0	12.9	155	10.5

Tab. 6.3: *Characeristics of the fission modes from fitting the ^{234}U data obtained with the 46.6 $\mu g/cm^2$ target to Eq. (6.1). Given are the average excitation energies of the compound nucleus $\langle E_x \rangle$, the reduced chi squared $\tilde{\chi}^2$ of the fit, the relative yield Y and weight w, as well as average heavy-fragment mass number $\langle A_H \rangle$, mass width σ_A, average total kinetic energy $\langle \mathrm{TKE} \rangle$ and total kinetic energy width σ_{TKE}, of the fitted fission modes. Values marked (*) were kept fixed during the fitting. Also included are theoretical predictions [7] of the characteristics.*

$\langle E_x \rangle$ (MeV)	$\tilde{\chi}^2$		Y (%)	w (%)	$\langle A_H \rangle$ (amu)	σ_A (amu)	$\langle \mathrm{TKE} \rangle$ (MeV)	σ_{TKE} (MeV)
7.23	1.07	S1	25.0 ± 1.7	27.1 ± 1.0	133.1 ± 0.1	3.7 ± 0.1	181.0 ± 0.3	6.9 ± 0.1
		S2	74.5 ± 1.7	72.3 ± 1.4	139.5 ± 0.1	5.3 ± 0.1	166.8 ± 0.1	8.4 ± 0.1
		SL	0.4 ± 0.1	0.6 ± 0.2	117.0 *	12.3 ± 2.8	159.1 ± 1.8	9.8 ± 2.3
6.49	1.04	S1	25.8 ± 2.0	30.1 ± 1.4	133.2 ± 0.2	4.1 ± 0.1	180.0 ± 0.4	7.1 ± 0.2
		S2	73.8 ± 2.0	69.5 ± 2.1	140.0 ± 0.2	5.3 ± 0.1	165.8 ± 0.1	9.0 ± 0.1
		SL	0.4 ± 0.1	0.3 ± 0.1	117.0 *	11.9 ± 1.7	160.0 ± 2.5	11.8 ± 1.7
5.80	1.04	S1	22.7 ± 2.4	28.8 ± 2.5	132.5 ± 0.3	3.5 ± 0.2	181.3 ± 0.7	7.0 ± 0.4
		S2	76.8 ± 2.6	70.9 ± 2.8	139.3 ± 0.2	5.2 ± 0.1	166.5 ± 0.3	8.6 ± 0.2
		SL	0.5 ± 0.3	0.4 ± 0.2	117.0 *	11.9 ± 0.1	161.9 ± 0.4	9.7 ± 0.0
theory		S1			134.0	3.4	186	9.0
		S2			141.0	5.9	176	9.5
		SL			117.0	12.9	155	10.5

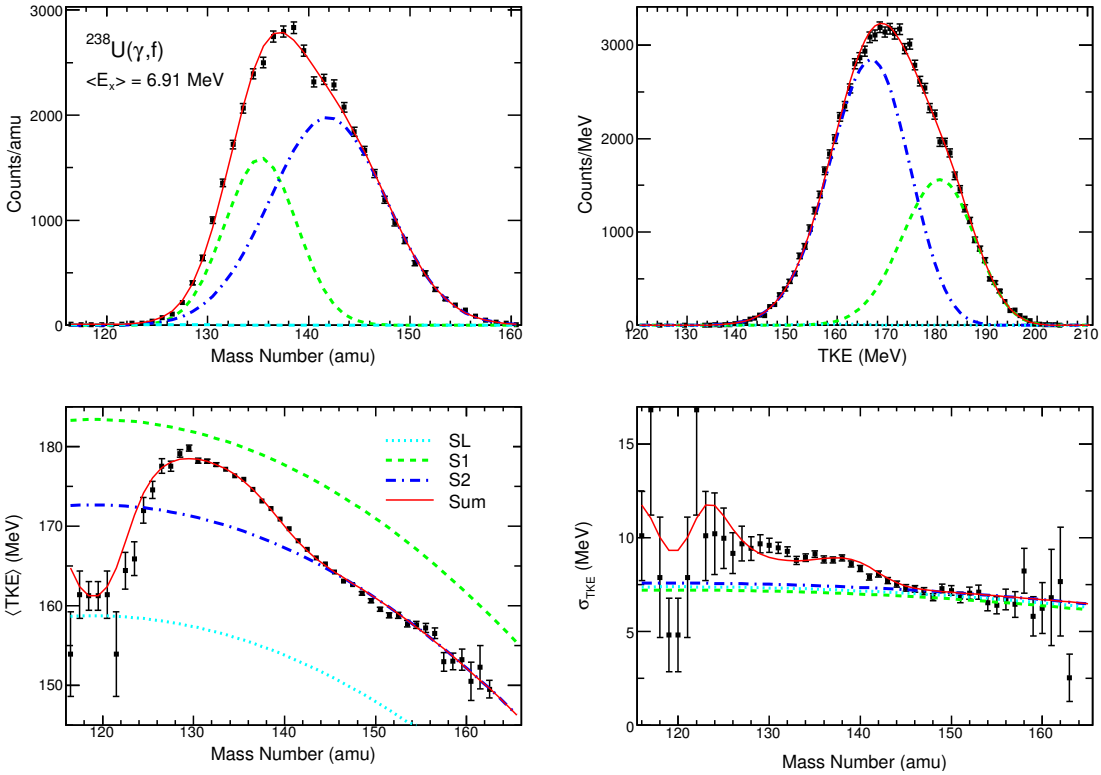

Fig. 6.6: *Fission-fragment yield as a function of mass (top left) and TKE (top right) as well as average TKE (bottom left) and width (bottom right) as function of the fragment mass from* $^{238}U(\gamma, f)$ *at* $\langle E_x \rangle = 6.91$ *MeV. The solid red line represent results from fits according to Eq. (6.1), the different colored lines are the model components.*

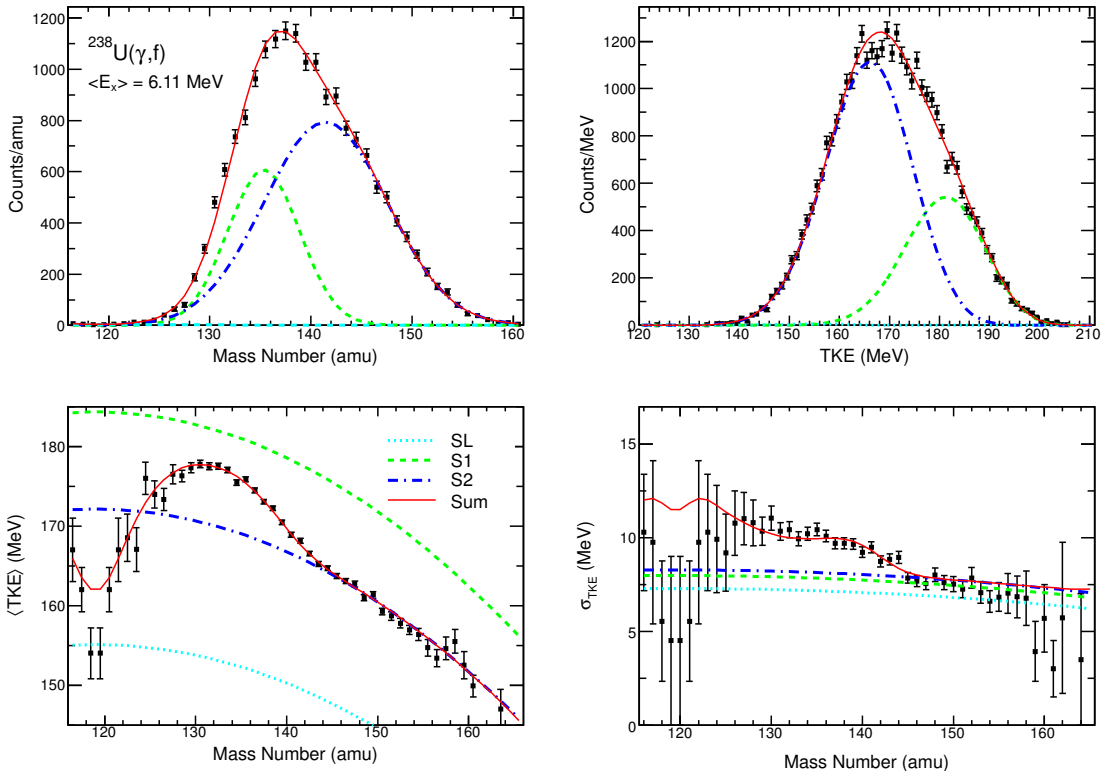

Fig. 6.7: *Fission-fragment yield as a function of mass (top left) and TKE (top right) as well as average TKE (bottom left) and width (bottom right) as function of the fragment mass from* $^{238}U(\gamma, f)$ *at* $\langle E_x \rangle = 6.11$ *MeV. The solid red line represent results from fits according to Eq. (6.1), the different colored lines are the model components.*

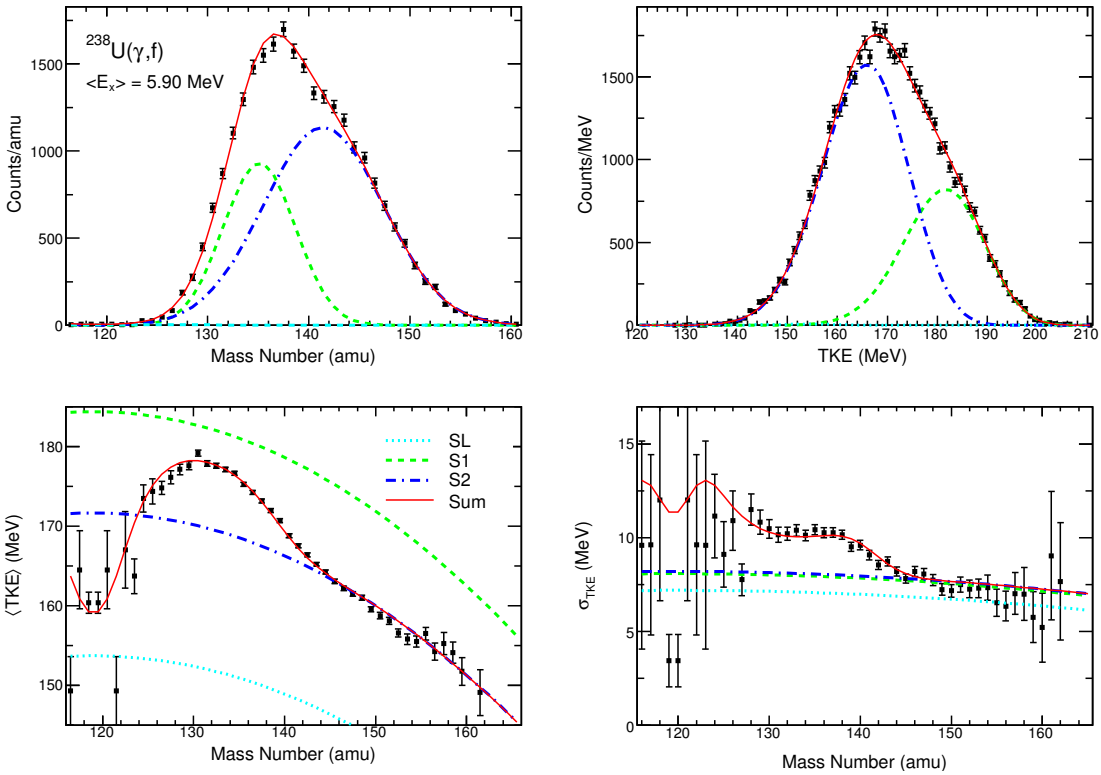

Fig. 6.8: *Fission-fragment yield as a function of mass (top left) and TKE (top right) as well as average TKE (bottom left) and width (bottom right) as function of the fragment mass from* $^{238}U(\gamma, f)$ *at* $\langle E_x \rangle = 5.90$ *MeV. The solid red line represent results from fits according to Eq. (6.1), the different colored lines are the model components.*

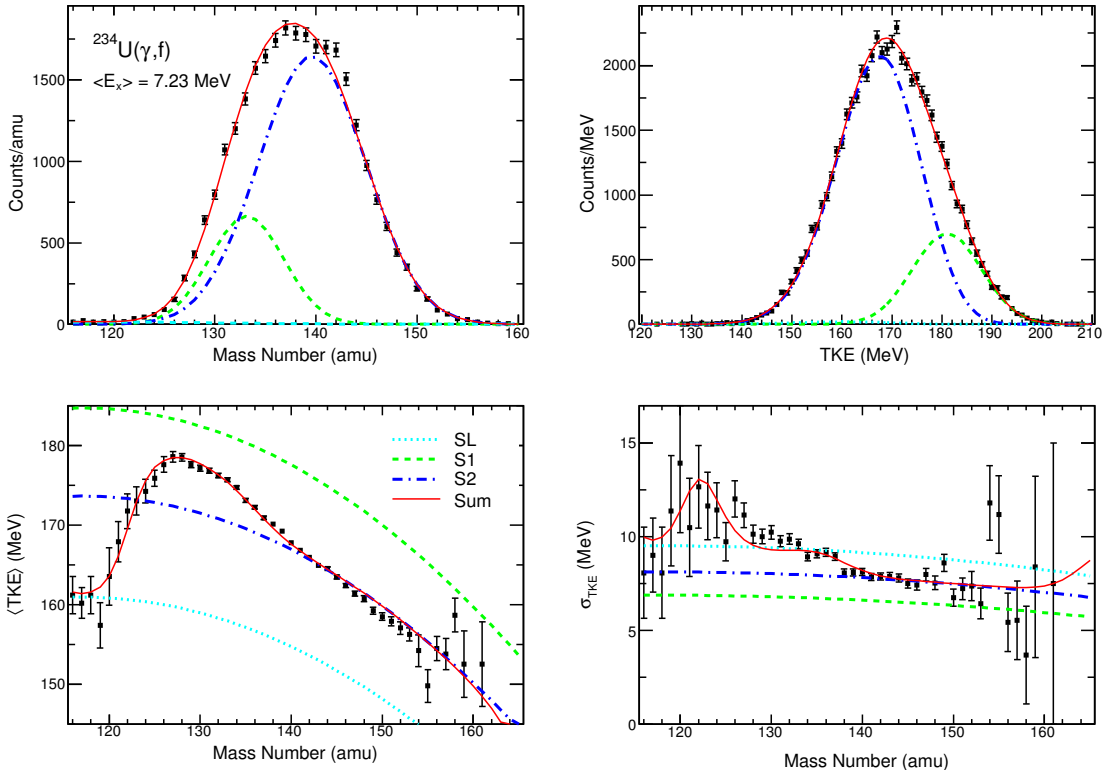

Fig. 6.9: *Fission-fragment yield as a function of mass (top left) and TKE (top right) as well as average TKE (bottom left) and width (bottom right) as function of the fragment mass from* $^{234}U(\gamma, f)$ *at* $\langle E_x \rangle = 7.23$ *MeV, obtained with a 46.6* $\mu g/cm^2$ *target. The solid red line represent results from fits according to Eq. (6.1), the different colored lines are the model components.*

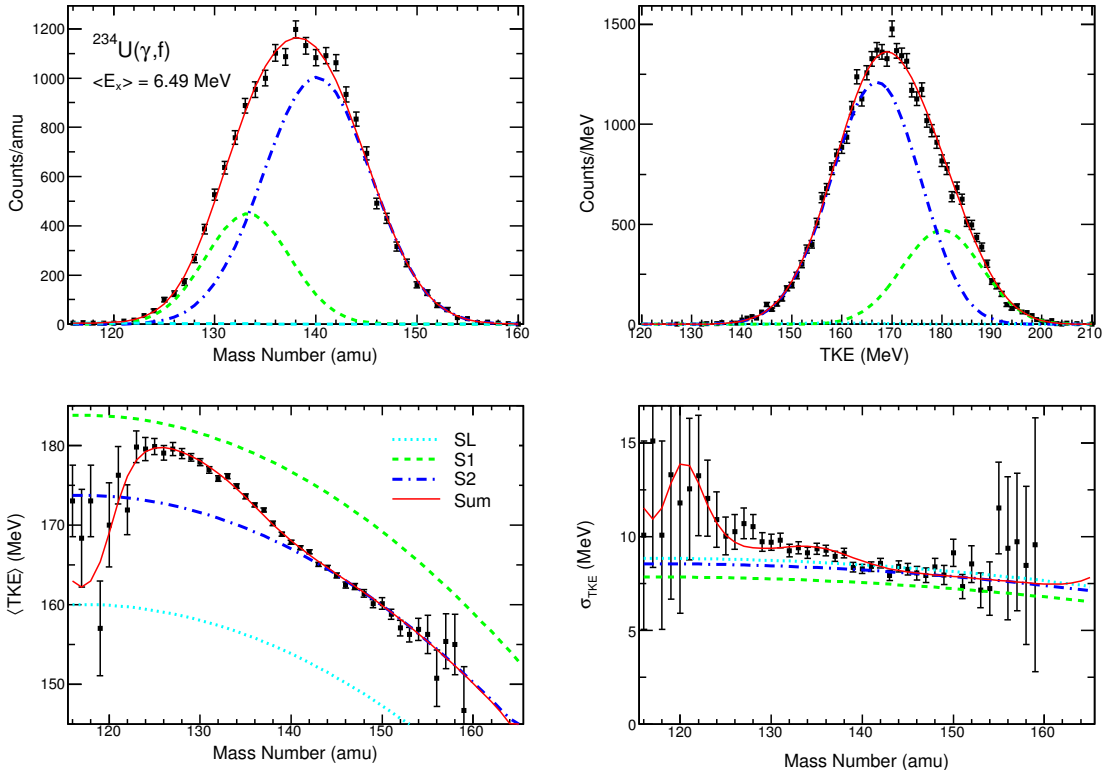

Fig. 6.10: *Fission-fragment yield as a function of mass (top left) and* TKE *(top right) as well as average* TKE *(bottom left) and width (bottom right) as function of the fragment mass from* $^{234}U(\gamma, f)$ *at* $\langle E_x \rangle = 6.49$ *MeV, obtained with a 46.6* $\mu g/cm^2$ *target. The solid red line represent results from fits according to Eq. (6.1), the different colored lines are the model components.*

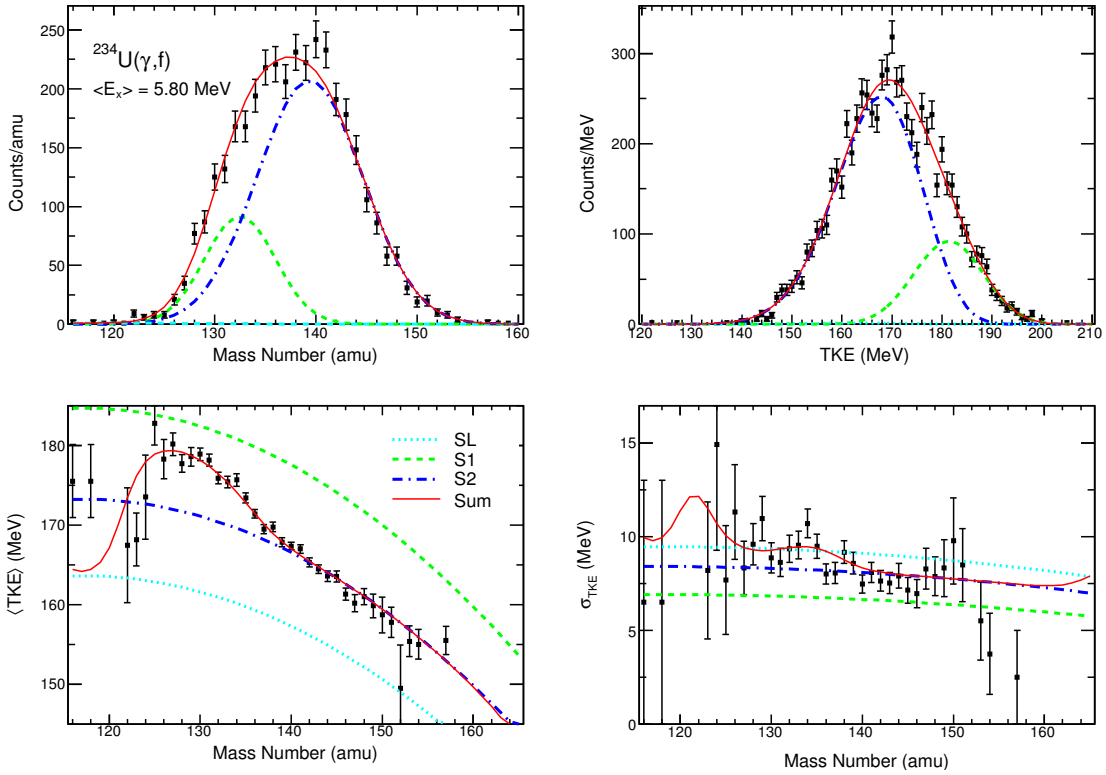

Fig. 6.11: *Fission-fragment yield as a function of mass (top left) and* TKE *(top right) as well as average* TKE *(bottom left) and width (bottom right) as function of the fragment mass from* $^{234}U(\gamma, f)$ *at* $\langle E_x \rangle = 5.80$ *MeV, obtained with a 46.6* $\mu g/cm^2$ *target. The solid red line represent results from fits according to Eq. (6.1), the different colored lines are the model components.*

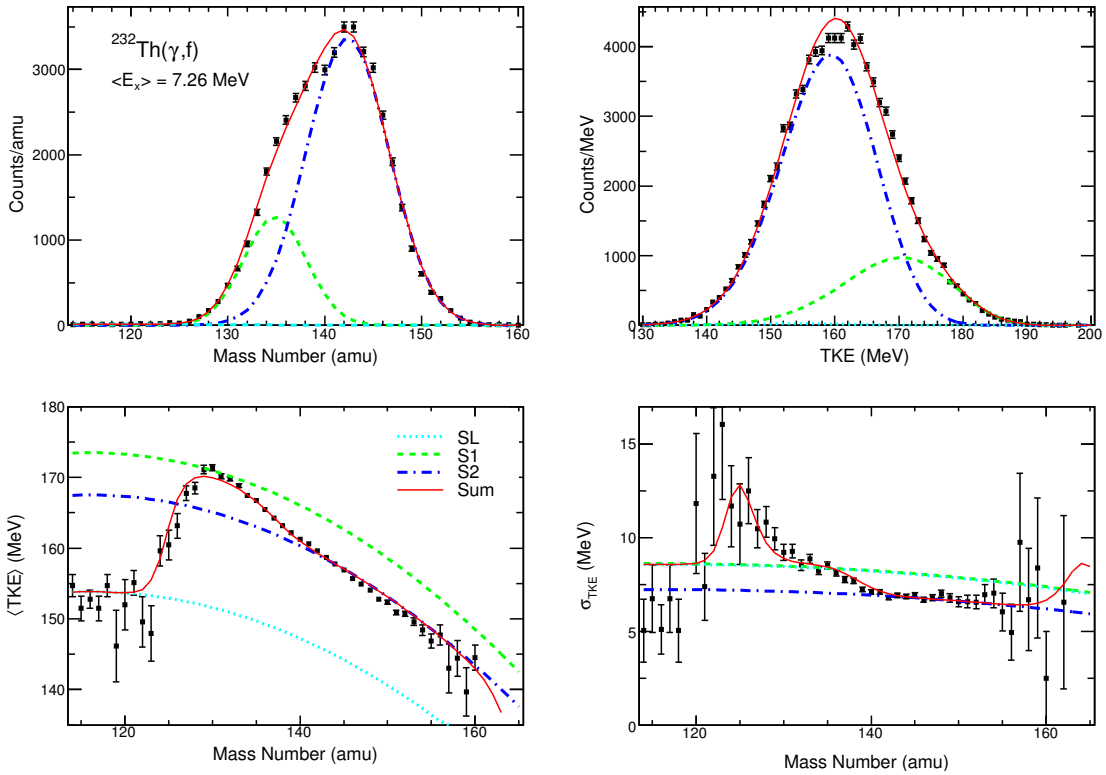

Fig. 6.12: *Fission-fragment yield as a function of mass (top left) and* TKE *(top right) as well as average* TKE *(bottom left) and width (bottom right) as function of the fragment mass from* $^{232}Th(\gamma, f)$ *at* $\langle E_x \rangle = 7.26$ *MeV. The solid red line represent results from fits according to Eq. (6.1), the different colored lines are the model components.*

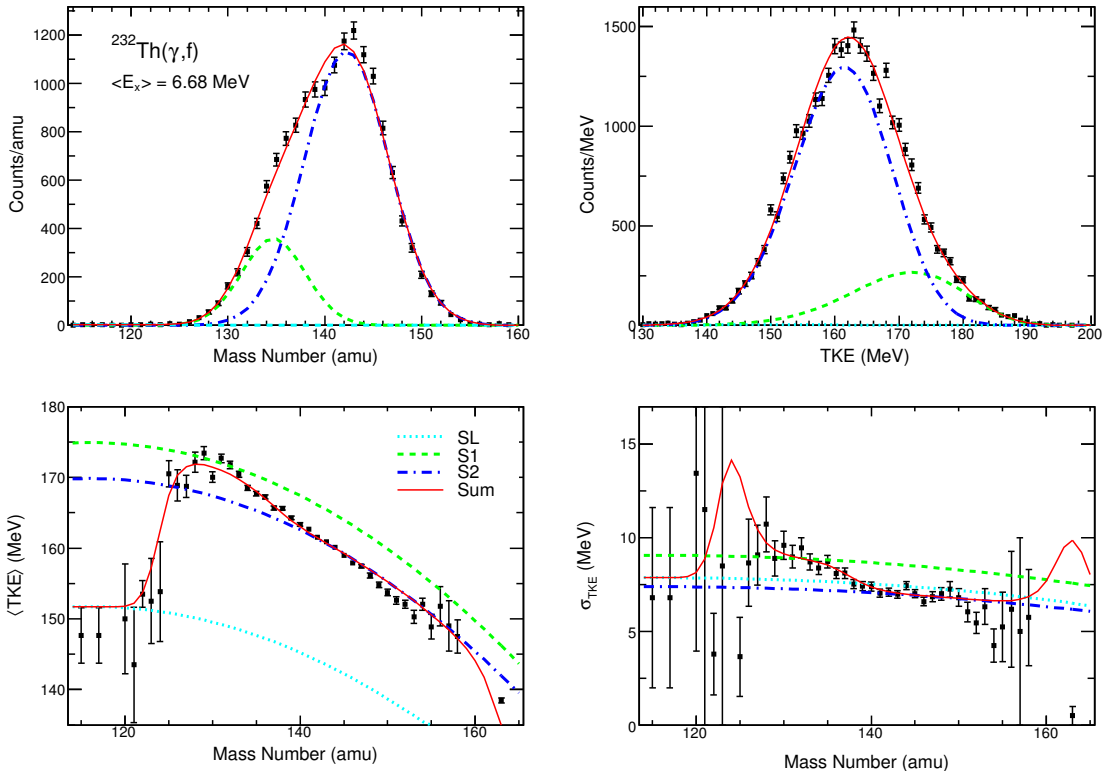

Fig. 6.13: *Fission-fragment yield as a function of mass (top left) and* TKE *(top right) as well as average* TKE *(bottom left) and width (bottom right) as function of the fragment mass from* $^{232}Th(\gamma, f)$ *at* $\langle E_x \rangle = 6.68$ *MeV. The solid red line represent results from fits according to Eq. (6.1), the different colored lines are the model components.*

Tab. 6.4: *Characeristics of the fission modes from fitting the ^{232}Th data obtained with the 87.0 $\mu g/cm^2$ target to Eq. (6.1). Given are the average excitation energies of the compound nucleus $\langle E_x \rangle$, the reduced chi squared $\tilde{\chi}^2$ of the fit, the relative yield Y and weight w, as well as average heavy-fragment mass number $\langle A_H \rangle$, mass width σ_A, average total kinetic energy $\langle \mathrm{TKE} \rangle$ and total kinetic energy width σ_{TKE}, of the fitted fission modes. Values marked (*) were kept fixed during the fitting. Also included are theoretical predictions [7] of the characteristics.*

$\langle E_x \rangle$ (MeV)	$\tilde{\chi}^2$		Y (%)	w (%)	$\langle A_H \rangle$ (amu)	σ_A (amu)	$\langle \mathrm{TKE} \rangle$ (MeV)	σ_{TKE} (MeV)
7.26	1.46	S1	22.1 ± 0.9	21.1 ± 0.8	134.8 ± 0.1	3.25 ± 0.05	171.3 ± 0.2	8.7 ± 0.1
		S2	77.4 ± 0.9	78.5 ± 0.9	142.3 ± 0.1	4.29 ± 0.03	161.3 ± 0.1	7.5 ± 0.1
		SL	0.5 ± 0.4	0.42 ± 0.0	116.0 *	12.3 ± 2.2	154.3 ± 2.9	9.2 ± 1.6
6.68	1.32	S1	23.0 ± 0.8	18.7 ± 0.7	135.3 ± 0.1	3.71 ± 0.08	170.3 ± 0.2	8.9 ± 0.2
		S2	76.9 ± 1.0	71.7 ± 0.9	142.6 ± 0.1	4.29 ± 0.04	160.8 ± 0.1	7.6 ± 0.1
		SL	0.1 ± 0.3	9.57 ± 26.50	116.0 *	8.3 ± 2.92	149.5 ± 3.6	8.9 ± 3.1
theory		S1			135.0	4.1	176	10.3
		S2			139.0	5.7	168	11.3
		SL			116.0	9.2	155	9.8

Tab. 6.5: *Comparison of the results of the fits of Eq. (6.1) to the data obtained with the 46.6 $\mu g/cm^2$ and the 190.0 $\mu g/cm^2$ targets. The last column gives results for the simulated effect of the added target thickness according to Sect. 5.2. Values marked (*) were kept fixed during the fitting.*

target	$\tilde{\chi}^2$		Yield (%)	w (%)	$\langle A_H \rangle$ (amu)	σ_A (amu)	l_{max} (fm)	l_{min} (fm)	l_{dec} (fm)
46.6 μg/cm^2	1.07	S1	25.0 ± 1.7	27.1 ± 1.0	133.1 ± 0.1	3.66 ± 0.07	16.45 ± 0.02	9.0 ± 2.1	0.10 ± 0.04
		S2	74.5 ± 1.7	72.3 ± 1.4	139.5 ± 0.1	5.29 ± 0.05	17.37 ± 0.01	12.9 ± 0.2	0.28 ± 0.01
		SL	0.4 ± 0.1	0.59 ± 0.2	117.0 *	12.3 ± 2.8	18.61 ± 0.21	14.1 ± 2.0	0.51 ± 0.20
190.0 μg/cm^2	1.21	S1	12.3±2.2	13.8±1.2	133.6±0.3	4.5±0.2	16.5±0.03	11.8*	0.33±0.01
		S2	87.7±2.2	86.2±1.2	138.40±0.04	6.50±0.03	17.08±0.01	11.8*	0.369±0.003
		SL		0.0*					
simulation	1.00	S1	8.7±1.8	12.6±0.9	133.5±0.2	3.8±0.2	16.22±0.03	11.8*	0.127±0.01
		S2	91.3±1.8	87.4±0.9	138.57±0.06	6.20±0.03	17.16±0.01	11.8*	0.230±0.003
		SL		0.0*					

6.2.1 Interpretation of the Mass Dependence of Angular Distributions

As mentioned in Sect. 2.3.2, a mass (and TKE) dependence of the angular distribution is expected within the MM-RNR model, when separate fission barriers are associated with each mode. Since the yield of each mode has been determined from the fits to Eq. (6.1), the expected dependence of the angular distribution,

$$\begin{aligned} W(A, \mathrm{TKE}, \theta) &= \sum_m W_m(\theta) \cdot Y_m(A, \mathrm{TKE}) \\ &= \sum_m \left(A_m + B_m \sin^2\theta + C_m \sin^2 2\theta \right) \cdot Y_m(A, \mathrm{TKE}), \end{aligned} \tag{6.2}$$

can be used to calculate the expected dependence of the angular distribution parameters A, B and C on the parameters M^* and TKE* , as introduced in Sect. 5.3.1. Since the yield of the SL mode is very low for all data sets (cf. Tabs. 6.3 and 6.4), it has been neglected in the following analysis. For each of the angular distribution parameters, one obtains two equations describing their dependence on M^* and TKE*, respectively. Using the equations describing the dependences on one of the parameters M^* (or TKE*) the mode-specific angular distribution parameters A_m, B_m and C_m can be determined from a fit to the experimental data. If Eq. (6.2) is valid, the same set of parameters must also describe the dependence on the second of the two parameters TKE* (or M^*). In Figs. 6.14 and 6.15 the data from ^{232}Th(γ, f) at $E_0 = 9.5$ MeV and ^{234}U(γ, f) at $E_0 = 9.0$ MeV, also presented earlier in Figs. 5.17 and 5.18 are repeated, however, this time with the calculated behavior according to the above discussion shown by the solid red lines. In Figs. 6.16 and 6.17 the same is also shown for the data from ^{234}U(γ, f) at $E_0 = 7.5$ MeV and $E_0 = 6.4$ MeV. The fit was performed to the angular distribution dependence on TKE*, since the larger deviations were observed there. The mode-specific angular distribution parameters were determined in such a way that the fit function exactly reproduces the parameters obtained when all experimental data is included (TKE$^* = 0$). The predicted dependence of the angular distributions on M^* does indeed describe the data quite well, in particular the ratio B/A, which is sensitive to the fission-barrier height. Deviations in the B/A ratio might arise due to the decreasing statistical accuracy with increasing values of M^* and TKE*, and due to errors in the assumed mass and TKE distributions of the two modes.

The ratios B/A of the angular distribution coefficients determined for the two standard modes in ^{232}Th(γ, f) and ^{234}U(γ, f) are plotted as function of the bremsstrahlung endpoint energy in Fig. 6.18. The uncertainties in these ratios take in to account the uncertainties in the fitted dependence and the uncertainties in the angular distribution parameters when all experimental data is included (TKE$^* = 0$). In a static model of the potential energy landscape the outer barrier of the S2 mode is expected to be smaller than that of the S1 mode, since the relative contribution of the S2 mode to the fission yield is predominant throughout the actinide region of nuclei. With a smaller barrier for the S2 mode a lower

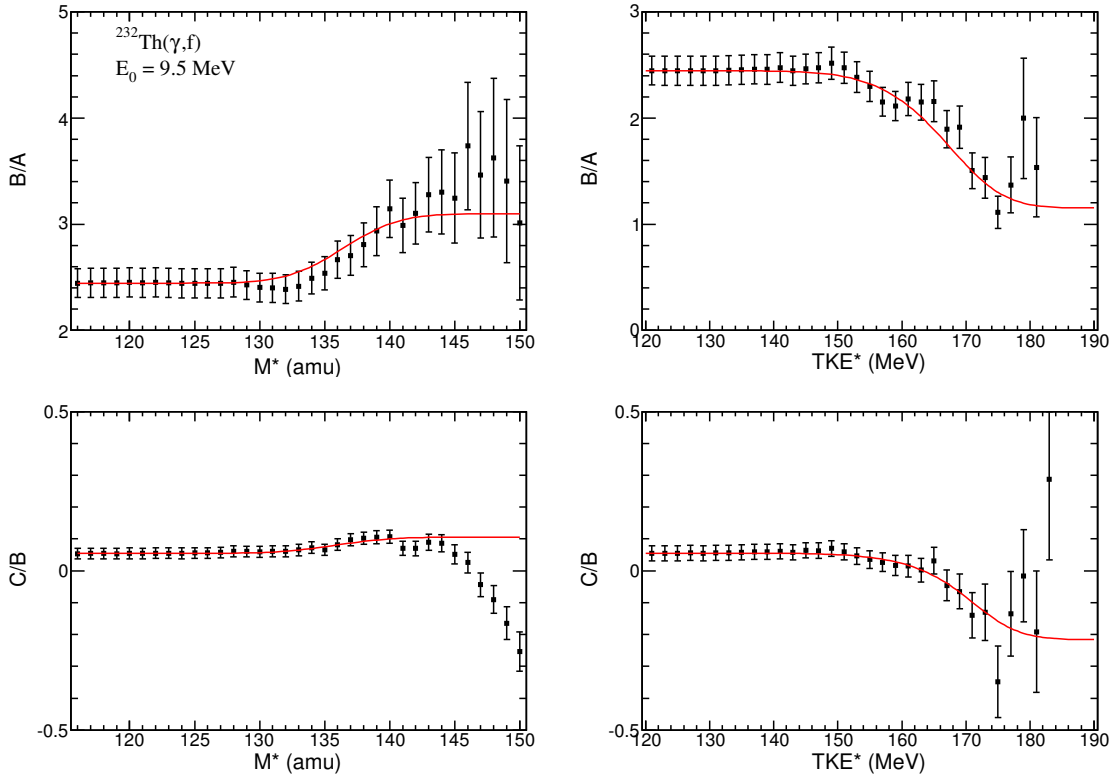

Fig. 6.14: *Dependence of fission-fragment angular distributions in* $^{232}Th(\gamma, f)$ *at* $E_0 = 9.5$ *MeV on the parameters* M^* *(left) and* TKE^* *(right), as introduced in Sect. 5.3.1. The solid red lines show the expected behavior assuming specific angular distributions for the the two standard modes.*

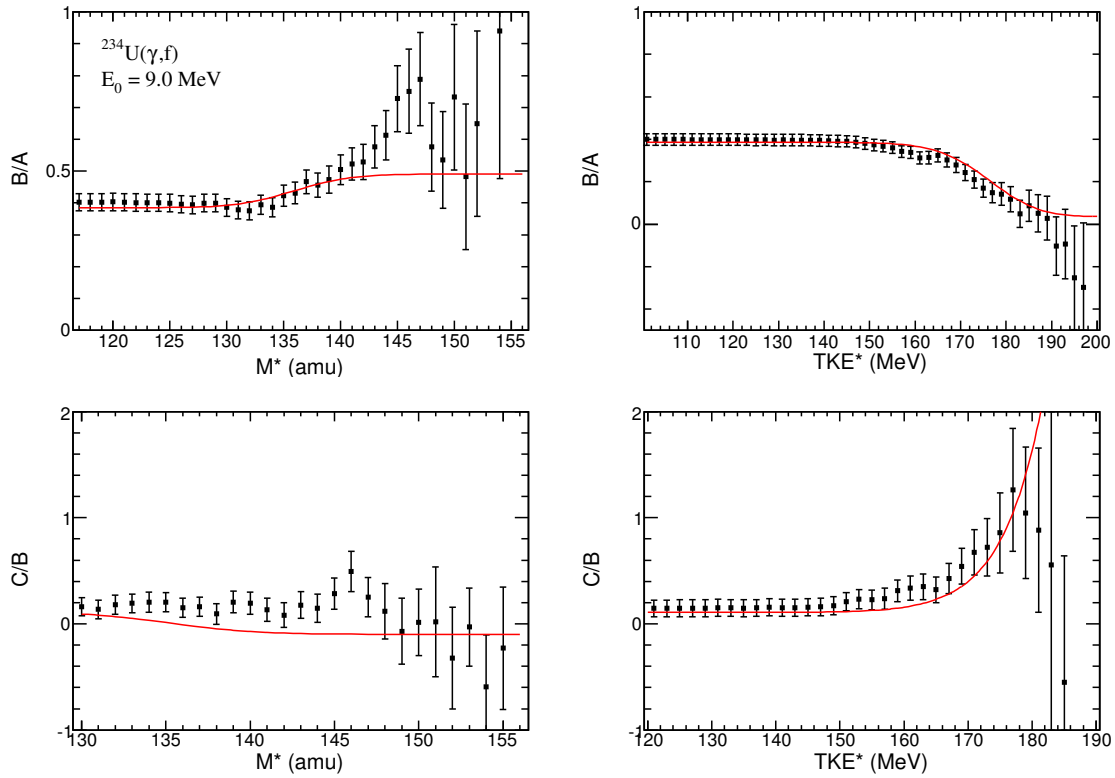

Fig. 6.15: *Dependence of fission-fragment angular distributions in* $^{234}U(\gamma, f)$ *at* $E_0 = 9.0$ *MeV on the parameters* M^* *(left) and* TKE^* *(right), as introduced in Sect. 5.3.1. The solid red lines show the expected behavior assuming specific angular distributions for the the two standard modes.*

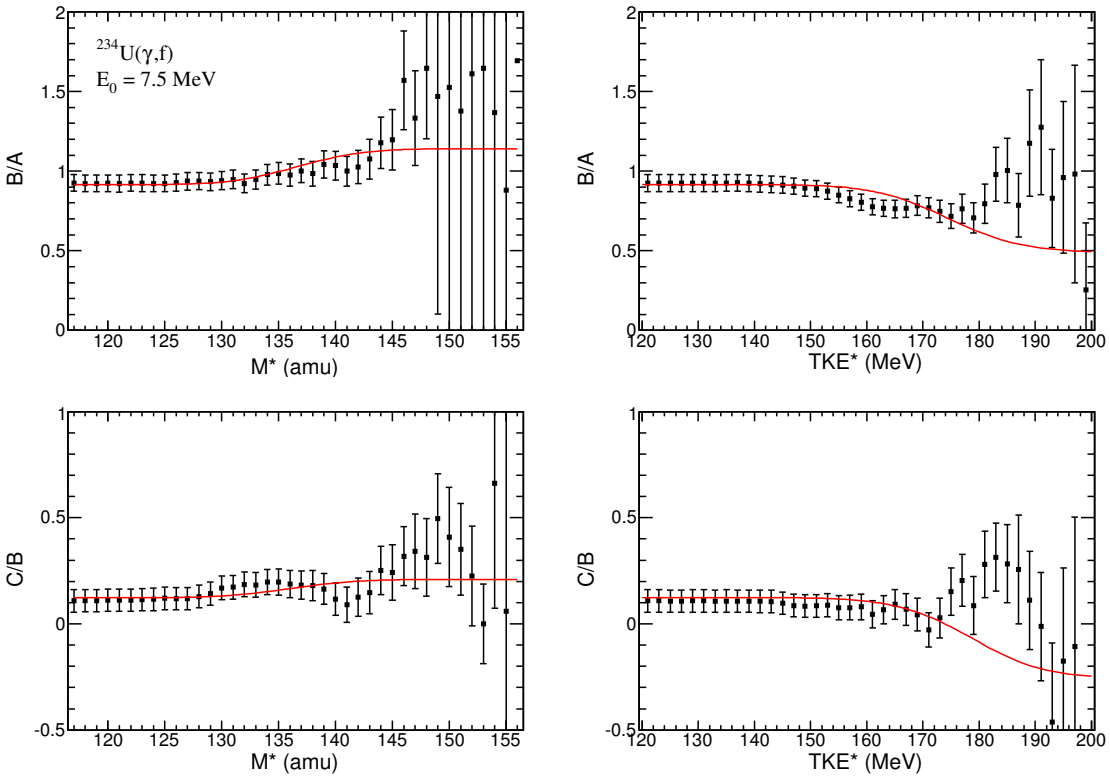

Fig. 6.16: *Dependence of fission-fragment angular distributions in* $^{234}U(\gamma, f)$ *at* $E_0 = 7.5$ *MeV on the parameters* M^* *(left) and* TKE^* *(right), as introduced in Sect. 5.3.1. The solid red lines show the expected behavior assuming specific angular distributions for the the two standard modes.*

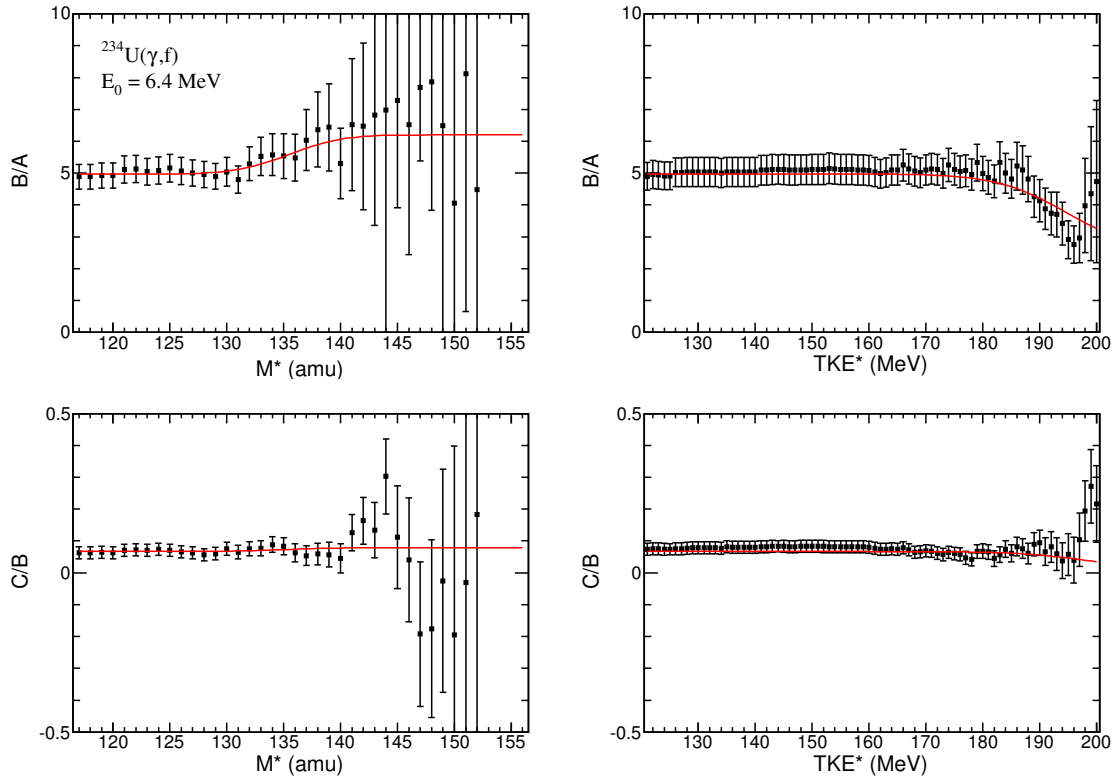

Fig. 6.17: *Dependence of fission-fragment angular distributions in* $^{234}U(\gamma, f)$ *at* $E_0 = 6.4$ *MeV on the parameters* M^* *(left) and* TKE^* *(right), as introduced in Sect. 5.3.1. The solid red lines show the expected behavior assuming specific angular distributions for the the two standard modes.*

value of the B/A ratio is expected. More excitation energy available on top of the barrier would lead to less predominant fission through the lower energy $(J^\pi, K) = (1^-, 0)$ channel. This was not observed in the experimental data. On the contrary, a higher value of the B/A ratio has been found for the S2 mode in all the measurements, which still remains to be understood.

Tab. 6.6: *Angular distribution parameters determined for the two standard fission modes in the reaction $^{232}Th(\gamma, f)$ and $^{234}U(\gamma, f)$.*

	E_0 (MeV)		A	B	C
^{232}Th	9.5	S1	0.28±0.01	0.32±0.01	-0.07±0.02
		S2	0.16±0.01	0.49±0.01	0.052±0.02
	8.0	S1	0.160±0.01	0.536±0.01	-0.04±0.02
		S2	0.03±0.01	0.66±0.01	0.06±0.02
^{234}U	9.0	S1	0.47±0.02	0.062±0.02	0.09±0.02
		S2	0.36±0.02	0.18±0.02	0.01±0.02
	7.5	S1	0.40±0.02	0.21±0.02	-0.07±0.02
		S2	0.26±0.02	0.30±0.02	0.07±0.02
	6.4	S2	0.20±0.03	0.47±0.03	-0.02±0.03
		S2	0.08±0.03	0.58±0.03	0.06±0.03

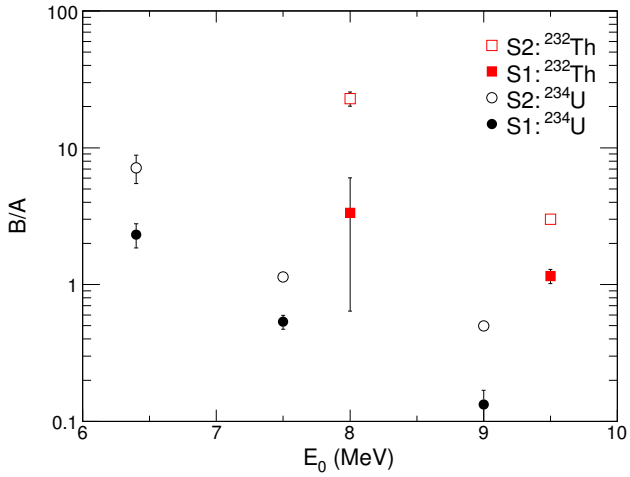

Fig. 6.18: *Ratios B/A of the angular distribution coefficients determined for the two standard fission modes in $^{234}U(\gamma, f)$ and in $^{232}Th(\gamma, f)$ as a function of the bremsstrahlung endpoint energy.*

Chapter 7

Summary and Conclusions

In this work fission-fragment characteristics in the photofission of ^{232}Th, ^{234}U and ^{238}U have been studied by means of the double-kinetic-energy technique. Bremsstrahlung was produced in a copper radiator from the electron beam of the injector linac to the S-DALINAC. A twin Frisch-grid ionization chamber has been used to simultaneously determine mass, TKE and emission angle of the fission fragments.

The motivation for the experiment on ^{238}U was to establish the experimental technique and analysis procedures. Excellent agreement with literature data of the main fission fragment characteristics was found for the reaction $^{238}\mathrm{U}(\gamma, f)$ in the excitation energy range of 5.9 – 6.9 MeV. In the development of the experimental technique special attention was paid to the determination of fission fragment angular distributions by means of electron drift-time measurements. The results show that the drift-time technique for the emission angle determination is comparable in accuracy with more established techniques, but with a much simplified experimental procedure. In conclusion, it was found that the ionization chamber is well suited for photofission studies.

Mass and TKE distributions of $^{234}\mathrm{U}(\gamma, f)$ in the excitation energy region of 5.8 – 7.2 MeV, close to the neutron separation threshold, has been determined for the first time. The mean heavy-fragment mass number is around 138.1, and the mean TKE is around 169.9 MeV. Results on the mass and TKE distributions of $^{232}\mathrm{Th}(\gamma, f)$ in the excitation energy region of 6.7 – 7.3 MeV show a mean heavy-fragment mass number around 140.6 and a mean TKE around 163.0 MeV.

A mass and TKE dependence of the angular distribution of fission fragments in the reaction $^{232}\mathrm{Th}(\gamma, f)$ has been found, similar to the mass dependence at higher excitation energies reported in Ref. [48] and for the first time in ^{234}U. The dependence takes the form of an increased anisotropy for far-asymmetric mass splits.

An analysis in terms of fission modes has been performed for all the fissioning systems investigated in this thesis. The results show a dominant S2 yield for the asymmetric mass yield in all the nuclei, with ∼77 % in ^{232}Th, ∼75 % in ^{234}U and ∼67 % in ^{238}U. The yield of the symmetric SL mode was small (below 1 %) for all nuclei. No strong dependence of the mode weights on the excitation energy was found. The angular distribution dependence on mass and TKE has also been analyzed in terms of fission modes, and could be described as a superposition of specific angular distributions for the two standard fission modes. This analysis results in a larger anisotropy for the S2 mode, as compared to the S1 mode, which suggests a higher outer barrier for this fission mode, in contrast to what is expected from the relative yield of the two standard modes in a static model of the fission process. Supporting evidence for the conjecture of separate outer fission barrier of the two standard modes may be found by extending the experiments performed in this thesis work to lower bremsstrahlung endpoint energies, in order to extract barrier parameters for the different fission modes from their respective angular distributions. A further probe is the investigation of the fragment characteristics from isomeric fission, which proceed via penetration of the outer barrier. Due to the small cross sections in both of these types of experiments they would greatly benefit from an increase in luminosity. The increase in thickness of the solid sample used in this work is undesirable due the deterioration of resolution. The effect of added target thickness has been demonstrated in the experiments on ^{234}U(γ, f) which were performed with two different targets with thicknesses of 190.0 μg/cm^2 and 46.6 μg/cm^2, respectively. The data obtained with the two different targets showed substantial discrepancies from each other. A folding procedure, taking the specific energy loss of the fission fragments in the added target layer into account, was able to explain these discrepancies. Hence, special attention must be paid to the quality of the target, when determining mass and TKE distributions by means of the double-kinetic-energy technique. Moderate increase in luminosity may be achieved by using an array of ionization chambers along the beam path. Together with a planned upgrade of the superconducting injector linac of the S-DALINAC to provide higher beam currents [94], an increase in luminosity of one order of magnitude may be achieved. Another possible way to reach very high luminosity without sacrificing resolution is the use of a gaseous active target. As a first step to such a device experimental investigations of counting gas properties of UF_6 has been undertaken, preliminary results is discussed in the last chapter of this thesis.

Chapter 8

Outlook

8.1 A Gaseous Uranium Hexaflouride Active Target

As mentioned in the introduction the new polarized injector SPIN [28] installed at the S-DALINAC [13] give access to experimental investigation of parity-non-conservation (PNC) effects in photofission. A future PNC investigation in photofission requires excellent statistical accuracy. Provided the same enhancement effects as in neutron-induced fission, the order of magnitude of the PNC asymmetry is expected to be about 10^{-4} [95]. An estimate of the time needed to deliver statistically relevant results for an experiment with the setup used in this work leads to more than a year of beam-time for endpoint energies not exceeding 7.0 MeV. Hence, a significant increase in luminosity is mandatory for a PNC experiment to become feasible. As discussed in Sects. 4.2.1 and 5.2, an increase in the thickness of the solid targets would severely diminish the angular and mass resolutions. Another approach to achieve the required luminosity is the use of an active target. A candidate for such an active target is UF_6, since it is gaseous at temperatures exceeding 64°C at ambient pressure [96].

The active target approach may also be interesting from other viewpoints. One limitation of the experiments described in this thesis is the use of bremsstrahlung, which cannot deliver excitation energy resolved results. A way to overcome this limitation is the use of tagged photons. The maximum rate of tagged photons at the NEPTUN photon tagger [97] at the S-DALINAC is, however, about two orders of magnitude lower than the photon flux achieved at the bremsstrahlung setup and therefore requires a substantial increase in target mass. Another point of interest is the investigation of mass and TKE distributions from (deep) sub-barrier fission, where low cross sections require high luminosities.

8.1.1 Setup for Investigation of UF_6 Counting-Gas Properties

For the purpose of investigating the counting gas properties of UF_6, a test setup has been constructed, consisting of a single-sided Frisch-grid ionization chamber, which is filled with argon and different admixtures of UF_6. In order to keep UF_6 gaseous, the ionization chamber is heated to a temperature of 70°C. Since UF_6 is highly reactive and creates hydrofluoric acid when coming into contact with water vapor [96], several cautionary measures are needed when handling the gas. All parts of the setup that may come into contact with UF_6 are therefore required to be made of special materials. The setup is manufactured entirely out of stainless steel and copper components, except for parts that need to be insulating, where polytetrafluoroethylene (PTFE) was used. To ensure that no UF_6 can escape, the system was vacuum He-leak tested down to 10^{-9} mbar l/s. A more complete description of the gas system will be given elsewhere [98].

A calibration source, consisting of ^{239}Pu, ^{241}Am and ^{244}Cm, is mounted in the plane of the cathode of the ionization chamber. The alpha-particle activity of the calibration source is used to ensure the functionality of the ionization chamber prior to the introduction of UF_6 to the counting gas.

8.1.2 Experimental Procedure and Preliminary Results

The pulse heights from the anode and the cathode from each event are digitized and written in a list-mode file for offline analysis. The two-dimensional presentation of the registered anode versus cathode pulse heights, depicted in Fig. 8.1, serves as a tool for investigating the properties of the counting gas. The equations describing the dependence of the pulse height on the deposited energy and the position of the center of gravity of the charge distribution created by the alpha particles have already been presented in Sect. 3.2. On the left-hand side of Fig. 8.1 the raw data obtained with the ionization chamber heated to 70°C, prior to the introduction of any UF_6, is displayed. Three well separated lines can be seen in the plot, corresponding to the three main lines from the calibration source. The small inclination of these lines as a function of the cathode pulse height is due to the inefficiency of the grid. It should be noted that, due to the dimensions of the chamber, alpha particles originating from the calibration source and emitted at large angles θ relative to the cathode plane normal cannot be stopped within the sensitive volume. This causes a smearing effect of the energy resolution towards small values of the cathode pulse height. An energy calibration taking these two effects into account resulted in an energy resolution for the chosen setup of (57.4 ± 0.5) keV FWHM. The effect on the experimental raw data of adding an amount of UF_6 equivalent to 40 μg U/cm^3 is displayed on the right hand side of Fig. 8.1. The interpretation of the spectrum is complicated by the fact that the alpha particles from the UF_6 does not have a fixed point of origin. The inclination of the three

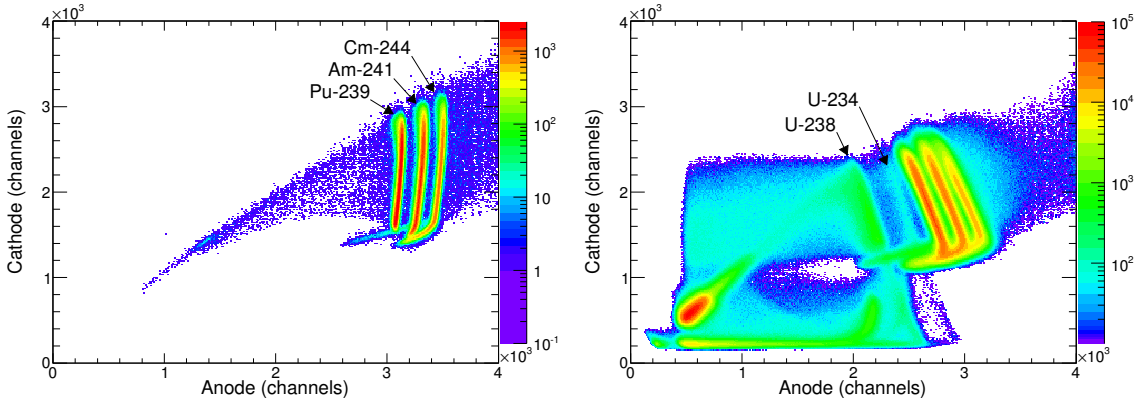

Fig. 8.1: *Raw experimental data from the UF_6 test setup. Left: Chamber filled with pure argon at a temperature of 70 °C. Right: Chamber filled with argon and an admixture of UF_6 gas equivalent to 40 μg U/cm^3. The color scales indicate the number of counts per bin.*

alpha-particle lines from the source is reversed as compared to the data obtained with pure argon. This fact indicates that electrons are captured by impurities in the counting gas, since there exists a linear relation between the time electrons spend in the counting gas and the cosine of the emission angle θ. The impurities could be traced back to a small amount of air that was present in the UF_6 container, or the gas-line connecting the container with the chamber, and introduced into the counting gas simultaneous with the first filling with UF_6. Further addition of UF_6 from the sample container did not affect the inclination of the alpha lines. In addition to the three alpha-particle lines from the calibration source, two fainter lines may be recognized at lower anode pulse heights. These two lines correspond to the alpha-particle energies of ^{238}U and ^{234}U, the two main alpha-particle emitters in the UF_6 gas. It is noted that these two lines are present also at cathode pulse heights lower than those allowed for alpha-particles originating from the cathode plane. This can only be achieved by alpha-particles that do not originate from the cathode. Hence, this verifies that gaseous UF_6 exists within the sensitive volume. One may also notice a component of the spectrum at low cathode pulse heights, stretching from very low anode channel numbers to about channel number 2200. These events originate from alpha particles depositing the major part of their energy between anode and grid, and consequently induce little to no charge on the cathode. Events above the diagonal, with a larger cathode than anode pulse height, represent alpha-decays that take place close to the chamber walls, so that electrons are not collected by the anode. By choosing a region of interest that excludes events, where alpha-particles from the source pass the grid, and projecting the data onto an axis perpendicular to the inclined alpha-particle lines, an energy spectrum is obtained. This energy spectrum has been calibrated using the three alpha-particle lines from the

calibration source and is displayed in Fig. 8.2. Arrows indicate the energies of the alpha particles emitted from the various substances present in the chamber. The energy resolution of this gas mixture was determined to be (81.2 ± 0.8) keV FWHM.

The drift velocity of ionization electrons in the counting gas mixture was also determined. The procedure for determining the drift velocity is based on measuring the rise time of the cathode signal and was adopted from Ref. [61]. In Fig. 8.3 the obtained drift velocities for pure argon as well as argon with an admixture of UF_6 equivalent to 20 μg U/cm^3 and 40 μg U/cm^3 are displayed as a function of reduced field strength. The drift velocities show an initial increase that reaches a maximum for high values of the field strength; further increase of the field strength slightly reduces the drift velocity eventually reaching a plateau. The introduction of a small amount of UF_6 clearly increases the drift velocity. This behavior is expected when introducing a complex molecule into the gas mixture, since it reduces the number of elastic collisions an electron experiences when drifting in the electric field. Furthermore, the drift velocity plateau is then only reached at higher field strengths. Since the ionization chamber needs to be operated in the drift velocity plateau region, the use of a large concentration of UF_6 in the counting gas requires an increased field strength. At reduced field strengths above 300 V/(cm·atm) with the highest amount of UF_6 content, the chamber experienced electrical breakdown delaying further experiments.

In conclusion, the experiments show promising results for an active target based on the argon–UF_6 gas mixture. Further experiments reaching higher concentration of UF_6 are foreseen after improvement of the current experimental setup. These results will be presented and discussed in Ref. [98].

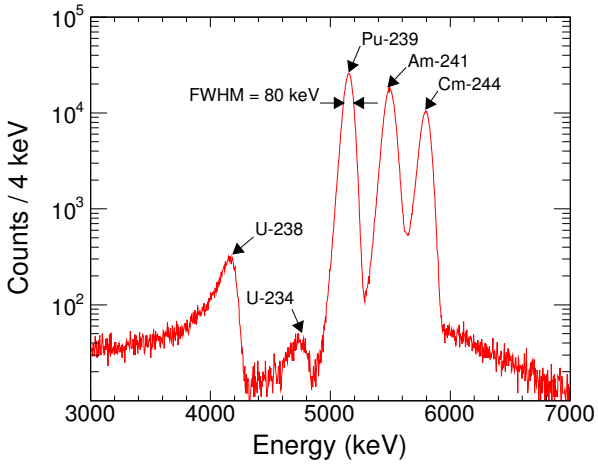

Fig. 8.2: *Energy spectrum obtained for a counting gas mixture of argon and an amount of UF_6 equivalent to 40 $\mu gU/cm^3$.*

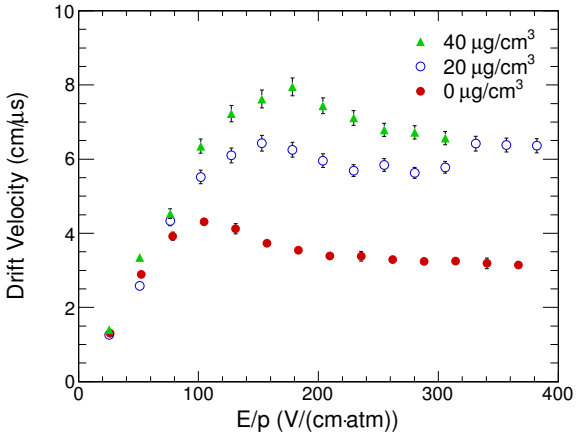

Fig. 8.3: *Electron drift velocity as a function of reduced field strength in pure argon as well as argon with an admixture of UF_6 equivalent to 20 μg U/cm^3 and 40 μg U/cm^3.*

8.2 Investigations of Shape Isomers

As mentioned in Sect. 2.1 shape isomers are explained as meta-stable states in the second minimum of the fission barrier that decay through either fission, by tunneling the outer barrier, or gamma-decay back to the ground state. The properties of shape isomers, such as decay mode and half life, directly probes the structure of the fission barrier. Although general features of fission barriers and shape isomers are fairly well understood, more experimental work is needed to address open questions, such as properties of the suggested third hyper-deformed minimum in the fission barrier [99, 100].

The first measurement series on ^{234}U(γ, f), cf. Sect. 3 was in part performed with a 20 MHz pulsed electron beam, in order to test the possibility to identify shape isomers with the present setup. To measure the time distribution of fission events a stop signal coinciding with the start of the beam pulse and with a properly adjusted delay was fed into the TDC. The start signal for the time measurement was taken from the cathode timing signal, the timing resolution was about 1 ns. In Fig. 8.4 the time distribution of fission events for two different electron beam energies are shown. The contribution of a possible delayed component of the yield can be expected on the leading edge of the prompt peak. The identification of delayed fission events is complicated by the time-structure of the beam pulse. At the 9.0 MeV beam energy the contribution of a possible fission isomer is negligible due to the low isomeric-to-prompt yield ratio. Hence, the time distribution of fission events at this beam energy corresponds to the time-structure of the beam pulse. In case there exists a fission isomer with a half-life larger than the width of the beam pulse ($\sim$ 10 ns) one may expect an increase in the fission yield on the leading edge of the prompt peak when lowering the electron beam energy. Obviously, no such change is observed in the data. In total 10980 prompt fission events were identified at the bremsstrahlung endpoint energy of 6.8 MeV. Based on the number of prompt fission events it is concluded that no fission isomer in ^{234}U with a half life larger than 10 ns and an isomeric-to-prompt yield ratio larger than 10^{-4} at 6.8 MeV bremsstrahlung could be found. The new polarized photo-injector [28, 101, 102] recently installed at the S-DALINAC is able to deliver intense pulsed electron beams $\sim$5 ps pulse widths. This will facilitate future experiments to identify fission isomers.

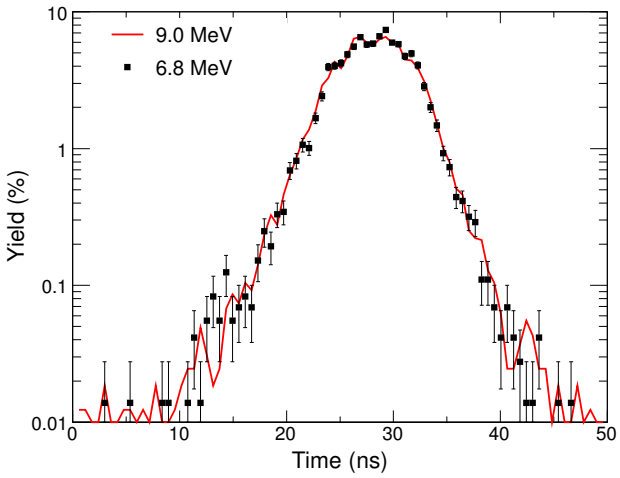

Fig. 8.4: *Time distribution of fission events from the reaction* $^{234}U(\gamma, f)$ *with 8.5 MeV and 6.8 MeV bremsstrahlung, obtained with a 20 MHz pulsed electron beam.*

Appendix A

Transformation of Angular Distributions

The transformation of an angular distribution relative to the chamber axis into the angular distribution relative to the beam, when the former is oriented at a 45° angle relative to the latter, can be obtained in the following way. Let θ represent the angle between the fission axis and the beam. Furthermore let θ_c and ϕ_c represent the polar and azimuthal angle of the fission axis in the chamber coordinates. A rotation of 45° of the chamber relative to the beam then implies

$$\cos\theta = \frac{1}{\sqrt{2}}\cos\theta_c + \frac{1}{\sqrt{2}}\sin\theta_c \sin\phi_c. \tag{A.1}$$

The angular distribution observed relative to the chamber axis may be written

$$W(\theta_c) = \frac{1}{2\pi}\int_0^{2\pi} W(\theta) d\phi_c, \tag{A.2}$$

where the angular distribution relative to the beam $W(\theta)$ is represented by Eq. (5.4), which can be rewritten in terms of $\cos\theta$,

$$W(\theta) = A + B\sin^2\theta + C\sin^2 2\theta = \alpha + \beta\cos^2\theta + \gamma\cos^4\theta, \tag{A.3}$$

with

$$\begin{cases} \alpha &= A + B \\ \beta &= 4C - B \\ \gamma &= -4C \end{cases}.$$

Combining Eqs. (A.1), (A.2) and (A.3) and solving the integrals then leads to

$$\begin{aligned} W(\theta_c) &= \frac{\alpha}{2\pi}\int_0^{2\pi} d\phi_c + \frac{\beta}{2\pi}\int_0^{2\pi} \cos^2\theta d\phi_c + \frac{\gamma}{2\pi}\int_0^{2\pi} \cos^4\theta d\phi_c \\ &= \alpha' + \beta'\cos^2\theta_c + \gamma'\cos^4\theta_c, \end{aligned} \tag{A.4}$$

with

$$\begin{cases} \alpha' = & A + \frac{3}{4}B + \frac{5}{8}C \\ \beta' = & -\frac{1}{4}B - \frac{5}{4}C \\ \gamma' = & \frac{13}{8}C \end{cases} \iff \begin{cases} A = & \alpha' + 3\beta' + \frac{25}{13}\gamma' \\ B = & -4(\beta' - \frac{10}{13}\gamma') \\ C = & \frac{8}{13}\gamma' \end{cases} . \tag{A.5}$$

Thus, by fitting the experimental data with Eq. (A.4) and using Eq. (A.5), the physically relevant angular distribution could still be obtained with the ionization chamber in the 45° position. However, due to the limited range in which the angular distribution can be determined and the strong correlation between the parameters A, B and C, the accuracy of the result is affected.

Bibliography

[1] O. Hahn, F. Strassmann, Naturwiss. 27 (1939) 11.

[2] L. Meitner, O. Frisch, Nature 143 (1939) 239.

[3] O. Frisch, Nature 143 (1939) 276.

[4] A. Nuttin, D. Heuer, A. Billebaud, R. Brissot, C. L. Brun, E. Liatard, J.-M. Loiseaux, L. Mathieu, O. Meplan, E. Merle-Lucotte, H. Nifenecker, F. Perdu, S. David, Prog. Nucl. Energy 46 (2005) 77.

[5] J. J. Cowan, F.-K. Thielemann, J. W. Truran, Phys. Rep. 208 (1991) 267.

[6] A. Turkevich, J. B. Niday, Phys. Rev. 84 (1951) 52.

[7] U. Brosa, S. Grossman, A. Müller, Phys. Rep. 197 (1990) 167.

[8] P. Siegler, F.-J. Hambsch, S. Oberstedt, J. Theobald, Nucl. Phys. A 594 (1995) 45.

[9] S. Oberstedt, F.-J. Hambsch, F. Vivés, Nucl. Phys. A 644 (1998) 289.

[10] F.-J. Hambsch, F. Vivés, P. Siegler, S. Oberstedt, Nucl. Phys. A 679 (2000) 32.

[11] G. Vladuca, A. Tudora, F.-J. Hambsch, S. Oberstedt, Nucl. Phys. A 707 (2002) 32.

[12] F.-J. Hambsch, G. Vladuca, A. Tudora, S. Oberstedt, I. Ruskov, Ann. Nucl. Energy 32 (2005) 1297.

[13] A. Richter, in: Proc. Fifth European Particle Accelerator Conference, Sitges/Spain 1996, Institute of Physics Publishing, Bristol, Philadelphia, 1996, p. 110.

[14] A. Göök, M. Chernykh, C. Eckardt, J. Enders, P. von Neumann-Cosel, A. Oberstedt, S. Oberstedt, A. Richter, Nucl. Phys. A 851 (2011) 1.

[15] A. Göök, M. Chernykh, J. Enders, A. Oberstedt, S. Oberstedt, Nucl. Instr. and Meth. A 621 (2010) 401.

[16] S. Pommé, Dissertation, Universiteit Gent (1992).

[17] S. Pommé, E. Jacobs, M. Piessens, D. De Frenne, K. Persyn, K. Govaert, M.-L. Yoneama, Nucl. Phys. A 572 (1994) 237.

[18] M. M. Abu-Khader, Progress in Nuclear Energy 51 (2009) 225.
URL http://www.sciencedirect.com/science/article/pii/S0149197008000851

[19] G. V. Danilyan, B. D. Vodennikov, V. P. Dronyaev, V. V. Novitskii, V. S. Pavlov, S. P. Borovlev, JETP Lett. 26 (1977) 186.

[20] G. V. Danilyan, B. D. Vodennikov, V. P. Dronyaev, V. V. Novitskii, V. S. Pavlov, S. P. Borovlev, Sov. J. Nucl. Phys. 27 (1978) 21.

[21] N. V. Borovikova, V. A. Vesna, A. I. Egorov, V. A. Knyaz'kov, A. Kolomenskii, V. M. Lobashev, A. N. Pirozhkov, L. A. Popeko, L. M. Smotritskii, N. A. Titov, A. I. Shablii, JETP Lett. 30 (1979) 495.

[22] U. Graf, F. Gönnenwein, P. Geltenbort, K. Schreckenbach, Z. Phys. A 351 (1995) 281.

[23] A. Kötzle, P. Jesinger, F. Gönnenwein, G. Petrov, V. Petrova, A. Gagarski, G. Danilyan, O. Zimmer, V. Nesvizhevsky, Nucl. Instr. and Meth. A 440 (2000) 750.

[24] G. E. Mitchell, A. Richter, H. A. Weidenmüller, Rev. Mod Phys. 82 (2010) 2845.

[25] G. E. Mitchell, J. D. Bowman, S. I. Penttilä, E. I. Sharapov, Phys. Rep. 345 (2001) 157.

[26] G. E. Mitchell, J. D. Bowman, H. A. Weidenmüller, Rev. Mod. Phys. 71 (1999) 445.

[27] H. A. Weidenmüller, Nucl. Phys. A 574 (1994) 75c.

[28] Y. Poltoratska, C. Eckardt, W. Ackermann, K. Aulenbacher, T. Bahlo, R. Barday, M. Brunken, C. Burandt, R. Eichhorn, J. Enders, M. Espig, S. Franke, C. Ingenhaag, J. Lindemann, W. F. O. Müller, M. Platz, M. Roth, F. Schneider, M. Wagner, A. Weber, T. Weiland, B. Zwicker, J. Phys. Conf. Series 298 (2011) 012002.

[29] V. V. Flambaum, G. F. Gribakin, Prog. Part. Nucl. Phys. 35 (1995) 423.

[30] R. Haxby, W. Shoupp, W. Stephens, W. Wells, Phys. Rev. 59 (1941) 57.

[31] G. C. Baldwin, G. Klaiber, Phys. Rev. 71 (1947) 3.

[32] G. C. Baldwin, G. Klaiber, Phys. Rev. 73 (1948) 1156.

[33] N. Bohr, J. Wheeler, Phys. Rev. 56 (1939) 426.

[34] H. Weigmann, in: The nuclear fission process, Ed. C. Wagemans, CRC Press, Boca Raton, Florida, 1991, Ch. 2, p. 7.

[35] V. Strutinsky, Nucl. Phys. A95 (1967) 420.

[36] S. M. Polikanov, V. A. Druin, V. A. Karnauchov, V. L. Mikheev, A. A. Pleve, N. K. Skobelev, V. G. Subotin, G. M. Ter-Akapian, V. A. Fomichev, Zh. Eksp. Teor. Fiz. 42 (1962) 1016.

[37] D. Paya, J. Blons, H. Derrien, A. Michaudon, in: Physics and Chemistry of Fission, IAEA, Vienna, 1969, p. 307.

[38] E. Migneco, J. Theobald, Nucl. Phys. A 112 (1968) 603.

[39] A. Bohr, in Proc. Int. Conf. Peaceful uses of Atomic Energy I (1956) 151.

[40] R. VandenBosch, J. R. Huizenga, Nuclear Fission, Academic Press, New York, 1974.

[41] E. Jacobs, U. Kneissl, in: The nuclear fission process, Ed. C. Wagemans, CRC Press, Boca Raton, Florida, 1991, Ch. 5, p. 103.

[42] J. Moreau, K. Heyde, in: The nuclear fission process, Ed. C. Wagemans, CRC Press, Boca Raton, Florida, 1991, Ch. 7, p. 227.

[43] B. D. Wilkins, E. P. Steinberg, R. R. Chasman, Phys. Rev. C 14 (1976) 1832.

[44] J. Moreau, K. Heyde, M. Waroquier, Phys. Rev. C 28 (1983) 1640.

[45] J. R. Adam, N. R. Lindblad, C. D. Hendricks, Jour. Appl. Phys. 39 (11) (1968) 5173.

[46] G. Vladuca, A. Tudora, F.-J. Hambsch, S. Oberstedt, I. Ruskov, Nucl. Phys. A (2003) 274.

[47] W. Wilke, R. Heil, U. Kneissl, U. Seemann, F. Steiper, H. Ströher, T. Weber, Phys. Lett. B 207 (1988) 385.

[48] F. Steiper, T. Frommhold, W. Henkel, A. Jung, U. Kneissl, R. Stock, Nucl. Phys. A 563 (1993) 282.

[49] H.-H. Knitter, in: The nuclear fission process, Ed. C. Wagemans, CRC Press, Boca Raton, Florida, 1991, Ch. 10, p. 491.

[50] P. Mohr, J. Enders, T. Hartmann, H. Kaiser, D. Schiesser, S. Schmitt, S. Volz, F. Wissel, A. Zilges, Nucl. Instr. and Meth. A 423 (1999) 480.

[51] K. Sonnabend, D. Savran, J. Beller, M. Büssing, A. Constantinescu, M. Elvers, J. Endres, M. Fritzsche, J. Glorius, J. Hasper, J. Isaak, B. Löher, S. Müller, N. Pietralla, C. Romig, A. Sauerwein, L. Schnorrenberger, C. Wälzlein, A. Zilges, M. Zweidinger, Nucl. Instr. and Meth. A 640 (2011) 6.

[52] M. Fritzsche, Diplomarbeit, Institut für Kernphysik, Technische Universität Darmstadt, unpublished (2007).

[53] B. B. Rossi, H. H. Staub, Ionization Chambers and Counters, 1st Edition, Vol. Experimental techniques of National Nuclear Energy Series, McGraw-Hill, New York, 1949.

[54] O. Bunemann, T. Cranshaw, J. Harvey, Can. Jour. Res. A 27 (1949) 191–206.

[55] V. A. Khriachkov, A. A. Goverdovski, V. V. Ketlerov, V. F. Mitrofanov, N. N. Semenova, Nucl. Instr. and Meth. A 394 (1997) 261.

[56] W. Shockley, Jour. Appl. Phys. 9 (1938) 635–636.

[57] S. Ramo, Proceedings of the IRE 27 (1939) 584–585.

[58] P. M. Morse, H. Feshbach, Methods of Theoretical Physics, McGraw-Hill, New York, 1953.

[59] M. Lyly, J. Ruokolainen, P. Råback, Elmer 6.0, Computer Code (2008).
URL `http://www.csc.fi/english/pages/elmer`

[60] C. Budtz-Jørgensen, H.-H. Knitter, C. Straede, F.-J. Hambsch, R. Vogt, Nucl. Instr. and Meth. A 258 (1987) 209.

[61] A. Göök, Master's thesis, Örebro universitet (2008).

[62] A. Göök, F.-J. Hambsch, A. Oberstedt, S. Oberstedt, Nucl. Instr. and Meth. A 664 (2012) 289.

[63] J. Ziegler, M. Ziegler, J. Biersack, Srim 2008.04, Computer Code (2008).
URL `http://www.srim.org/`

[64] R. Barth, Y. Du, H. Essel, R. Fritzsche, H. Göringer, J. Hoffmann, F. Humbert, N. Kurz, R. Mayer, W. Ott, D. Schall, Gsi multi-branch system user manual (2000).
URL `http://www-win.gsi.de/daq/Docs/gm_mbs_i_2.pdf`

[65] J. Adamczewski-Musch, M. Al-Turany, D. Bertini, H. G. Essel, S. Linev, The go4 analysis framework v3, Computer Code (2008).
URL `http://www-win.gsi.de/go4/`

[66] S. Agostinelli, J. Allison, K. Amako, J. Apostolakis, H. Araujo, P. Arce, M. Asai, D. Axen, S. Banerjee, G. Barrand, F. Behner, L. Bellagamba, J. Boudreau, L. Broglia, A. Brunengo, H. Burkhardt, S. Chauvie, J. Chuma, R. Chytracek, G. Cooperman, G. Cosmo, P. Degtyarenko, A. Dell'Acqua, G. Depaola, D. Dietrich, R. Enami, A. Feliciello, C. Ferguson, H. Fesefeldt, G. Folger, F. Foppiano, A. Forti, S. Garelli, S. Giani, R. Giannitrapani, D. Gibin, J. G. Cadenas, I. González, G. G. Abril, G. Greeniaus, W. Greiner, V. Grichine, A. Grossheim, S. Guatelli, P. Gumplinger, R. Hamatsu,

K. Hashimoto, H. Hasui, A. Heikkinen, A. Howard, V. Ivanchenko, A. Johnson, F. Jones, J. Kallenbach, N. Kanaya, M. Kawabata, Y. Kawabata, M. Kawaguti, S. Kelner, P. Kent, A. Kimura, T. Kodama, R. Kokoulin, M. Kossov, H. Kurashige, E. Lamanna, T. Lampén, V. Lara, V. Lefebure, F. Lei, M. Liendl, W. Lockman, F. Longo, S. Magni, M. Maire, E. Medernach, K. Minamimoto, P. M. de Freitas, Y. Morita, K. Murakami, M. Nagamatu, R. Nartallo, P. Nieminen, T. Nishimura, K. Ohtsubo, M. Okamura, S. O'Neale, Y. Oohata, K. Paech, J. Perl, A. Pfeiffer, M. Pia, F. Ranjard, A. Rybin, S. Sadilov, E. D. Salvo, G. Santin, T. Sasaki, N. Savvas, Y. Sawada, S. Scherer, S. Sei, V. Sirotenko, D. Smith, N. Starkov, H. Stoecker, J. Sulkimo, M. Takahata, S. Tanaka, E. Tcherniaev, E. S. Tehrani, M. Tropeano, P. Truscott, H. Uno, L. Urban, P. Urban, M. Verderi, A. Walkden, W. Wander, H. Weber, J. Wellisch, T. Wenaus, D. Williams, D. Wright, T. Yamada, H. Yoshida, D. Zschiesche, Nucl. Instr. and Meth. A 506 (3) (2003) 250.

[67] M. Chadwick, P. Oblozinsky, M. Herman, N. Greene, R. McKnight, D. Smith, P. Young, R. MacFarlane, G. Hale, S. Frankle, A. Kahler, T. Kawano, R. Little, D. Madland, P. Moller, R. Mosteller, P. Page, P. Talou, H. Trellue, M. White, W. Wilson, R. Arcilla, C. Dunford, S. Mughabghab, B. Pritychenko, D. Rochman, A. Sonzogni, C. Lubitz, T. Trumbull, J. Weinman, D. Brown, D. Cullen, D. Heinrichs, D. McNabb, H. Derrien, M. Dunn, N. Larson, L. Leal, A. Carlson, R. Block, J. Briggs, E. Cheng, H. Huria, M. Zerkle, K. Kozier, A. Courcelle, V. Pronyaev, S. van der Marck, Nucl. Data Sheets 107 (2006) 2931.

[68] A. S. Soldatov, Ser. Yad. Konstanty 1 (1997) 859.

[69] E. Birgersson, Dissertation, Örebro universitet (2007).

[70] P. Siegler, Dissertation D17, Technische Hochschule Darmstadt (1994).

[71] F. Vivès, Dissertation, Université de Bordeaux (1998).

[72] G. Barreau, A. Sicre, F. Caitucoli, M. Asghar, T. Doan, B. Leroux, G. Martinez, T. Benfoughal, Nucl. Phys. A432 (1985) 411.

[73] H. Nifenecker, C. Signarbieux, R. Babinet, J. Poitou, in: Proc. 3rd Symp. on Physics and Chemistry of Fission, Vol. 2, IAEA, Vienna, 1974, p. 51.

[74] V. Apalin, Y. N. Gritsyuk, I. Kutikov, V. Lebedev, L. Mikaelian, Nucl. Phys. 71 (1965) 533.

[75] M. Piessens, Dissertation, Rijksuniversiteit Gent (1989).

[76] T. D. M. Weijers-Dall, H. Timmers, R. G. Elliman, Nucl. Instr. and Meth. A 550 (2005) 139.

[77] J. K. Knipp, R. C. Ling, Phys. Rev. 82 (1951) 30.

[78] J. Lindhard, V. Nielsen, M. Scharff, P. V. Thomsen, Mat.-Fys. Medd. 33 (1963) 10.

[79] J. Lindhard, M. Scharff, H. E. Schiott, Mat.-Fys. Medd. 33 (1963) 14.

[80] F. Tovesson, F.-J. Hambsch, S. Oberstedt, H. Bax, Nucl. Scien. Tech. Suppl. 2 (2002) 673.

[81] J. P. Unik, J. E. Gindler, L. E. Glendenin, K. F. Flynn, A. Gorski, R. K. Sjöblom, in: Proc. Symp. Physics and Chemistry of Fission, Vol. 2, IAEA, Vienna, 1974.

[82] V. Viola, K. Kwiatkowski, M. Walker, Phys. Rev. C31 (1985) 1550.

[83] E. Birgersson, A. Oberstedt, S. Oberstedt, F.-J. Hambsch, Nucl. Phys. A 817 (2009) 1–34.

[84] J. F. Ziegler, Appl. Phys. Lett. 31 (8) (1977) 544.

[85] D. Lang, R. Walsh, Nucl. Instr. and Meth. 200 (1982) 389.

[86] H. G. Rajprakash, G. Sanjeev, K. B. Vijaykumar, K. Siddappa, B. K.Ñayak, A. Saxena, Indian J. Phys. 83 (2009) 1135.

[87] R. Vandenbosch, Phys. Lett. B 45 (3) (1973) 207.

[88] A. Manfredini, L. Fiore, C. Ramorino, H. G. de Carvalho, W. Wölfi, Nucl. Phys. A 123 (1969) 664.

[89] E. J. Dowdy, T. L. Krysinski, Nucl. Phys. A 175 (1971) 501.

[90] F. James, Minuit Reference Manual, CERN Program Library Long Writeup D506, CERN Computing and Networks Division (1998).

[91] F. James, M. Winkler, Minuit2, Computer Code.
URL `http://www.cern.ch/minuit`

[92] F.-J. Hambsch, H. H. Knitter, C. Budtz-Jørgensen, J. P. Theobald, Nuclear Physics A 491 (1989) 56.

[93] C. Wagemans, P. Schillebeeckx, A. Deruytter, Nucl. Phys. A 502 (1989) 287c.

[94] R. Eichhorn, R. Barday, U. Bonnes, M. Brunken, C. Eckardt, J. Conrad, J. Enders, H. D. Graef, C. Heßler, T. Kuerzeder, C. Liebig, M. Platz, Y. Poltoratska, M. Roth, S. T. Sievers, T. Weilbach, W. Ackermann, W. F. O. Mueller, B. Steiner, T. Weiland, K. Aulenbacher, J. D. Fuerst, in: Proceedings of the 2008 Linear Accelerator Conference (LINAC 2008), Victoria, B.C. Canada, 2008, p. 398.

[95] T. Wettig, H. A. Weidenmüller, Private Communication (1996).

[96] W. Bacher, Gmelin-Handbuch der anorganischen Chemie, Uran, Verbindungen mit Fluor, 8th Edition, Vol. Erg.-Bd. C., Verl. Chemie, Weinheim, 1980, p. 71.

[97] D. Savran, K. Lindenberg, J. Glorius, B. Löher, S. Müller, N. Pietralla, L. Schnorrenberger, V. Simon, K. Sonnabend, C. Wälzlein, M. Elvers, J. Endres, J. Hasper, A. Zilges, Nucl. Instr. and Meth. A 613 (2010) 232.

[98] C. Eckardt, Dissertation, Technische Universität Darmstadt, in Preparation.

[99] J. Blons, Nucl. Phys. A 502 (1989) 121.

[100] P. Thirolf, D. Habs, Prog. Part. Nucl. Phys. 49 (2002) 325.

[101] Y. Fritzsche, Dissertation D17, Technische Universität Darmstadt (2011). URL `http://tuprints.ulb.tu-darmstadt.de/2770`

[102] M. Wagner, Dissertation, Technische Universität Darmstadt, in Preparation.

Acknowledgement

I wish to thank my supervisor Professor Dr. Joachim Enders whose guidance and support has made this thesis work possible. I would like to sincerely thank Professor Dr. Andreas Oberstedt from Örebro university for guidance and countless fruitful discussions. My gratitude also goes out to Dr. Stephan Oberstedt, from whom I have also learned a great deal in many discussions. Professor Dr. Dr. h.c. mult. Achim Richter who initiated the photofission experimental campaign is also gratefully acknowledged.

Thanks to the neutron physics division at the Institute for Reference Materials and Measurements and in particular Dr. Franz-Josef Hambsch for lending us the targets that made the experiments possible. The experiment would of course not have been possible without the electron beams, thanks to the S-DALINAC operating team for providing them. Thank you also to the Enders work-group and everyone else who helped out with the experiment shifts.

On a personal note I want to thank my family and friends for their support and encouragement throughout the years.

The financial support from the DFG through SFB 634 is gratefully acknowledged.

Curriculum Vitae

Not available in online version.

Erklärung zur Dissertation

Hiermit versichere ich, die vorliegende Dissertation ohne Hilfe Dritter nur mit den angegebenen Quellen und Hilfsmitteln angefertigt zu haben. Alle Stellen, die aus Quellen entnommen wurden, sind als solche kenntlich gemacht. Diese Arbeit hat in gleicher oder ähnlicher Form noch keiner Prüfungsbehörde vorgelegen.

Darmstadt, den 13. November 2012

(Alf Göök)